

Dynamic Control of Metamaterials at Terahertz Frequencies

Author: David Shrekenhamer

Persistent link: <http://hdl.handle.net/2345/3152>

This work is posted on [eScholarship@BC](#),
Boston College University Libraries.

Boston College Electronic Thesis or Dissertation, 2013

Copyright is held by the author, with all rights reserved, unless otherwise noted.

Boston College

The Graduate School of Arts and Sciences

Department of Physics

**DYNAMIC CONTROL OF METAMATERIALS AT
TERAHERTZ FREQUENCIES**

a dissertation

by

DAVID SHREKENHAMER

submitted in partial fulfillment of the requirements

for the degree of

Doctor of Philosophy

May 2013

**DYNAMIC CONTROL OF METAMATERIALS AT TERAHERTZ
FREQUENCIES**

DAVID SHREKENHAMER

Boston College Graduate School of Arts and Sciences, 2013

Major Professor: Willie J. Padilla, Associate Professor of Physics

ABSTRACT

Progress in the field of metamaterials has started coming to a point where the field may finally begin to emerge as a viable solution to many electromagnetic challenges facing the community. No where is that more true than at terahertz frequencies where there lies an immense opportunity for growth. The development of mature technologies within this region of the electromagnetic spectrum would provide a valuable resource to become available for a multitude of applications. In order to achieve this, the necessary first steps of identifying viable materials and paths to integrate these with metamaterials will need to be completed.

In this dissertation, we examine several different paths to achieve dynamic metamaterial electromagnetic response at terahertz frequencies, and demonstrate several paths to package these devices into imaging systems. In Chapter 1, we introduce the basic theory and design principles of metamaterials. We also describe the experimental techniques involved in the study of terahertz metamaterials. Chapter 2 presents a computational and experimental study investigating the integration of high electron mobility transistors with metamaterials allowing for high speed modulation of incident

terahertz radiation. In Chapters 3 and 4, we investigate several different paths to create tunable terahertz metamaterial absorbers. Chapter 3 presents an investigation where we encapsulate a metamaterial absorber unit cell with liquid crystals. We study both computationally and experimentally the tuning mechanism of the absorber as the liquid crystal refractive index is controlled as a function of the applied electric field strength and modulation frequency. In Chapter 4, we form a doped semiconducting metamaterial spatial light modulator with multi-color super-pixels composed of arrays of electronically controlled terahertz metamaterial absorbers. We computationally and experimentally study the independent tunability of each pixel in the spatial array and demonstrate high speed modulation.

Chapter 5 introduces a multiplex imaging approach by using a terahertz spatial light modulator to enable terahertz imaging with a single pixel detector. We demonstrate the capability for high speed image acquisition, currently only limited by the commercial software used to reconfigure the spatial masks. We also configure the system to capture high fidelity images of varying complexity. In Chapter 6, we show how a metamaterial absorber can be implemented into a detector focal plane array for high sensitivity, low mutual coupling, and broad angle performance. Finally, we summarize in Chapter 7 the achievements of the research presented and highlight the direction of future work.

ACKNOWLEDGEMENTS

The end to a wonderful chapter in my life is finally coming to a close. So many people have made this possible, and am so grateful for all of the support I have received over the years. I want to first thank my advisor, Prof. Willie Padilla, for taking a chance on me over six years ago and providing me with the chance of a lifetime; to be able to explore the world of metamaterials under his wing. He has allowed me the freedom to explore my ideas and curiosities, while providing me with the guidance, encouragement, and support necessary to continue to grow both as a physicist and as a person.

I want to also thank my undergraduate advisors at UCSD, Profs. David Meyer and Dimitri Basov. As a sophomore Physics major, I remember Dimitri asking in the first lecture if anyone would be interested in undergraduate research. As I approached him afterwards I couldn't have envisioned the course of events that would result. I want to thank everyone in the Basov lab, especially both Dimitri and Prof. Kenneth Burch who mentored me for the two years I was there. Thank you Kenny for your willingness to give me a second chance after I perfectly sanded off every single thin film sample we were all set to measure. Having mentored over a half-dozen undergraduates myself I can only hope that I have had the same profound influence on their careers and lives that you have had on mine.

My journey at Boston College has allowed me the great fortune of be surrounded by some amazing people as well as the opportunity to collaborate with a wonderfully diverse set of talented individuals. It has truly been a pleasure to have worked with Wenchen Chen, Xinliang Liu, Claire Watts, Chris Bingham, Dr. Kebin Fan, Dr. Salvatore Sato,

Nathan Landy, and the rest of the Padilla lab. Thank you to all the terrific people who I have had the pleasure of meeting and working with in the Physics Dept. at Boston College, especially Profs. Michael Naughton and Stephen Wilson for taking the time to be on my doctoral committee.

I have a wonderful collaborations with the groups of Prof. Sameer Sonkusale in the ECE Dept. at Tufts University, Prof. Richard Averitt in the Physics Dept. at Boston University, Prof. Sanjay Krishna in the ECE Dept. at the University of New Mexico, Profs. David Smith and Nan Jokerst in the ECE Dept. at Duke University, and lastly Prof. David Schurig in the ECE Dept. at the University of Utah. I especially thank Saroj Rout, Dr. Wangren Xu, Dr. Andrew Strikwerda, and John Montoya for all of their contributions which have allowed much of the work described in this thesis to be realized. I have learned an incredible amount from each one of you, and I can say with certainty that you have made my graduate experience something I will treasure for the rest of my life. Working alongside great people is an inspiration, and makes coming to the lab everyday a tremendous pleasure.

Lastly, I must thank all of my friends and family. My parents, Susan and Abe, have inspired me to push myself harder than I thought I was capable, their immense love and support has allowed me to go after my dreams without fear of consequence. I knew that coming to Boston would provide me the chance of the lifetime, but I was completely swept off my feet when I met my fiancé, Amanda, about half way through my studies. I am so blessed to be able to begin the next chapter of our lives together when we are married in a week! Thank you for having the patience to deal with me when I came home

late for weeks on end, to cheer me up when I was frustrated and distraught because things were awry in the lab, and most importantly for pushing me to finally graduate.

TABLE OF CONTENTS

ACKNOWLEDGEMENTS.....	i
TABLE OF CONTENTS.....	iv
LIST OF FIGURES	vi
1. Introduction	1
1.1. Overview of Metamaterials.....	2
1.1.1. Split ring resonators	3
1.1.2. Additional types of metamaterials	5
1.1.3. Metamaterial absorbers.....	7
1.1.4. Terahertz metamaterials.....	9
1.1.5. Dynamic metamaterials	10
1.2. Experimental techniques	11
1.2.1. Simulations	11
1.2.2. Homogenous parameter extraction	13
1.2.3. Fabrication methods.....	14
1.2.4. Terahertz time domain spectroscopy	14
1.2.5. Fourier transform infrared spectrometry.....	17
2. High speed terahertz modulation from metamaterials with embedded high electron mobility transistors.....	21
2.1. Design and fabrication	22
2.2. Results and discussion.....	25
2.2.1. THz Transmission with DC Biased HEMT	25
2.2.2. High frequency THz modulation	29
3. Liquid crystal tunable metamaterial absorber	32
3.1. Design and fabrication	32
3.2. Results and discussion.....	34
4. Metamaterial absorber terahertz spatial light modulator.....	43
4.1. Design and fabrication	43
4.2. Results and discussion.....	49

5. Terahertz single pixel imaging with an optically controlled dynamic spatial light modulator	58
5.1. Theory	60
5.1.1. Imaging Theory.....	60
5.1.2. Dynamic THz spatial light modulators	62
5.2. Experimental setup.....	65
5.3. Experimental Results and Discussion	68
5.4. Metamaterial SLMs.....	72
6. Microwave Metamaterial Detector Focal Plane Array.....	75
6.1. Design and fabrication	76
6.2. Results and discussion.....	81
7. Conclusions and future direction.....	87
7.1. THz compressive sensing.....	87
7.2. Bolometric imaging.....	89
BIBLIOGRAPHY.....	91
CURRICULUM VITAE.....	103

LIST OF FIGURES

Figure 1.1 Overview of magnetic split ring resonators (SRRs).....	4
Figure 1.2 The split ring resonator (SRR) resonant field distributions in the plane of the metamaterial.....	5
Figure 1.3 The electric coupled LC (ELC) resonant field distributions in the plane of the metamaterial.....	6
Figure 1.4 Overview of electrically coupled LC resonators (ELCs)	6
Figure 1.5 Design and operational principle of metamaterial absorbers (MMAs).....	8
Figure 1.6 A schematic of the THz time domain system that was setup for the study of the THz modulation	16
Figure 1.7 THz data collected by THz-TDS system with an open aperture reference and optical chopper used to lock into the THz signal.....	16
Figure 1.8 Pictures of the Bruker Vertex 80V Fourier transform infrared spectrometer (FTIR) and the Hyperion 2000 FTIR microscope.	18
Figure 1.9 THz data collected by FTIR	19
Figure 2.1 Design and structure detail of the HEMT based electronically controlled THz metamaterial modulator	22
Figure 2.2 The simulated I-V characteristics of the HEMT	24
Figure 2.3 Frequency dependent transmitted electric field for the HEMT / metamaterial device as a function of bias.....	26
Figure 2.4 Simulated differential transmission for various 2D carrier concentrations N_s	27
Figure 2.5 Time domain data for modulation at frequencies of 100 kHz, 1 MHz and 10 MHz	30
Figure 3.1 Design and operational principle of the tunable metamaterial absorber	33
Figure 3.2 Experimentally measured absorption of the metamaterial absorber	36
Figure 3.3 Numerical simulations of the metamaterial absorber.....	38
Figure 3.4 Resonant terahertz fields of the metamaterial absorber	40
Figure 3.5 Effective optical constants of metamaterial absorber.....	41
Figure 4.1 Design and structure detail of the electronically controlled THz metamaterial absorber based spatial light modulator (MMA-SLM)	44
Figure 4.2 Schematic representation of the fabrication procedure of the epitaxial n-doped GaAs layer pixel definition.	46
Figure 4.3 Schematic representation of the fabrication procedure of the control chip.	47
Figure 4.4 Schematic representation of the fabrication procedure for final device assembly.....	48
Figure 4.5 Voltage dependent current (IV) profile	48
Figure 4.6 Experimentally measured and computationally simulated frequency dependent reflectance of the metamaterial absorber shown for each color sub-pixel.....	50
Figure 4.7 Numerical simulation results of the metamaterial absorber	53

Figure 4.8 Simulation results for reflected amplitude and phase modulation shown for each color sub-pixel	55
Figure 4.9 Spatial light modulator performance	56
Figure 5.1 Schematic depicting multiplex imaging process where the spatial modulation of a formed image allows for the reconstruction using a single pixel detector.	60
Figure 5.2 Transmission of THz radiation through ρ -Si wafer as a function of frequency for several different optical fluence values	63
Figure 5.3 Overview schematic of experimental THz imaging setup	65
Figure 5.4 Comparison of THz imaging with raster scan masks and <i>S</i> -matrix masks	69
Figure 5.5 THz imaging with high-resolution <i>S</i> -matrix masks.....	72
Figure 5.6 Optically reconfigurable THz masks with metamaterials	73
Figure 6.1 System architecture of our metamaterial microwave power detector array	77
Figure 6.2 Numerical simulations of metamaterial absorber	79
Figure 6.3 Experimental measurements in anechoic chamber for the center pixel on the MMA / FPA	82
Figure 6.4 System architecture consists of three boards.....	84
Figure 6.5 S-parameter data shows the transmission without (S_{31} blue curve) and with (S_{41} gold curve) the addition of the impedance matching and low noise amplifier (LNA)	84
Figure 6.6 Off-angle performance characterization of the MMA / FPA at 2.5 GHz.....	85
Figure 7.1 Next generation terahertz imaging system utilizing metamaterial spatial light modulator (SLM)	88
Figure 7.2 Metamaterial absorber (MMA) pixel array used for bolometric mm-wave to infrared (IR) imaging	89

CHAPTER 1

1. Introduction

The ability to dynamically control the response of a photonic device to electromagnetic radiation is a very powerful concept that has long been a goal of scientists and engineers. Metamaterials are engineered electromagnetic materials which enable the precise control over light and are optimistic candidates to achieve this degree of freedom. Over the past decade, interest of the scientific and engineering communities for developing such metamaterial structures has been continuous and increasing. Experimental realizations of negative index of refraction [1,2], invisibility cloaks [3], and perfect lensing [4,5] all served to ignite the field. As metamaterial research continues to mature, demonstrations of practical devices will become increasingly important for continued growth. Metamaterial based sources, detectors and modulators that could be used in communication systems, or for imaging and sensing applications, would go far to validate the initial promise of the technology.

This is especially true at terahertz (THz) frequencies where components necessary to efficiently manipulate THz radiation remain in need of substantial development in order to provide realistic solutions [6]. THz radiation has great potential for imaging applications [7,8] due to its ability to penetrate most dielectric materials and non-polar liquids. Its harmless interaction with human tissue suggests imaging in this regime has immediate applicability in the fields of biodetection [9], system inspection [10], and detection of illegal drugs [11]. However, a significant limitation currently preventing wide-spread THz imaging is the absence of efficient sources and detectors operating

between 0.1 and 10 THz - a band of the electromagnetic spectrum often referred to as the "THz gap" [12].

Metamaterials have proven to be very resourceful at THz frequencies in achieving material response behaviors that do not exist in nature and can be designed to possess properties with significant advantages over conventional materials. The work presented here explores and demonstrates several different paths to achieve dynamic THz metamaterials. We hybridize metamaterials by embedding an assortment of exotic materials including semiconductors and liquid crystals to efficiently control the material response. We also explore several paths in which metamaterials can be leveraged to form imaging systems. This includes the development of spatial light modulators (SLMs), which we demonstrate can be used for THz single pixel imaging.

1.1. Overview of Metamaterials

A commonly accepted definition for metamaterials is that of an artificial material which has an effective material response that is determined by the design geometry and not that of the constituent materials. This definition of metamaterials is not restricted solely to electromagnetics, but can also be applied to many different areas of physics including acoustic [13] and thermodynamic [14] systems. In electromagnetics, Maxwell's equations and the constitutive relations describing the electromagnetic theory of light present a description governing all classic light-matter interactions. Naturally occurring materials have electronic properties that are classified as insulators, conductors or semiconductors. Ultimately, it is the atomic structure of each material that determines the exact nature of the electronic behavior and the resulting optical constants that influence how impinging electromagnetic radiation interacts in accordance with Maxwell's equations. In a similar

fashion, metamaterials are formed by taking very subwavelength ($\lambda/10$) structures to function as electric and magnetic dipoles that behave analogously to atoms inside a bulk homogeneous material. The macroscopic electromagnetic material response is thus defined in terms of an effective dielectric permittivity [ϵ_{eff}] and magnetic permeability [μ_{eff}] parameters [15-17]. These effective constitutive parameters provide a useful way to understand electromagnetic wave interaction with metamaterials, making the calculation of the complex quasistatic local-field structure unnecessary [18].

1.1.1. *Split ring resonators*

The magnetic properties of split ring resonators (SRRs) was proposed long before the advent of metamaterials [19], though John Pendry was the first to propose a structure composed of an array of SRRs and quantifying the array as an artificial material possessing an effective magnetic response [15]. In addition to describing the concept of forming an effective medium the relationship relating the SRR unit cell geometry to the material response was also derived. The SRRs shown in Fig. 1.1(a) are built from nonmagnetic conducting sheets, whose material response shown in Fig. 1.1(c) can be determined solely by the SRR geometry (Pendry described a similar concept for an effective electric response with an array of thin wires [20]). The frequency dependent μ_{eff} can be expressed in the form similar to a Lorentz oscillator [15,21]

$$\mu_{eff}(\omega) = 1 - \frac{F\omega^2}{\omega^2 - \omega_0^2 + i\Gamma\omega} \quad (1.1)$$

where F is the geometrical factor, ω_0 is the resonance frequency, Γ is the resistive loss in the resonating SRR. The influence of the constituent metal conductivity σ influences the overall oscillator strength, but in practice this is always limited by the underlying

supporting dielectric, whose losses are much more significant in comparison to the ohmic losses found in metal conductors in microwave and THz metamaterials.

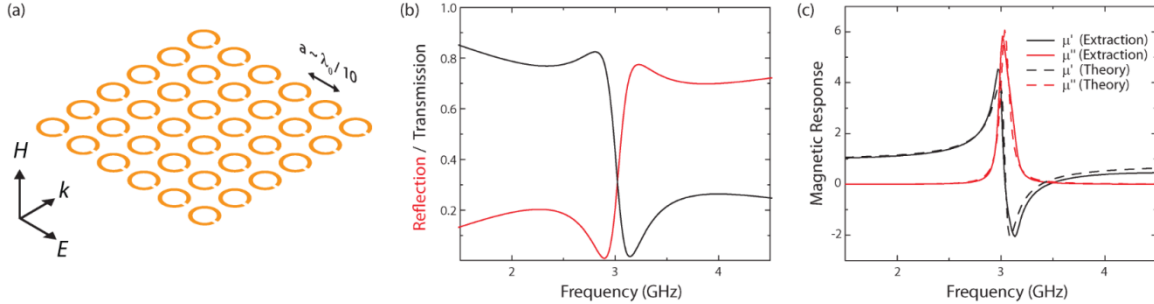


Figure 1.1 Magnetic split ring resonators (SRRs). (a) Incident electromagnetic wave propagates across SRR array, where the element spacing a is one order of magnitude smaller than the free space wavelength λ_0 . (b) The simulated reflection and transmission for an SRR with $a = 10$ mm. (c) The extracted magnetic response (solid curves) from the simulation results shown in (b) and method is discussed in 1.2.2, also shown is the response when fit with the theoretical model listed in Eq. 1.1, where $F = 0.20$, $\omega_0 = 2\pi \times 3.03$ GHz, and $\Gamma = 0.10$ s⁻¹.

The resonant response of metamaterials typically refers to the fundamental mode, corresponding to the lowest frequency excited resonance. For an SRR, the fundamental mode can be excited magnetically with an incident electromagnetic wave as shown in Fig. 1.1(a). In Fig. 2 the resonant current, electric, and magnetic field distributions are respectively shown for the excited SRR. At this frequency, the oscillating magnetic field component of the incident electromagnetic wave induces an oscillating current that causes charge of opposite polarity to accumulate in the gap of the split ring, thereby producing a strong enhancement of electric field. The magnetic and electric field enhancement shown in Fig. 2(b,c) are 90 degrees out of phase where the peak magnetic field corresponding to a maximum current density is shown in Fig. 1.2(a).

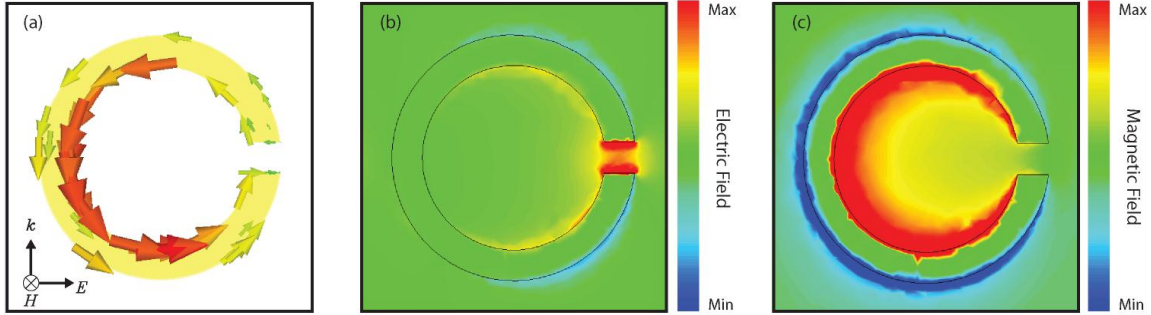


Figure 1.2 The split ring resonator (SRR) resonant field distributions in the plane of the metamaterial where (a) shows the resonant current density, (b) the maximum electric field, and (c) plots the maximum magnetic field.

The resonant response of SRRs, and for most metamaterials, can be described conceptually as an LC circuit [22], where the inductance, L , comes from the path length and area enclosed by the ring, and the capacitance, C , from the split gap. From an engineering perspective this is useful as the resonance frequency $\omega_0 = 1/\sqrt{LC}$, meaning that by simply scaling these variables one can achieve a resonant response at nearly any frequency, though in practice material parameters in general vary considerably across the electromagnetic spectrum. This description is also useful in conceptualizing dynamic metamaterials, wherein the majority of research focuses on different mechanisms of controlling the capacitance associated with the split gap (this will be outlined in more detail below in section 1.1.5).

1.1.2. *Additional types of metamaterials*

SRRs have proven to be of immense interest due to their magnetic response, but many alternative structures have also been proposed with different functionalities. Electric ring resonators (ERRs), also known as electrically coupled LC (ELC) resonators, have a modified asymmetric geometry compared to conventional SRRs, which enables them to effectively cancel the magnetic moment and only couple to the incident electric field

vector as illustrated in Fig. 1.3 [23,24]. The electric response is shown in Fig. 1.4(c), similar to that of the magnetic response of the SRR in Fig. 1.1(b), where ϵ_{eff} takes the form [25,26]

$$\epsilon_{eff}(\omega) = \epsilon_{\infty} - \frac{F\omega^2}{\omega^2 - \omega_0^2 + i\Gamma\omega} \quad (1.2)$$

where ϵ_{∞} is the frequency independent dielectric permittivity in the supporting dielectric substrate that is due to the contribution of bound electrons. These studies have also investigated the different levels of response for modified ERR structures having created a range of polarization sensitive and insensitive (four-fold symmetry) designs [24].

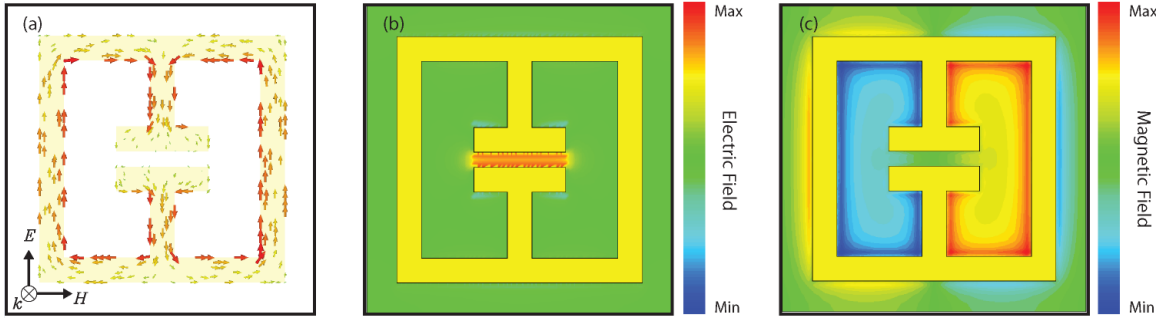


Figure 1.3 The electric coupled LC (ELC) resonant field distributions in the plane of the metamaterial where (a) shows the resonant current density, (b) the maximum electric field, and (c) plots the maximum magnetic field.

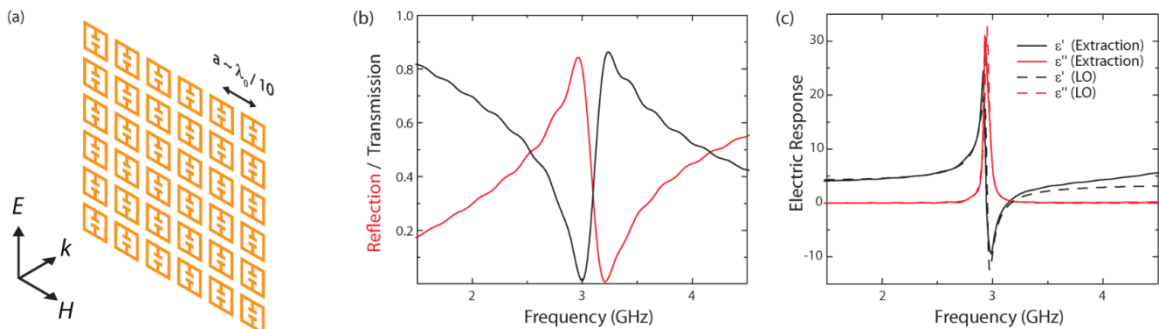


Figure 1.4 Electrically coupled LC resonators (ELCs). (a) Incident electromagnetic wave propagates normal to ELC array, where the element spacing a is one order of magnitude smaller than the free space wavelength λ_0 . (b) The simulated reflection and transmission for an ELC with $a = 10$ mm. (c) The extracted electric response from the simulation results shown in (b) and method is discussed in 1.2.2, also shown is the response when fit

with the theoretical model listed in Eq. 1.2, where $\epsilon_\infty = 4.3$ (FR4 dielectric), $F = 0.55$, $\omega_0 = 2\pi \times 2.96$ GHz, and $\Gamma = 0.05$ s⁻¹.

Chiral metamaterials have been demonstrated to have unique interactions for either handedness of light [27], and Pendry demonstrated how this could be exploited in generating an alternative means of achieving a negative index of refraction material [28]. Metamaterials can be designed to be extremely subwavelength ($\sim\lambda_0/2000$) [29], thus allowing for several different approaches involving multiple fundamental resonant frequencies to form the effective material response. Some studies have demonstrated this by using bipartite structures within a planar design [30], or by stacking metamaterial cells with slightly varying geometry thereby increasing the resonant bandwidth of the effective material response [31]. Complimentary structures have been explored and theoretically explained using Babinet's principle [32,33]. These structures display a reversal of the transmission and reflection as compared to the regular structure.

1.1.3. *Metamaterial absorbers*

Metamaterials can be designed to yield highly efficient absorption by careful tailoring of their electric and magnetic response functions. Metamaterial absorbers (MMAs) have sparked significant interest since their first demonstration [34,35] and hold great potential for use in applications ranging from thermal emitters [36] and energy harvesting [37], to sensors and narrow band absorbers [38]. The ability of sub-wavelength metamaterial unit cells to completely absorb incident electromagnetic energy has been demonstrated across much of the electromagnetic spectrum as depicted in Fig. 1.5(a) [34,39-41]. One key design feature afforded by metamaterials is the ability to engineer materials for matching the impedance $Z(\omega) = \sqrt{\mu(\omega)/\epsilon(\omega)}$ of the MMA to that of free space, thereby minimizing the reflectance. The resonant nature of the MMA structures generates high

electric fields in the gap, completely dissipating the incident energy into a combination of dielectric and ohmic losses (See Fig. 1.5(c)) [38,39].

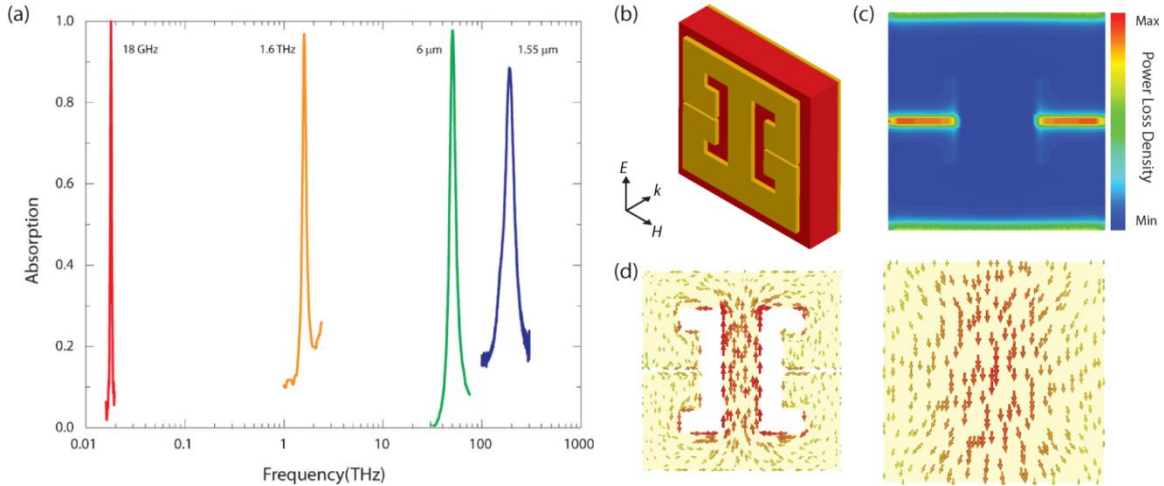


Figure 1.5 (a) Metamaterial absorbers (MMAs) have been experimentally demonstrated to achieve near perfect absorption across the electromagnetic spectrum ranging from microwave to optical [41]. (b) Schematic of MMA unit cell where the electric resonator is on top of a dielectric spacer with a ground plane on the backside. (c) Power loss density shown in metamaterial plane directly underneath the double electric ring resonator (dERR). (d) Current densities shown for the dERR and ground plane.

Metamaterial absorbers typically consist of two metallic layers spaced apart by virtue of a dielectric spacer [35]. The top metal layer is geometrically patterned in order to strongly couple to a uniform incident electric field. By pairing the top layer with a metal ground plane, a mechanism for coupling to the magnetic component of light is created - see Fig. 1.5(b). The magnetic response forms anti-parallel currents in the top and bottom metal layers, whereas the electric response resonates the electric resonator shown in Fig. 1.5(d) [34]. Altering the geometry of the metallic pattern and dielectric thickness enables tuning of the effective material response parameters allowing for both impedance matching and strong absorption at nearly any desired frequency. MMAs are quite remarkable and have been demonstrated experimentally to possess many interesting properties such as polarization sensitive and insensitive designs [26], absorb incident

radiation over a wide incident angles for both TE and TM polarizations [42], multi-absorption bands [43], and dynamic MMAs can be formed [44,45].

1.1.4. *Terahertz metamaterials*

Metamaterials that are resonant at THz frequencies have demonstrated the ability to generate material properties not easily obtainable in nature, most notably a magnetic response that is particularly rare at THz frequencies [46]. The experimental characterization of many different types of materials has shown that many non-metallic and non-polar medium possess relatively weak interactions with incident THz radiation [47]. Alternatively, materials can be strongly opaque as in the case of metals, which are highly reflective, or water vapor which is strongly absorptive [48-50]. Metamaterials allow for control of both electric and magnetic response providing a path to achieving responses that are absent within natural existing materials. These artificial materials contain the added benefits of being able to possess dynamic control of the material response as well as spectral selectivity. Both of which are useful properties for the development of novel sensing and imaging systems that would provide the capability for identification of molecular compounds and or chemicals. Many of these substances have specific THz signatures i.e., molecular vibrational absorptive modes serving as chemical fingerprints. In addition, such devices can be deigned to operate within an atmospheric transmission window to provide suitable visibility at manageable working distances [47].

The length scale associated with metamaterials resonant at THz frequencies is on the order of several microns with respect to the smallest feature sizes, and tens of microns for a typical unit cell dimension. The size of these features permits the use of conventional microfabrication techniques resulting in cost effective, highly efficient

means of production. Common substrates for THz metamaterials are semi insulating gallium arsenide (SI-GaAs) and high resistivity silicon (ρ -Si) which allow for minimal absorption through the substrate. Free standing (substrate free) metamaterials have also been fabricated on thin layers of silicon nitride [51], polyimide [52], parylene [53], and silk [54]. Many different types of THz metamaterials have been experimentally studied and have demonstrated extraordinary responses, these include: negative index of refraction [55,56], chiral structures [57], metamaterial absorbers [39], and extraordinary optical transmission [58].

1.1.5. *Dynamic metamaterials*

In recent years demonstration of frequency agile and tunable metamaterials have shown great potential for applications at THz frequencies. Various methods have been utilized to achieve amplitude and frequency modulation including photodoping [59,60], electronic control [61-63], temperature control [64], and microelectromechanical systems (MEMS) [65]. Similar type designs have also shown the capability to modulate the electromagnetic phase [66]. Electronic control is of particular interest to many because of the ability to integrate such devices with electronics and for achieving high modulation speeds [63].

The underlying mechanisms behind each of these forms of control rely on very similar principles. In the case of MEMS integrated metamaterials, the physical geometry of the resonant structure can be reconfigured to alter the electromagnetic response, as was demonstrated through either a cantilever design [65] and comb-drive actuation [67]. As discussed in section 1.1.1, the electric field located in the split gap formed by the SRR has an extremely large field enhancement factor; as a result the resonant response is highly influenced by the underlying dielectric. The complex permittivity of the substrate

$\tilde{\epsilon}_s = \epsilon_1 + i\epsilon_2$, is composed of the real and imaginary components, which can be controlled through various mechanisms and utilized to achieve tunability in the resonant metamaterial structure. Changes in ϵ_1 are inversely proportional to a shift in the resonant frequency, whereas ϵ_2 is directly related to the damping factor of the resonance. Materials that have independent control of the real and imaginary components are ideal from an application prospective, allowing one to generate efficient frequency shifters or amplitude modulators.

1.2. Experimental techniques

Experimentalists exploring the world of metamaterials have many tools with which to create and characterize samples. Historically speaking, in experimental condensed matter physics, investigations of materials have consisted of long cycles for the development and discovery of new materials. Material growth is run by specialists, where years of effort are often required to produce samples of sufficient quality. For optical measurements, single crystal samples can be rather difficult to obtain with the necessary size to characterize. In the world of metamaterials many of these concerns are alleviated due to optimization cycles that combine experiment and simulation. The fabrication techniques which utilize standard clean room methods such as UV lithography and E-beam writing are able to produce large area and high quality samples.

1.2.1. Simulations

Ideally, creating analytical models would allow one to extract important information about the underlying mechanisms of metamaterials, but this is quite difficult to accomplish for typical metamaterial structures of complex geometries. Full wave 3D electromagnetic simulations of metamaterials offer a theoretical tool that has contributed

to the exponential growth occurring within the field. Researchers can accurately model the response of complex composite structures computationally by using known material parameters, such as the conductivity for Cu ($\sigma_{Cu} = 5.96 \times 10^7$ S/m) and Au ($\sigma_{Au} = 4.56 \times 10^7$ S/m), along with various dielectric materials such as Si ($\epsilon_{Si} = 11.9$) and GaAs ($\epsilon_{GaAs} = 12.9$), to calculate the reflection and transmission coefficients. The basic principles behind these numerical methods are to discretize the unit cell with appropriate boundary conditions, and then solve Maxwell's equations in partial differential form at each point within the grid.

There are classically two main approaches which are used by researchers, with the first being the finite difference time domain (FDTD) method [68]. FDTD is very attractive in order to simulate the response over a large bandwidth in a computationally efficient manner. The second method is the finite element method (FEM) which solves the discretized form of Maxwell's equations for a specified frequency, i.e. at a fixed wavelength [69]. This method can generate improved accuracy relative to the FDTD solver by generating a more complex tetrahedral meshing. This conforms to non-linear geometries and adaptively scales local meshing cells to produce higher mesh densities within the high field regions.

We primarily use CST Microwave Studio commercial solver in our research which uses a slightly different approach referred to as the finite integration technique (FIT). Their software functions as a FDTD equivalent transient solver and a FEM equivalent frequency solver. FIT preserves Maxwell's equations in integral form. In general, is a more robust method in comparison to classic FDTD methods. This allows for increased efficiency in solving larger and more complex structures. One additional

advantage of using this software is the flexibility to integrate simulation results into circuit designs. This is used in the work described in Chapter 6 where we have used a metamaterial absorber to form a focal plane array at microwave frequencies. The electromagnetic response of a metamaterial with impedance matching circuit was calculated using this feature.

1.2.2. Homogeneous parameter extraction

Determining the constitutive parameters of materials from optical spectroscopic measurement is a powerful technique that has contributed invaluable information including the frequency dependent optical constants for a host of materials. Conventional transport measurements and electronics can characterize DC behavior and RF responses, but optical characterization is useful for characterization of various materials from millimeter-wave to UV. Metamaterials can also be investigated with similar techniques to determine the effective response of the artificial material.

A transfer-matrix formalism allows for a simple isotropic, homogeneous solution for the extraction of the material parameters from the measured complex reflection (S_{11}) and transmission (S_{21}) coefficients [16,70]:

$$n = \frac{1}{kd} \cos^{-1} \left[\frac{1}{2S_{21}} (1 - S_{11}^2 + S_{21}^2) \right] \quad (1.3)$$

$$Z = \sqrt{\frac{(1 + S_{11})^2 - S_{21}^2}{(1 - S_{11})^2 - S_{21}^2}} \quad (1.4)$$

where the wavenumber of the incident wave is $k = 2\pi/\lambda$ and d is the unit cell dimension. The relationship between the refractive index n and impedance Z to ϵ_{eff} and μ_{eff} are the following

$$n = \sqrt{\varepsilon\mu}, \quad Z = \sqrt{\frac{\mu}{\varepsilon}} \quad (1.5)$$

thus the full material response can be determined. Experimentally, it is very difficult to achieve accurate measurements of both the reflection and transmission coefficient, but in simulation this can be done easily.

1.2.3. Fabrication methods

In most general cases THz metamaterials can easily be fabricated using standard cleanroom photolithography; this allows for easy integration with different substrates and materials for application specific functionality. Standard mask aligners tolerate up to 5 inch mask size allowing for fabrication of samples on wafers up to 4 inches in diameter. Typical feature sizes that can be obtained in a cleanroom are down to 2 μm resolution (with slight rounding of sharp features below 4 μm). Au is conventionally selected as the metal deposited to form the metamaterials, along with thin a titanium (Ti) adhesion layer. The total thickness is between 100 and 200 nm, chosen to be sufficiently large compared to the penetration depth (75 nm at 1 THz) [71]. Many of the precise fabrication details can be found in the early literature and, while many of the hybrid devices presented in this manuscript utilize these techniques, we also present several new approaches that are discussed in more detail in the subsequent chapters.

1.2.4. *Terahertz time domain spectroscopy*

THz time domain spectroscopy (THz-TDS) is a technique that was first developed in the late 1980's and whose science quickly matured within the 1990's becoming one of the most useful tools in performing THz spectroscopy and uncovering the dynamics within ultrafast materials systems [72,73]. These room temperature systems offer SNR

performance in excess of 10,000 thus providing a very accurate means of characterizing materials from 0.1 to over 4 THz with up to 1 GHz resolution [72,74]. A typical THz-TDS system using photoconductive antennas is shown schematically in Fig. 1.6 where an optical chopper has been substituted for THz metamaterial modulator that is discussed in more detail in Chapter 2. A 532 nm wavelength 4 W neodymium-doped yttrium aluminum garnet (YAG) laser beam is used to pump the titanium sapphire (Ti-sapphire) ultrafast laser that typically outputs a train of optical pulses centered about 800 nm wavelength (~ 100 fs in duration), at a repetition rate that varies from 70 to 100 MHz. The beam is split into two different paths with one path going through a controllable delay stage, and the other path being a fixed distance. One beam is used for THz generation, creating a THz pulse of ~ 1 ps duration, the THz beam is then focused through the sample and directed onto the detector. The detector is sensitive to the incident THz electric field $E_{THz}(t)$ for time increments that are much less than 1 ps, thus by scanning the delay line a measure of the $E_{THz}(t)$ as a function of time can be accomplished. An example of the measured time waveform is shown in Fig. 1.7(a), where the Fourier transform of the time signal calculates the frequency dependent complex electric field spectrum $\tilde{E}_{THz}(\omega)$ (magnitude shown in Fig. 1.7(b)). The spectral resolution is inversely proportional to the length of the temporal scan.

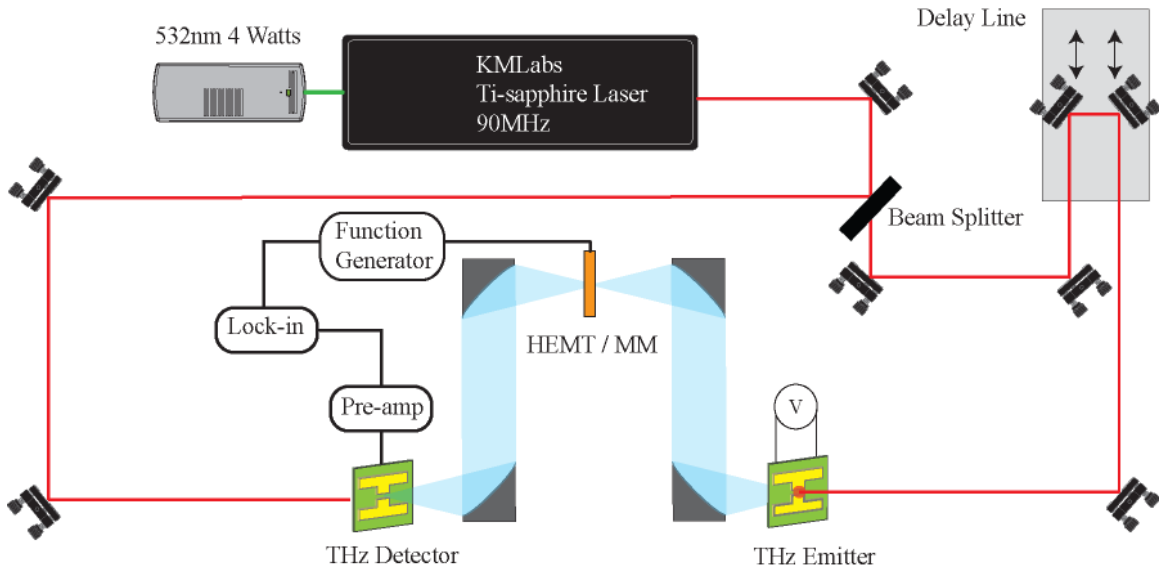


Figure 1.6 A schematic of the THz time domain system that was setup for the study of the THz modulation discussed in Ch. 2 where we demonstrate high speed THz modulation with a hybrid device consisting of high electron mobility transistors (HEMT) monolithically integrated with metamaterials (MM).

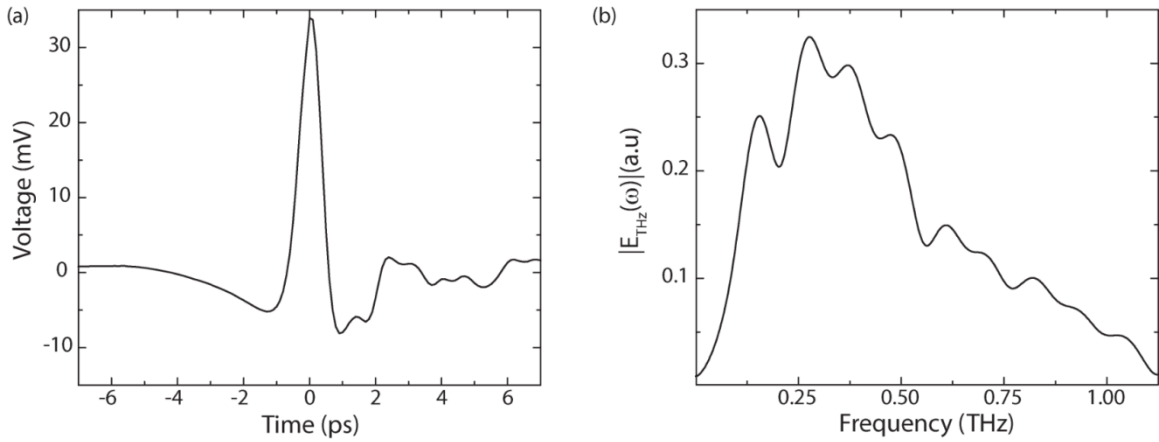


Figure 1.7 THz data collected by THz-TDS system with an open aperture reference and optical chopper used to lock into the THz signal. (a) The raw data taken from the lock-in is output in Volts. (b) The resulting spectrum calculated by taking the Fourier transform of the data shown in (a) after zero padding.

The generation antenna typically uses a stripline antenna fabricated on a GaAs substrate (Band gap of 1.42 eV = 874 nm), where the two lines of the antenna have a DC bias set across them. The optical beam excites free carriers in the GaAs generating a current which radiates THz electromagnetic radiation where the central emission

frequency can be controlled by virtue of the stripline spacing (~ 0.3 THz for $80 \mu\text{m}$ spacing [See Fig. 1.7(b)], and $E_{\text{THz}}(t)$ is proportional to the time derivative of the current density generated. On the detector side a dipole antenna is used on top of a substrate material with optical generated carriers that boast very short carrier lifetimes; such as low temperature grown LT-GaAs, Er:GaAs nanoislands, or ion-implanted silicon-on-sapphire (SOS) [75]. The antenna is unbiased and a current is generated by combination of the photogenerated carriers which are accelerated by local THz electric field vector. Due to the short carrier lifetime the current generated $I(t)$ is directly proportional to $E_{\text{THz}}(t)$ [74]

$$I(t) \sim \int_{-\infty}^t \sigma(t) E_{\text{THz}}(t - \tau) d\tau \quad (1.5)$$

where $\sigma(t)$ is the time dependent conductivity relating the free carriers optically excited in the substrate. The current is passed respectively to a preamplifier and lock-in amplifier and outputs a measured DC voltage proportional $E_{\text{THz}}(t)$.

1.2.5. *Fourier transform infrared spectrometry*

An alternative to characterizing metamaterials with a THz-TDS system is using a commercial Bruker Vertex 80 V Fourier transform infrared spectrometer (FTIRs) shown in Fig. 1.8(a). This instrument is a vacuum system and uses a Michelson interferometer to perform broadband spectroscopic measurements over a continuous range from 5 cm^{-1} to $50,000 \text{ cm}^{-1}$ ($\lambda \sim 2 \text{ mm}$ to 200 nm), with better than 0.2 cm^{-1} (6 GHz) spectral resolution. Each spectral region requires a specific configuration to achieve optimal signal to noise (SNR), where at THz frequencies a mercury (Hg) arc lamp is used as a source, the beamsplitter is made from thin mylar ($6 \mu\text{m}$ to $125 \mu\text{m}$), and the detector is a liquid

helium cooled Si bolometer made by Infrared Laboratories. The FTIR is coupled to a Hyperion microscope (See Fig. 1.8(b)) which allows us to perform THz microscopy down to 2 THz.

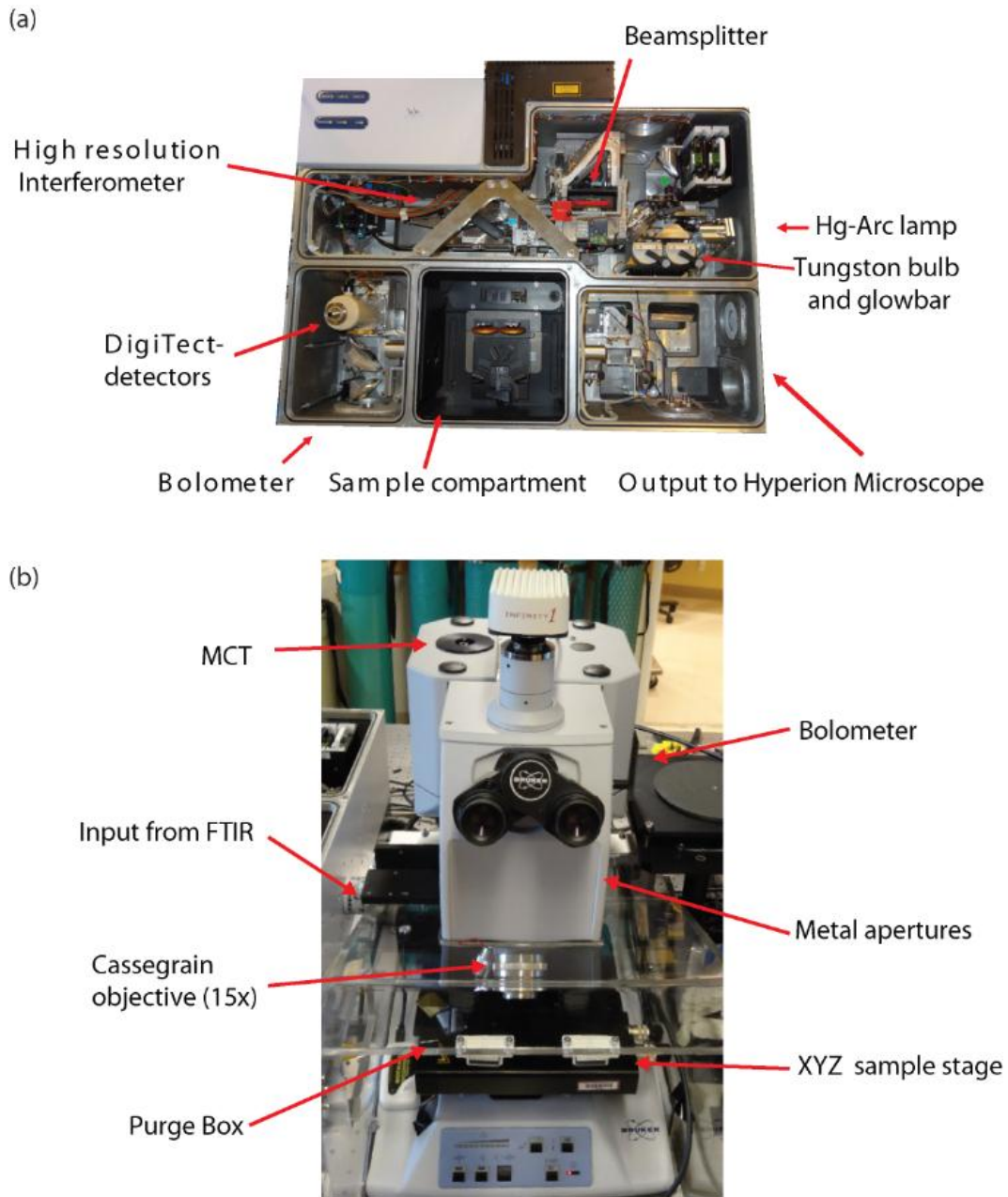


Figure 1.8 Pictures of the Bruker Vertex 80V Fourier transform infrared spectrometer (FTIR) and the Hyperion 2000 FTIR microscope.

Interferometric infrared spectroscopy utilizing two-beam interference was originally designed by Michelson in the late 19th century [76]. The theory behind the operation is that by dividing the beam into two paths and then recombining the beam after introducing a controllable difference in path length, interference between the two beams occurs. The intensity dependence on the path difference, referred to as the interferogram, is shown in Fig. 1.9(a). The interferogram is measured by a single detector where the Fourier transform of the interferogram extracts the wavelength dependent intensity spectrum shown in Fig. 1.9(b) [77] (This is analogous to how the THz-TDS relates the time dependent electric field waveform to the frequency dependent electric field spectrum). In the Bruker system, the beam is split into two separate paths by use of a beamsplitter, where one path reflects off a stationary mirror, and the other beam reflects off of a movable mirror which oscillates back and forth with a constant mirror velocity. The recombined beam transmits through the sample chamber where focusing mirrors direct the beam into the detector (Si-bolometer for THz, MCT for Mid-Infrared (MIR), and several different DigiTect-detectors for detecting in the near-infrared (NIR) to UV).

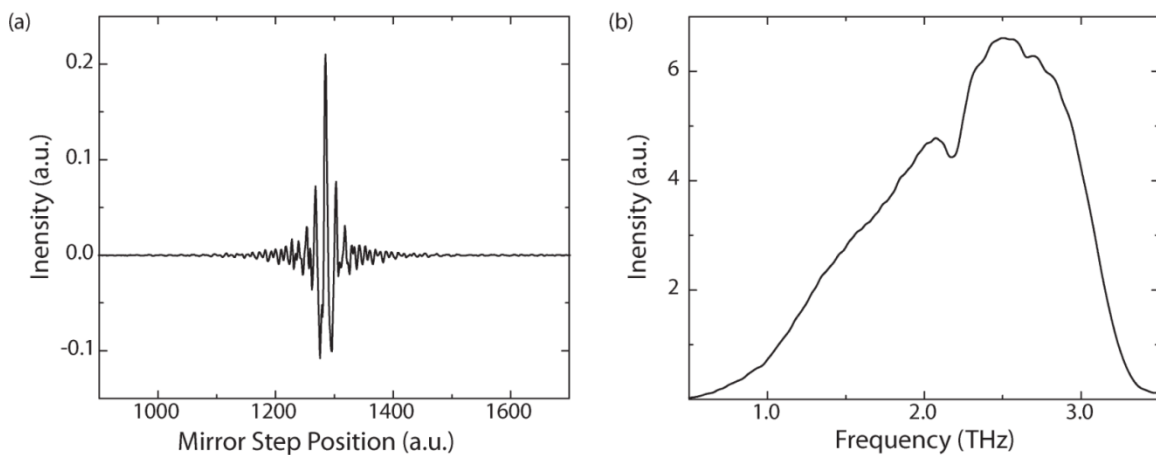


Figure 1.9 THz data collected by FTIR. (a) The interferogram plots the measured intensity as a function of mirror step position. (b) The resulting spectrum calculated by taking the Fourier transform of the interferogram shown in (a).

CHAPTER 2

2. High speed terahertz modulation from metamaterials with embedded high electron mobility transistors

Another area of significant research is the use of two-dimensional electron gases (2DEGs) in high electron mobility transistors and their interaction with THz waves. Studies have demonstrated the ability to create the trifecta of emission [78], detection [79], and modulation [80] of THz electromagnetic waves. The work of Dyakonov and Shur [81,82], has demonstrated that the 2DEG instability in short channel HEMTs has a resonant response to electromagnetic radiation at a frequency governed by the size and shape of the channel, i.e. the geometrical plasmon frequency. Tuning the plasmon resonant frequency to the incident THz wave has been used to create detectors, mixers and multipliers. Due to the non-radiative nature of 2DEG plasma oscillations (2DPs), the HEMT architecture has been implanted into a variety of structures mainly based on metal wire gratings. These structures have shown broadband THz electromagnetic response at temperatures up to 300 K.

When implemented as THz modulators these devices have demonstrated significant advantages over alternative architectures, such as quantum well structures which require cryogenic temperatures, and liquid crystals which possess relatively slow speeds [83,84]. HEMT devices have thus far been limited to relatively low transmission modulation values of less than 3%, and maximum modulation frequencies of 10 kilohertz (kHz) [85]. Here we present a hybrid HEMT / metamaterial device that utilizes monolithic integration of transistors *at the metamaterial unit cell level* and is able to

perform as an intensity modulator at terahertz frequencies with switching speeds up to 10 MHz [63].

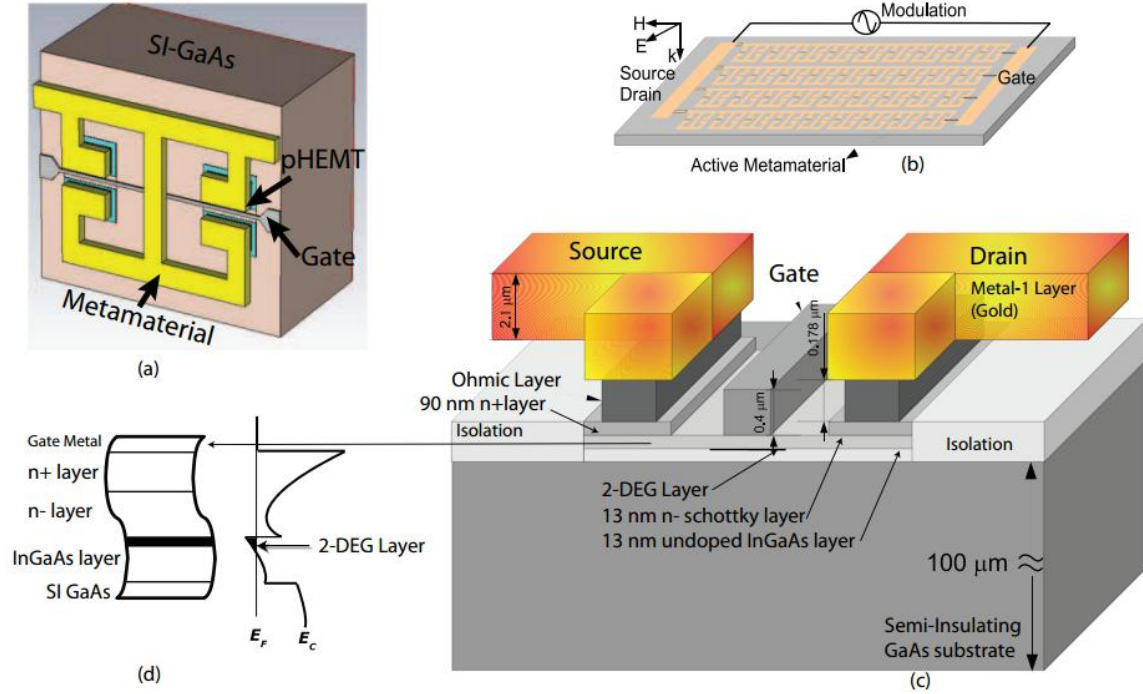


Figure 2.1 Design and structure detail of the HEMT based electronically controlled THz metamaterial modulator. (a) Single unit cell of the metamaterial element, as modeled for simulation. The HEMT is identified and lies under each split gap of the metamaterial. (b) Schematic depicting the entire HEMT / metamaterial device, and the polarization orientation of the incident THz wave is shown. (c) Cross-sectional view of the HEMT / metamaterial device in proximity to the split gap. (d) Band diagram detailing the 2DEG layer in the undoped InGaAs at the interface with the Schottky layer.

2.1. Design and fabrication

The sample was constructed using a commercial GaAs technology which consisted of three metal layers, an enhanced mode pseudomorphic HEMT, and a silicon nitride encapsulating dielectric, see Fig. 2.1. The technology utilized for this study is primarily used for mobile phone applications and to our knowledge this is the first time this has been used for THz metamaterial applications. The top metal layer, 2.1 μm thick gold, is patterned to form the metamaterial layer [63]. A different metal layer forms the gate of

the device and is also used for connecting all the gates within the same row. A 0.176 μm thick ohmic layer, which is also utilized as a routing layer, was primarily used for connecting the source and drain of the HEMT to the metamaterial. The source and drain are shorted through the metamaterial as a direct consequence of the metamaterial structure we have selected.

The metamaterial geometry used in this work is based on the electric split-ring resonator (ESRR) [23,24], and a detail of the unit cell is shown in Fig. 2.1(a). Each unit cell consists of two single rings butted together with their split gaps at the outside to accommodate design rules specific to the implemented technology. The line width of the metamaterial is 4 μm and the split gap is 3 μm . The metamaterial had the dimensions of 42 μm wide by 30 μm in height. A periodic array of these unit cells as shown in Fig. 2.1(b) was fabricated, with period of 55 μm x 40 μm , and a total size of 2.75 x 2.6 mm^2 with 3200 elements total. Metamaterial elements are fabricated on a 100 μm thick semi-insulating (SI) GaAs substrate.

A HEMT lies underneath each of the split gaps of the metamaterial element, (two per unit cell), as shown in cross-section in Fig. 2.1(c). The gate length is 0.5 μm and has a width 5 μm for each device. The HEMT is constructed using pseudomorphic undoped InGaAs and a lightly doped Schottky layer, each 13 nm thick, creating a heterojunction. A 2DEG is formed in the undoped InGaAs channel layer as predicted by the band diagram at the interface (Fig. 2.1(d)) [86]. Unlike traditional FETs, this channel is formed in an intrinsic (undoped) crystal, resulting in very high mobility ($\sim 3000 \text{ cm}^2/\text{V}\cdot\text{s}$) and charge density ($\sim 1.5 \times 10^{12} \text{ cm}^{-2}$) at room temperature, thus enabling fast conduction

even at THz frequencies. We simulated the DC behavior of the device using Agilent's Advanced Design System (ADS) software. The dependence of the current between the source and drain terminal (I_{DS}) on the gate bias voltage (V_{GS}), and on the drain to source electric field (E_{DS}) is shown in Fig. 2.2(a) and (b), respectively.

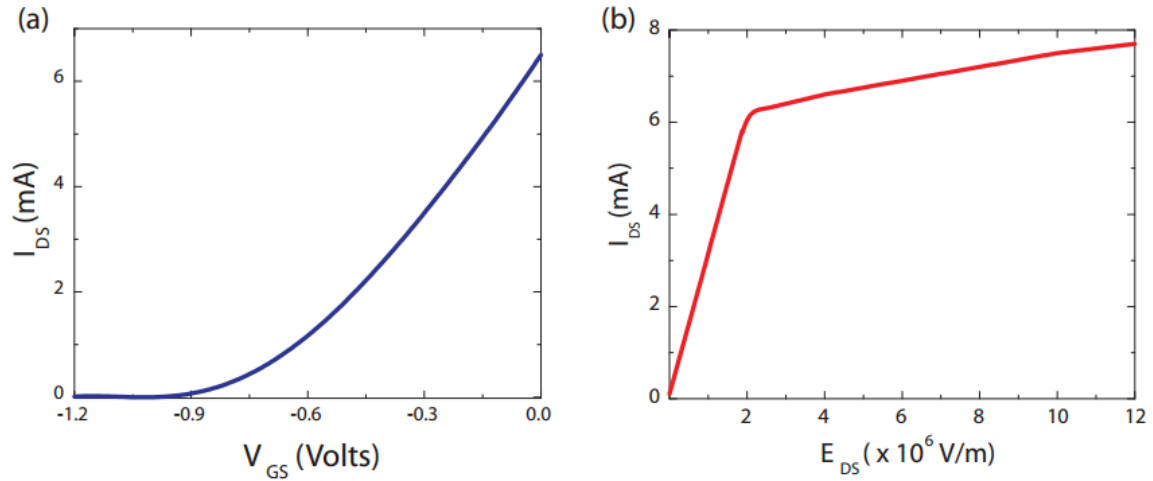


Figure 2.2 The simulated I-V characteristics of the HEMT. (a) Drain-to-source current (I_{DS}) as a function of gate-to-source (V_{GS}) voltage. (b) I_{DS} as a function of drain-to-source electric field (E_{DS}), operating in the linear region.

The same metal layer which is used to form each metamaterial is also used to connect each element together within the same row. These wires run perpendicular to the split gaps, and we polarize the electric field of incident radiation perpendicular to the connecting wires which avoids the Drude-like response documented in prior works [61]. At the perimeter of the device each row is connected vertically using the ohmic layer and all elements are connected to a single bond pad to provide DC bias voltage for the drain and source of the HEMT. The gates for all HEMTs are connected in a similar fashion to a single bond pad which provides the DC bias voltage for the gate.

The entire unit cell was modeled using a commercial finite difference time domain (FDTD) solver, CST's Microwave Studio, in which the metamaterial was designed to be resonant at 0.46 THz. The physical dimensions of the material layers in the device were modeled as shown in Fig. 2.1(c). The gold and ohmic layers were modeled as lossy metals based on their respective DC conductivity values. For both the n^+ and Schottky semiconductor layers, we utilize a frequency dependent Drude model for the conductivity. The 2DEG was simulated as a 2 nm thick Drude layer, which enables an accurate modeling of the HEMT device in both the conductive and the depleted (non-conducting) states. This is representative of what occurs in experiment by applying gate-to-source voltage (V_{GS}) of 0 V (conductive) and -1.1 V (depleted). This method allowed us to simulate the THz transmission of the device for various DC biases.

2.2. Results and discussion

2.2.1. THz Transmission with DC Biased HEMT

The device was characterized using a THz-TDS which has been previously described in detail [87]. The incident time-domain THz electric field ($\vec{E}_i(t)$) was polarized along the split gap to drive the metamaterial elements into resonance. At the resonant frequency of the metamaterial, (0.46 THz), the electric field is concentrated within the split gaps of the metamaterial and is within the linear regime of the device owing to the low incident power used in experiments. The reference signal was measured with the sample removed from the beam path in order to normalize the data and calculate the absolute transmission. In Fig. 2.3(a) we show the transmitted electric field as a function of frequency for different V_{GS} values. For V_{GS} less than -1.0 V, the channel is completely depleted, (see Fig. 2.2), and transmission shows a resonance at 0.46 THz. When the gate-to-source

voltage is increased above -1.0 V, the channel starts forming between the split gaps, and the metamaterial resonance begins to diminish. At $V_{GS} = 0$ V, when the channel is completely formed, a low-impedance path at the split gap is created which effectively shorts the metamaterial resonant response. It can be seen in the transmission data (Fig. 2.3(a)) that the frequency response shows no resonance at $V_{GS} = 0$ V.

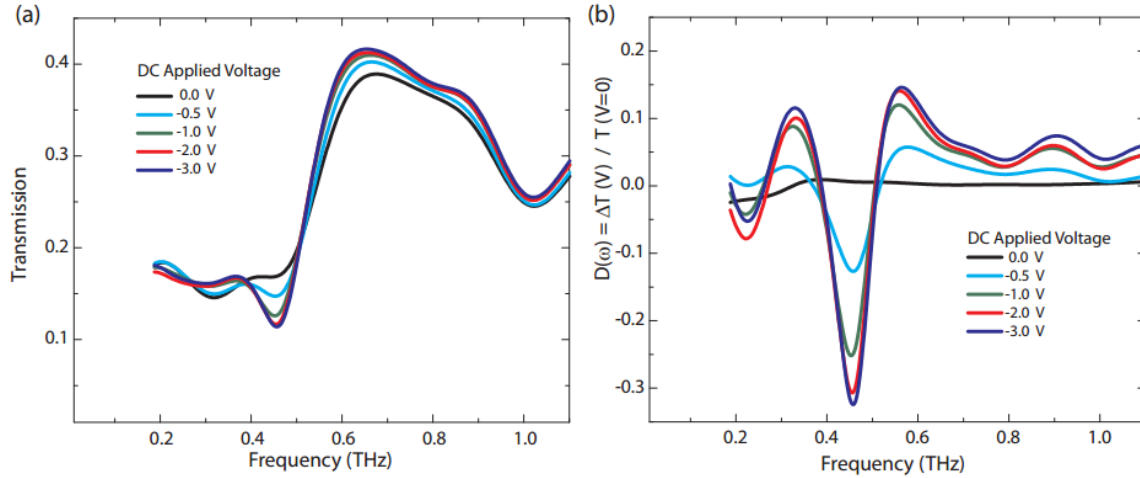


Figure 2.3 (a) Frequency dependent transmitted electric field for the HEMT / metamaterial device as a function of bias. (b) Voltage dependence of the differential transmission as defined in the text.

In order to elucidate the switching ability of the terahertz metamaterial, we plot the differential transmission, defined as $D(\omega) = [T(\omega)_{V_{GS}} - T(\omega)_{V_{GS}=0V}] / T(\omega)_{V_{GS}=0V}$ in Fig. 2.3(b). The black curve of Fig. 2.3(b) is two successive transmission measurements divided by each other, both at $V_{GS} = 0$ V, thus representing the frequency dependent noise. For a differential transmission of $V_{GS} = -0.5$ V, cyan curve of Fig. 2.3(b), $D(\omega)$ is relatively flat with deviations of about 5% or less, except at a frequency of 0.46 THz, where a value of -13% is observed. This minimum in differential transmission at 0.46 THz is seen to increase for increasing V_{GS} , until at $V_{GS} = -3.0$ V were a value of $D(\omega) = -33\%$ is observed.

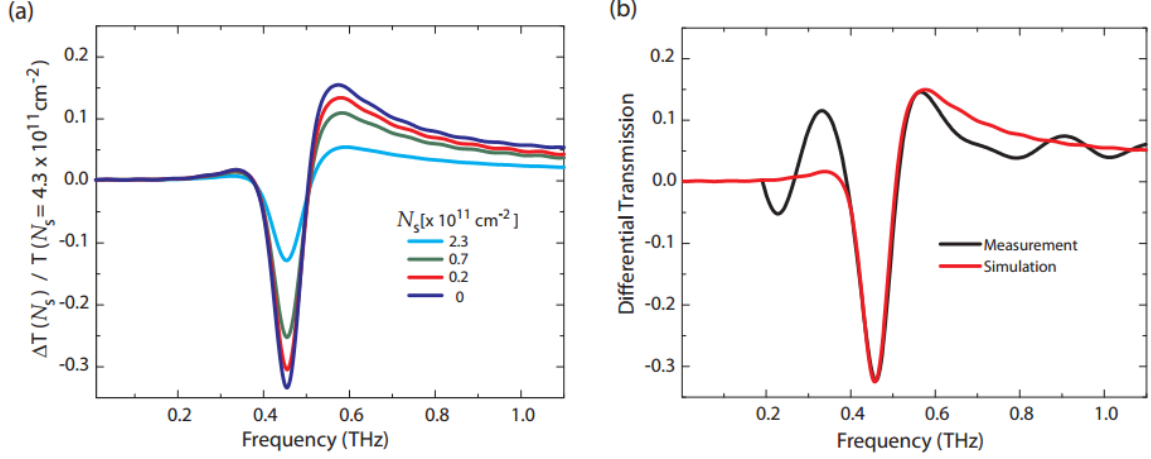


Figure 2.4 (a) Simulated differential transmission for various 2D carrier concentrations N_s . (b) A comparison of simulated (red) and experimental (black) differential transmission.

We computationally investigated the combined HEMT / metamaterial system. In recent years there has been considerable interest in 2DEG formation in HEMTs as a potential candidate for far-field THz wave interaction [78-82]. A majority of these applications revolve around utilizing the 2DEG instability in the HEMT channel. In our device the plasmon resonance resulting from the 2DEG instability does not play a roll. As such the parameter of interest for us is the frequency dependent conductivity $\sigma(\omega)$. The dynamic response of the channel carriers can in many cases be described by the two-dimensional Drude conductivity [88,89],

$$\sigma(\omega) = \frac{\sigma_0}{1 - i\omega\tau} \quad (2.1)$$

which has real and imaginary parts given by:

$$\sigma_r = \sigma_0 / (1 + \omega^2\tau^2), \quad \sigma_i = \sigma_0\omega\tau / (1 + \omega^2\tau^2) \quad (2.2)$$

where σ_0 is the DC conductivity [Siemens / sq] given by the expression $\sigma_0 = e^2 N_s \tau / m^*$.

Here e is the electron charge, N_s is the two-dimensional carrier density of the 2DEG, τ is

the scattering or relaxation time, m^* is the effective mass of electrons and ω the angular frequency of the time-varying electric field. It can be observed from Eq. 2.2 that for low frequencies, the conductivity is purely real and hence the current is in phase with the electric field in the split gap, for frequencies near the scattering time-constant both the real and imaginary part is half the DC conductivity and the phase is 45 degrees. For much higher frequencies the conductivity asymptotically approaches zero.

Modification of charge density in a true 2DEG has no implications on the capacitance of a metamaterial owing to its infinitesimal thickness. However, the nature of our FDTD is inherently three-dimensional. Thus, if we simply change the carrier density in simulation this would falsely modify the capacitance of the metamaterial. In order to approximate the two-dimensional charge density we restrict the real part of the permittivity to be equal to epsilon infinity ($12.9 \epsilon_0$ for GaAs) and allow the imaginary part to modeled by the Drude model. The resulting complex relative permittivity can be expressed analytically as,

$$\varepsilon(\omega) = \varepsilon_{\infty} + i\omega_p^2 \frac{\gamma\omega^{-1}}{\omega^2 + \gamma^2} \quad (2.3)$$

where γ is the collision frequency and ω_p is the plasma frequency. The collision frequency $\gamma = 2\pi \times 1.4$ THz is calculated with the relation $\gamma = e/m^*\mu$ where μ the mobility of the channel along with both e and m^* the electron charge and effective mass in GaAs. The plasma frequency is $\omega_p^2 = e^2 N_s / \epsilon_0 m^* d$ where N_s is the two-dimensional carrier concentration and d is the simulated model thickness of the channel layer. We sweep the carrier concentration in simulation observing a full resonant metamaterial response with a completely depleted channel ($N_s = 0 \text{ cm}^{-2}$) and a shorted response as the

carrier concentration increased to ($N_s = 4.3 \times 10^{11} \text{ cm}^{-2}$), see Fig. 2.4(a). Comparing this simulation with the experimental data shows excellent agreement (see Fig. 2.4(b)).

2.2.2. High frequency THz modulation

In section 2.2.1 we demonstrated the ability to switch the THz waveform by adjusting the gate bias voltage of the HEMT with respect to the drain and source (V_{GS}). We now turn toward demonstration of high speed dynamic modulation and utilize a THz-TDS with a Photoconductive Antenna (PCA) emitter and detector. The standard mechanical chopper often utilized in a TDS system was replaced with the HEMT / metamaterial modulator which serves the same function as the mechanical chopper with the important distinction that now only a narrow band of frequencies about the metamaterial resonance is modulated. Therefore, the data has to be interpreted differently than the static case. A square-wave bias, alternating between -1.1 V and 0 V, was applied to the gate of the HEMT with respect to the source and drain. The same square wave signal was applied to the reference input of the lock-in amplifier. After collecting the entire time-domain THz signal we have a sampled signal which can be expressed as,

$$V_{out}(t) = \alpha |\vec{E}_{t0}(t) - \vec{E}_{t1}(t)| \quad (2.4)$$

where $\vec{E}_{t0}(t)$ and $\vec{E}_{t1}(t)$ are the time-domain electric-field of the transmitted THz signal when $V_{GS} = 0 \text{ V}$ and $V_{GS} = -1.1 \text{ V}$ respectively, and α is a proportionality constant related to the particulars of the THz-TDS setup, such as the gain of pre-amplifier and averaging time-constant of the lock-in amplifier.

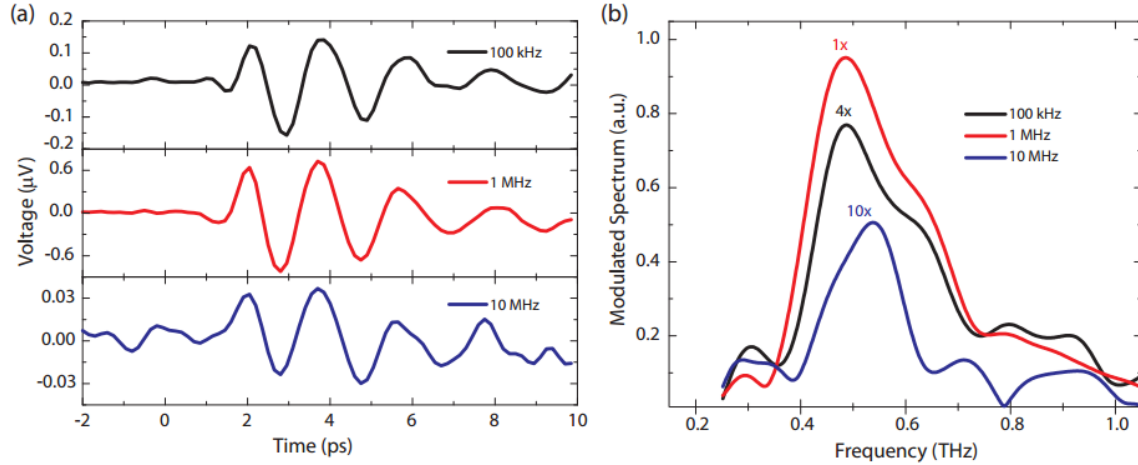


Figure 2.5 (a) Time domain data for modulation at frequencies of 100 kHz, 1 MHz and 10 MHz. (b) Spectra calculated from the time domain data.

The time-domain signal $V_{out}(t)$ is plotted in Fig. 2.5(a) for three different modulation frequencies, 100 kHz, 1 MHz and 10 MHz. In Fig. 2.5(b) we plot the spectrum as obtained from Fourier transforming the time-domain data plotted in Fig. 2.5(a). It can be seen that the peak of the spectrum lies at 0.46 THz indicating modulation of the metamaterial resonance. Bandwidth of the spectrum remains relatively unchanged between 100 kHz and 1 MHz, and the amplitude of the spectrum increases. At a modulation rate of 10 MHz the bandwidth is observed to decrease a bit and the amplitude falls off from values observed at 1 MHz. The spectrum amplitude has a non-monotonic dependence as a function of frequency that can largely be attributed to the THz-TDS setup itself. PCA detection has known limitations in THz-TDS at high frequency modulation as documented in past work [87]. Contributions to the degradation of the spectrum amplitude from the HEMT / metamaterial device should remain small as there is several orders of magnitude separation between the gate-to-source modulated voltage and the input noise voltage as reported in HEMT performance studies [90]. In both the time-domain signal and the spectrum, the modulation amplitude falls off at higher

frequencies and, for this device, the limit is in the neighborhood of 10 MHz. We attribute this as being primarily due to the parasitic nature of the long bond wires used in the chip assembly and, importantly, not a limitation of either the HEMT or metamaterial device.

In conclusion, we have demonstrated a HEMT / metamaterial device capable of modulation of THz radiation at frequencies up to 10 MHz, and modulation depths of up to 33% at 0.46 THz with all electronic control. A commercial GaAs process was utilized for implementation of the HEMT technology, as well as for fabrication of the metamaterials. We achieved monolithic integration of a total of 2×10^4 active transistors at the metamaterial unit cell level. This work demonstrates a new path for construction of high speed terahertz electronic devices.

CHAPTER 3

3. Liquid crystal tunable metamaterial absorber

Liquid crystals are viable candidates for tunable / dynamic metamaterials with much unexplored potential. The voltage dependent birefringence exhibited by nematic liquid crystals is well known and has been exploited over the past several decades leading to the development of devices, most notably optical display technology. However, the birefringence in LCs extends well beyond the visible spectrum and has afforded a new outlet for electronically tunable metamaterial and photonic structures [91-95]. Here we demonstrate that by combination of the variable properties of liquid crystals with metamaterials, an electronically tunable metamaterial absorber at terahertz (THz) frequencies is thus realizable [44].

3.1. Design and fabrication

Metamaterial absorbers typically consist of two metallic layers spaced apart by virtue of a dielectric spacer. The top metal layer is geometrically patterned in order to strongly couple to a uniform incident electric field. By pairing the top layer with a metal ground plane, a mechanism for coupling to the magnetic component of light is created - see Fig. 3.1(a). Altering the geometry of the metallic pattern and dielectric thickness enables tuning of the effective material response parameters allowing for both impedance matching and strong absorption at nearly any desired frequency. A schematic and optical microscope image of the device are shown in Figs. 3.1(a) and (b) with a single unit cell having the dimensions as labeled. ERRs were fabricated to form a square array with 50 μm lattice spacing. Each unit cell is connected to its neighbors via horizontal metallic

wires (4.5 μm width) and the entire array is connected to bias pads lying at the perimeter of the device. A 200 nm Au/Ti continuous metal ground plane was E-beam deposited on top of a supporting silicon (Si) substrate. A 5.5 μm thick liquid polyimide (PI-5878G, HD MicrosystemsTM) dielectric layer was spin coated on top. Ultraviolet (UV) photolithography is used to pattern photoresist which was used for final deposition of 200 nm Au/Ti to create the ERR layer. We also use the ERR structures to serve as a hard mask for inductively coupled plasma and reactive ion etching in order to remove all polyimide not directly underneath the metamaterial layer.

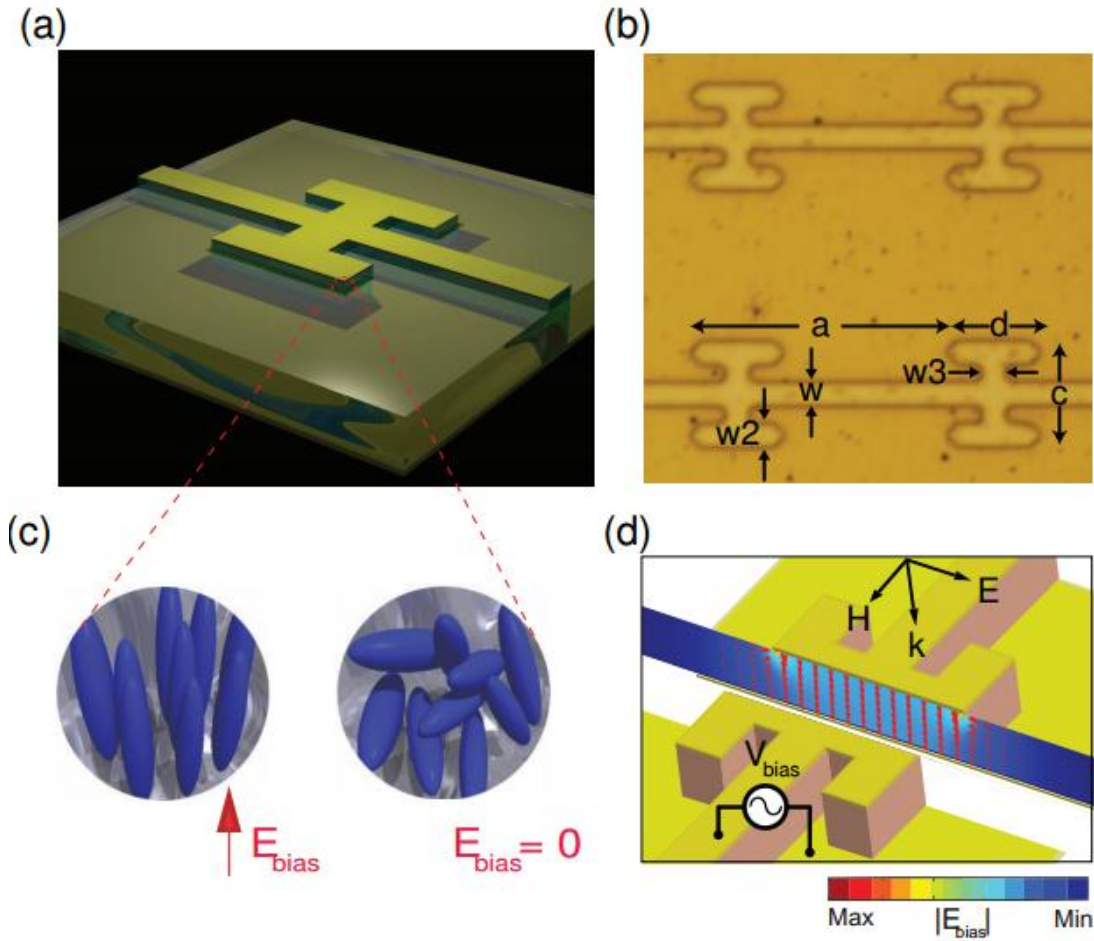


Figure 3.1 Design and operational principle of the tunable metamaterial absorber. (a) Rendering of a single unit cell of the liquid crystal metamaterial absorber. (b) Optical microscope image of a portion of the metamaterial array where the unit cell has the

dimensions of $a = 50$, $c = 20$, $d = 16$, $w = w_2 = 4.5$, and $w_3 = 5$ in micrometers. (c) Depiction of the random alignment of liquid crystal in the unbiased case (right) and for an applied AC bias (left). (d) Simulation of the electric field vector and absolute value produced from an applied potential bias between the ERR and ground plane.

The liquid crystal 4'-n-pentyl-4-cyanobiphenyl (5CB) is deposited on top of the metamaterial array and completely fills in and encapsulates the polyimide / metal structure. 5CB possesses a nematic LC phase at room temperature with large birefringence ($n_e - n_o = \Delta n$) at THz frequencies ranging between 0.11 to 0.21 [84,96-98], where the refractive index can be switched between its ordinary n_o and extraordinary n_e value in the presence of an electric field. A schematic shown in Fig. 3.1(a,c) illustrates the mechanism by which the LC is tuned. A potential is applied between the ERR and ground plane which orients the LC along field lines (see Fig. 3.1(d)). The polyimide is required for structural support however it plays a significantly more important role in our design. Most liquid crystals have large interactions with boundaries which inhibits any possible response to an applied electric field thus causing threshold phenomena -- an effect called the Freedericksz transition [99]. Notably, our configuration permits LC near the surface of the polyimide to be *orientated with electric field lines*. This also facilitates a smooth tuning of the refractive index as a function of applied electric field.

3.2. Results and discussion

The frequency dependent reflectance [$R(\omega)$] was characterized at an incident angle of 20 degrees from 2.0 to 3.5 THz using a Fourier-transform infrared spectrometer, liquid helium-cooled Si bolometer detector, and a germanium coated 6 μm mylar beamsplitter. The measured reflectance spectra are normalized with respect to a gold mirror and we calculate the frequency dependent absorption as $A(\omega) = 1 - R(\omega)$ since the transmitted intensity was zero due to the metal ground plane. The resulting $A(\omega)$ was characterized

and measurements were performed with the THz electric field perpendicular to the metal connecting wires, as depicted in Fig. 3.1(d).

The LC molecules are aligned by applying a square-wave potential between the ERR metal layer and the ground plane at various modulation frequencies (f_{mod}). The square-wave is centered about zero and has peak-to-peak voltage equal to twice the peak bias voltage (V_{bias}). Use of a modulated bias prevents free carrier build-up at the electrode metal interface which can occur for DC applied potentials [100,101].

The absorption was characterized for a number of different bias values and modulation frequencies. In Fig. 3.2(a) we show the frequency location of the absorption maximum ($A(\omega)$) as a function of V_{bias} for modulation frequencies of 373 Hz, 1 kHz, 10 kHz, and 100 kHz. The general trend is that as we increase the applied voltage the metamaterial absorption shifts to lower frequencies. For $f_{mod} = 373$ Hz and 1 kHz the change is monotonic for increasing potential, but we find deviations from this for 10 kHz and 100 kHz. As can be observed in Fig. 3.2(a) the greatest frequency shift occurs for $f_{mod} = 1$ kHz - in accord with prior investigations with 5CB [84,91,98]. In Fig. 3.2(b) we plot the frequency dependent absorption $A(\omega)$ for 0 V (blue solid curve) and 4 V (red dashed curve) at $f_{mod} = 1$ kHz. With no applied bias we achieve a reasonable absorption of 85% at 2.62 THz, a full width half max (FWHM) of 600 GHz and the spectrum is otherwise featureless. At $V_{bias} = 4$ V the resonant absorptive feature shifts to 2.5 THz, lowers to a peak value of 80% and narrows slightly with a FWHM of 420 GHz. This represents a shift in the peak of the absorption by 4.6% in frequency.

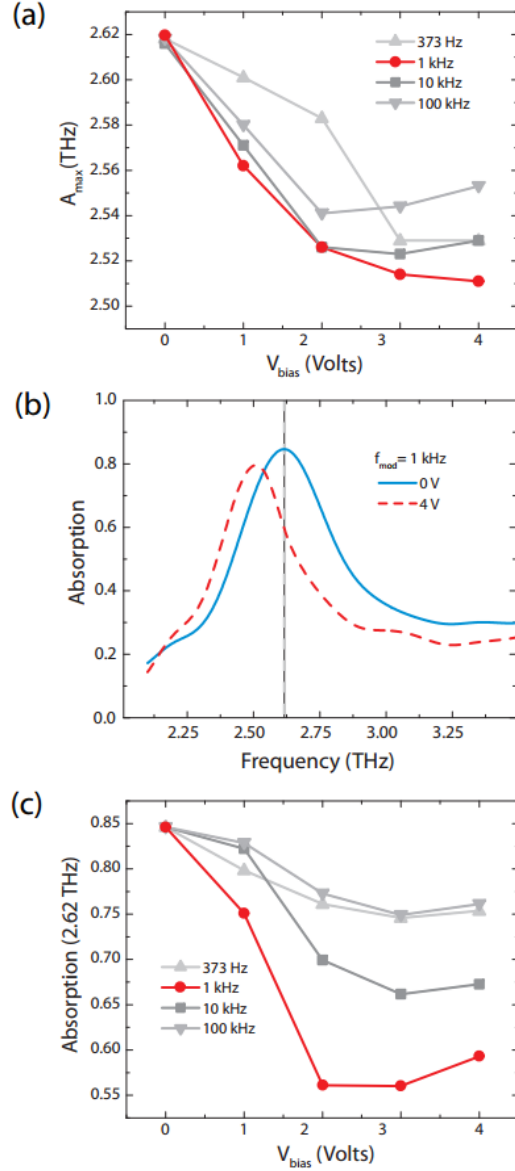


Figure 3.2 Experimentally measured absorption of the metamaterial absorber. (a) Frequency location of the absorption maximum ($A(\omega)$) as a function of applied bias voltage (V_{bias}) for modulation frequency (f_{mod}) values of 373 Hz, 1 kHz, 10 kHz, and 100 kHz. (b) Frequency dependent absorption $A(\omega)$ for 0 V (blue solid curve) and 4 V (red dashed curve) at $f_{mod} = 1$ kHz, dashed line is centered at $A_{maz}(V_{bias} = 0) = 2.62$ THz. (c) The absorption value at 2.62 THz as a function of V_{bias} for various modulation frequencies.

In many applications one may desire amplitude modulation only over a narrow band. As an example we consider operating at a fixed frequency of $\omega_0 = 2.62$ THz, i.e. the peak absorption of the unbiased case plotted in Fig. 3.2(b). In Fig. 3.2(c) we plot

$A(\omega_0)$ as a function of V_{bias} for various modulation frequencies. Generally we observe that the absorption level drops as a function of increasing voltage bias for all modulation frequencies investigated, which seems to saturate near 3-4 volts of applied bias. The greatest change in $A(\omega_0)$ occurs for 1 kHz bias modulation, as shown by the red curve in Fig. 3.2(c) -- in accord with the results presented in Fig. 3.2(a). The LC 5CB thus provides an all-electronic means of both frequency and amplitude tuning of the absorption peak of metamaterial absorbers and here we realize an amplitude tuning of over 30% at $\omega = 2.62$ THz.

In order to clarify the mechanism underlying operation of the tunable absorber, we perform full wave 3D electromagnetic simulations. The Au/Ti metal layers were modeled as a lossy metal with a frequency independent conductivity of $\sigma_0 = 4.56 \times 10^7$ S/m, and the polyimide layer with a relative permittivity of $\tilde{\epsilon}_{poly} = \epsilon_1 + i\epsilon_2 = 2.88 + i0.09$ [52]. In accord with prior work [84,96-98], we model the complex refractive index of 5CB, (with zero applied bias), as a lossy dielectric with $\tilde{n}_{5CB} = n_{5CB} + i\kappa_{5CB} = 1.82 + i0.14$. As mentioned in the main text, the LC encapsulates the metamaterial array and thus we model a 2 μm thick layer on top of the ERR. We assume that any LC not lying in-between the ERR and ground plane is unaltered by the applied bias (see 3.1(d)). The THz birefringent properties of 5CB have been characterized as an increase in the real part of the refractive index (n_{5CB}), (for increasing applied bias), between the ordinary and extraordinary states [84,97]. However, it has been demonstrated that there is little difference in the imaginary component (κ_{5CB}) above 1.2 THz [96]. In simulation, we thus modify only n_{5CB} as a function of V_{bias} and keep the imaginary refractive index constant at a value of $\kappa_{5CB} = 0.14$.

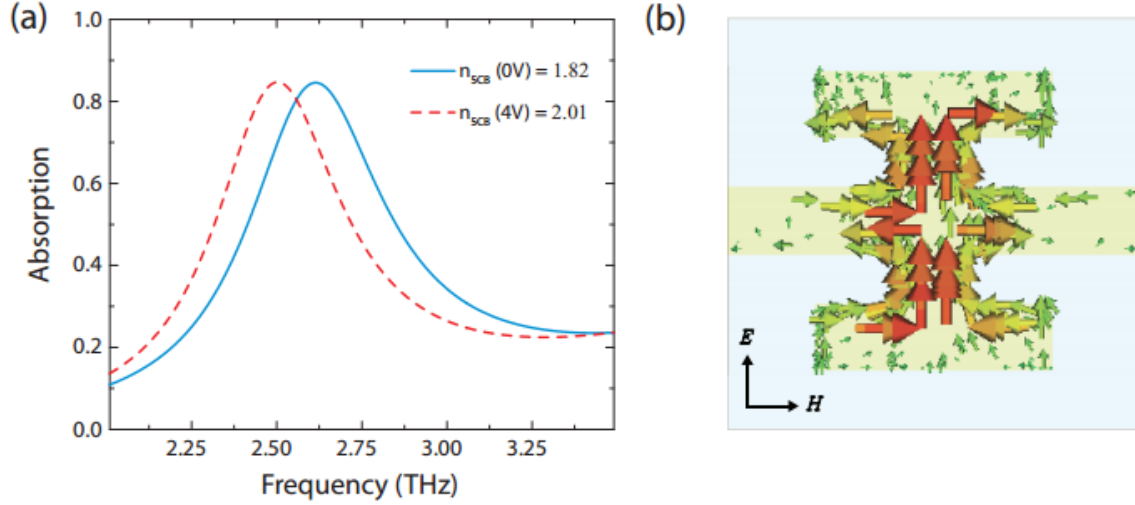


Figure 3.3 Numerical simulations of the metamaterial absorber. (a) THz absorption simulated for 0 V (blue solid curve) and 4 V (red dashed curve) at $f_{mod} = 1\text{kHz}$. (b) Simulated current density in the ERR for the case of the unbiased absorption maximum $A_{maz}(V_{bias} = 0) = 2.62\text{ THz}$.

Results from the computational investigation are presented in Fig. 3.3. Starting initially from the unbiased state where $n_{5CB}(V_{bias} = 0) = 1.82$, we monotonically increase n_{5CB} resulting in a redshift of the absorption peak frequency (see Fig. 3.3(a)). At 4 V the peak absorption occurs at 2.51 THz and in the numerical model we determine $n_{5CB}(V_{bias} = 4) = 2.01$. As can be observed we find good agreement with experimental results (see Fig. 3.2), although simulation indicates that the value of the peak absorption at 4 V applied bias is not significantly altered from the unbiased state. Notably we find that the change in refractive index determined by simulation is $\Delta n = 0.19$ -- consistent with values determined by other works [84,96-98]. At a frequency of 2.62 THz, simulation predicts a change in A of 15% between zero and 4 V of applied bias, as shown in Fig. 3.3(a). In contrast experimental results yield a 30 percent change in absorption at the same frequency.

It is instructive to examine the particular mode exhibited by our device at the maximum of the absorption, i.e. 2.62 THz. This can be explored by observation of the the surface current density and magnitude of the THz electric field (plotted in a plane centered between the two metallizations), as shown in Figs. 3.3(b) and 3.4(a). We find that the surface current density is similar to that found in prior investigations [23] and, as expected, the THz electric field is primarily localized underneath the ERR - in the same vicinity as the electric field provided by the bias shown in Figure 1c. In contrast, the power loss density shown in Fig. 3.4(b), reaches its strongest values just outside the ERR at the polyimide / LC interface. (The magnitude of the electric field is also plotted as a vector field in Fig. 3.4(c), and the power loss density in Fig. 3.4(d); both in cross section.) The form of the metamaterial absorptive feature strongly depends on the value of the complex dielectric constant that the local terahertz electric field experiences. In particular the resonant frequency is set by the real part of the dielectric function, whereas the width of the absorption is determined by dielectric loss [38,42]. Thus future designs can achieve greater frequency tuning of the absorption peak by altering the geometry such that the LC lies directly underneath the ERR, where the applied bias is greatest, as shown in Fig. 3.1(d). An alternative approach would be utilization of LC polymers [102], which could then act both as a supporting structure, and bias tunable dielectric.

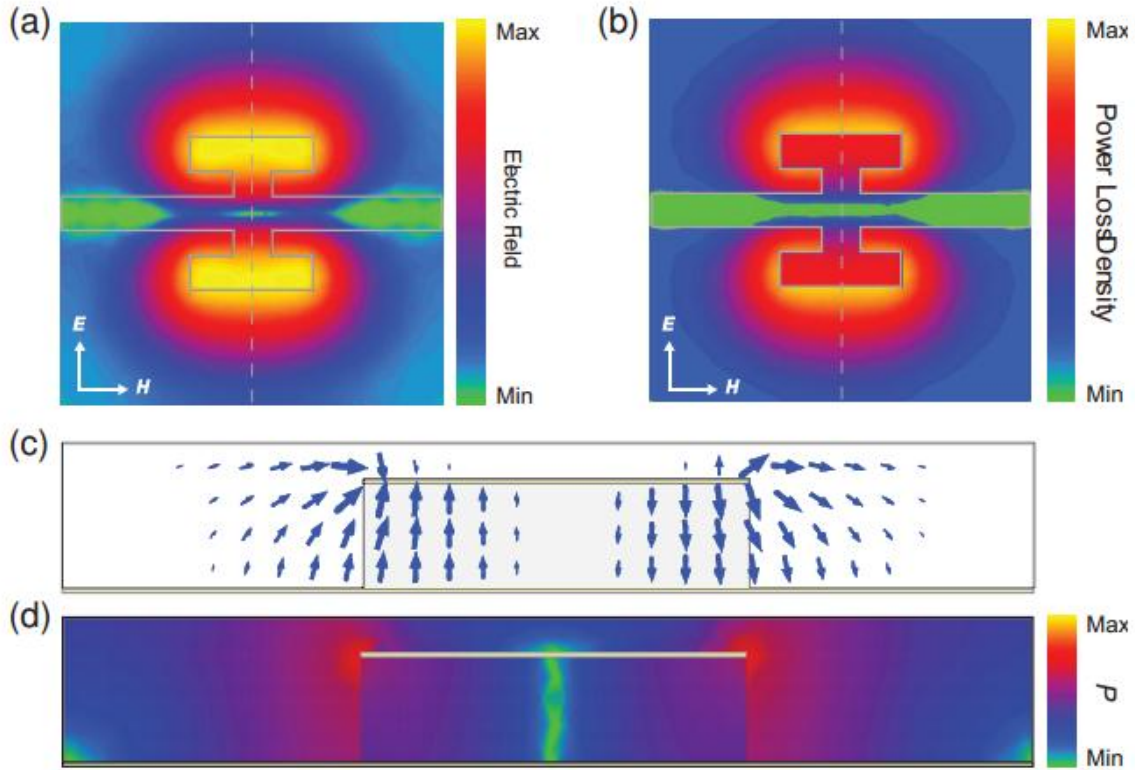


Figure 3.4 Resonant terahertz fields of the metamaterial absorber. (a) Simulated electric field magnitude and (b) power loss density (P) shown at a plane centered between the two metallizations. (c,d) Terahertz electric field vector plot (c) and power loss density (d) shown for a cross sectional cut (gray dashed line in (a,b)).

We note that in order to frequency tune a metamaterial in which both the electric and magnetic properties have been designed, it is desirable to adjust them identically to preserve the electromagnetic response. Some dynamic magneto-dielectric metamaterials may require sophisticated tuning mechanisms in order to maintain their properties [103]. In contrast, a salient feature of this particular absorber design, is the ability to simultaneously adjust $\epsilon(\omega)$ and $\mu(\omega)$ by simply altering the dielectric properties of the dielectric spacing layer, as demonstrated here with liquid crystal. This can be verified by plotting the extracted [38] material parameters. The extracted material parameters (assuming a thickness of $7.7 \mu\text{m}$ equal to its physical dimensions) for the metamaterial absorber is obtained from simulations utilizing a frequency dependent Drude model

(plasma frequency $\omega_p = 2\pi \times 2175$ THz and collision frequency $\omega_c = 2\pi \times 6.5$ THz). As revealed in Fig. 3.5, both the permittivity and permeability shift with little change in their shape for all applied biases investigated.

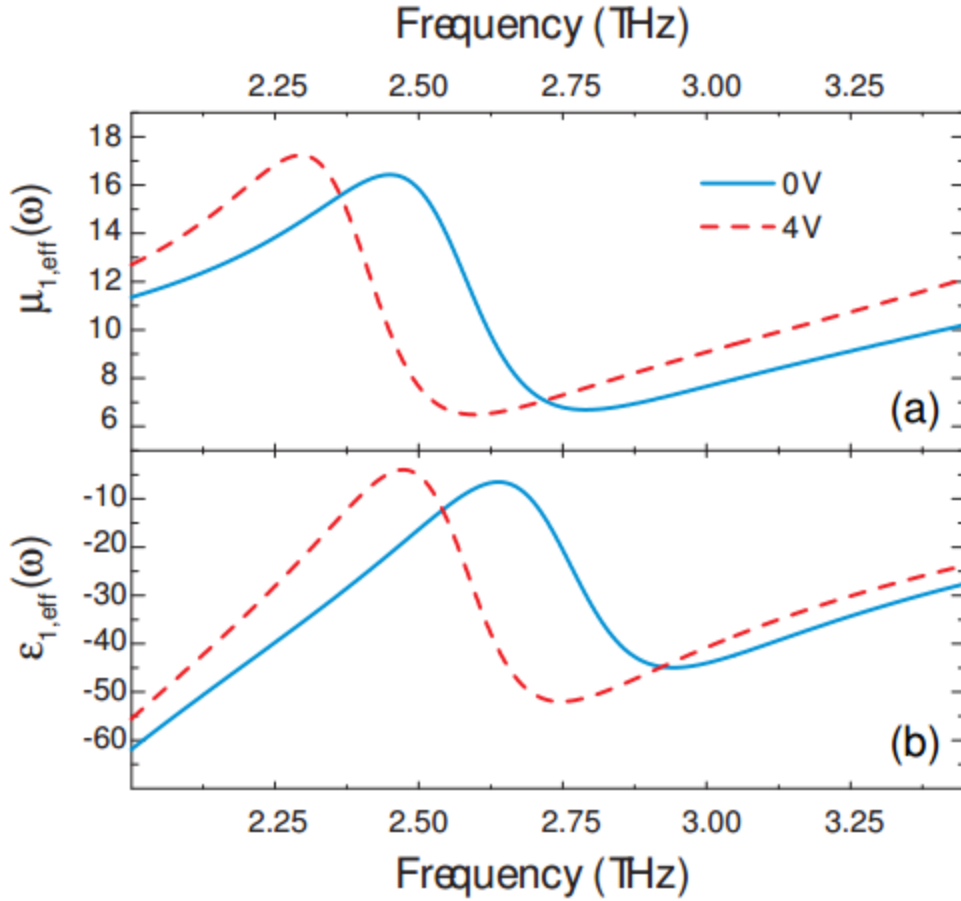


Figure 3.5 Effective optical constants of metamaterial absorber. (a) Real part of effective permeability ($\mu_{1,eff}$), and (b) real part of effective permittivity ($\epsilon_{1,eff}$), determined from inversion of the simulated scattering parameters for 0 V (blue solid curves) and 4 V (red dashed curves).

The demonstration of the dynamic control of electromagnetic waves at surfaces presented here provides a new path forward construction of exotic devices. The formation of pixelated arrays of metamaterial LCs would provide a means for SLM (including phase and amplitude), and focal plane array imagers. As both metamaterials and liquid

crystals have been shown to operate across much of the electromagnetic spectrum this would enable an innovative substitute for digital micro-mirror devices (DMDs), which are spectrally featureless and have set frequency limits. The fabrication of focal plane arrays consisting of the designs demonstrated here could serve as an excellent candidate for detector pixels when implemented into bolometric, rectification, pyroelectric and piezoelectric configurations.

In conclusion, we have demonstrated all-electronic control of liquid crystal metamaterial absorbers. We achieve a 30 percent amplitude tuning of the absorption and realize a frequency tunability greater than 4 percent. The scalability of both liquid crystal properties and metamaterial absorbers suggests our design can be extended to both higher and lower frequencies. The prospect of electronically controlled metamaterial absorbers have implications in numerous scientific and technological areas rich in applications, particularly in sensing, imaging, energy harvesting and dynamic scene projectors.

CHAPTER 4

4. Metamaterial absorber terahertz spatial light modulator

Here we demonstrate, for the first time, a doped semiconducting metamaterial SLM with multi-color super-pixels composed of arrays of electronically controlled THz metamaterial absorbers [45]. In Fig. 4.1(a) we show a photograph of an 8x8 pixel implementation of the THz MMA-SLM. The pixels are tiled in a similar fashion to conventional RGB color schemes (Bayer filters) and we modulate each at a unique frequency in the THz range. The overall SLM system architecture is shown schematically in Fig. 1b and consists of metamaterial absorber pixels flip chip bonded to a Silicon chip carrier with routing to bond pads which are wire-bonded to a leadless chip carrier (LCC). Individual pixels are biased through a commercial 64 channel output controller and each THz color pixel consists of approximately 400 individual metamaterial absorber unit cells.

4.1. Design and fabrication

Our metamaterial absorber consists of two metallic layers with a dielectric spacer lying in-between. The top metal layer is patterned in order to strongly couple to the electric component of an incident electromagnetic wave. A bottom ground plane layer is spaced relatively close to the top layer, thus allowing the external magnetic field to couple – as shown in Fig. 1b. Altering the geometry of the metallic pattern and dielectric thickness allows tuning of the impedance and loss, thus enabling resonant absorption at nearly any frequency. In our implementation we utilize a 2 μm ($< \lambda/35$) thick n-doped ($2.0 \times 10^{16} \text{ cm}^{-3}$) epitaxial layer of GaAs as the dielectric spacer. A junction is formed from the ELCs

and serves as the Schottky contact with the bottom ground plane used as the ohmic contact. This configuration enables depletion of carriers in the epi-layer underneath the ELCs as a function of applied reverse bias and results in tuning of the absorption peak and modulation of the electromagnetic spectrum.

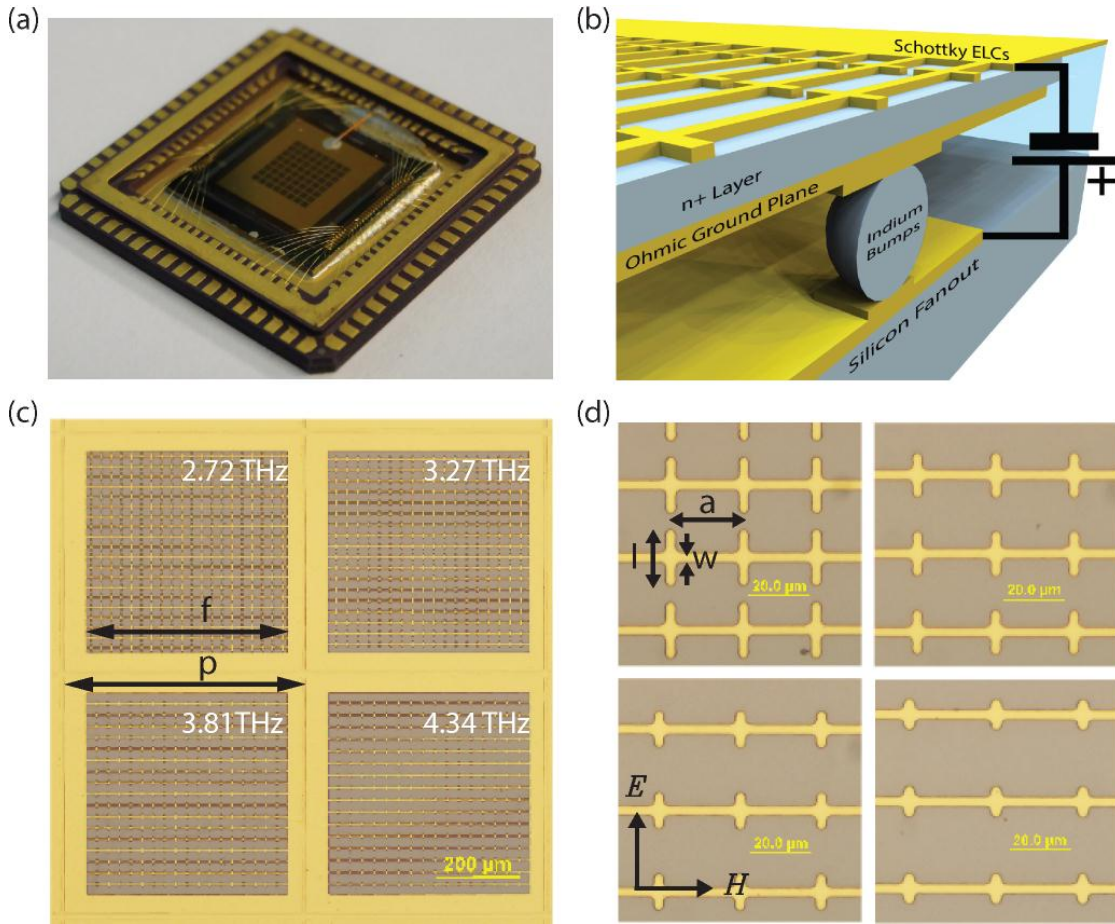


Figure 4.1 Design and structure detail of the electronically controlled THz metamaterial absorber based spatial light modulator (MMA-SLM). (a), Image of MMA-SLM as assembled in chip carrier package. (b), Cross-sectional schematic view of a single pixel. (c,d), Optical microscope images for each color pixel with dimensions as listed in Table 4.1.

Optical microscope images of the THz MMA-SLM are shown in Figs. 4.1(c,d) and the dimensions of each color pixel is listed in Table 4.1. Each pixel has a separate ground plane which provides electric isolation to enable independent modulation, and

necessitates fabrication of mesas extending through the epi-layer to define a single pixel. The metamaterial unit cells are connected to their neighbors via horizontal metallic wires. The arrays have a pitch, p , of 600 μm and the isolated ohmic contact ground planes are centered about each pixel with a side length of 570 μm . The mesas lie in-between the ground planes and have a width of 10 μm .

Table 4.1 Dimensions for each frequency (THz) color pixel as relating to Fig. 4.1(c,d). The line width w is 3 μm and the pixel pitch p is 600 μm are held constant for each pixel design.

dimension [microns]	2.72 THz	3.27 THz	3.81 THz	4.34 THz
a	25	27	28	30
l	19.2	15.2	12.5	10.6
f	500	486	476	480

Fabrication of the THz 8 x 8 array is similar to the fabrication of an infrared FPA with an additional step to define the metamaterial pattern on the backside^[104]. These THz pixels are hybridized to a control chip to dynamically bias each pixel in the array.

Fabrication begins by defining the metamaterial pixels on a GaAs substrate as shown in Fig. 4.2. The GaAs substrate consists of a 2 micron layer of doped GaAs with a highly selective etch stop layer below. A typical etch stop layer consists of 50nm of AlGaAs.

The mesa is etched down to the etch stop layer to ensure electrical isolation between pixels. Next, ohmic contact metal consisting of Ge(280 Å)/Au(540 Å)/Ni(200 Å)/Au(3,000 Å) is deposited onto each pixel and a rapid thermal anneal (RTA) at 370 degrees Celsius is performed. The ohmic contact metal is a large square with side length of 570 μm . A 200nm thick layer of silicon dioxide is deposited with a window to the ohmic contact metal. An under bump metal (UBM) layer of Ti(300 Å)/Ni(1,500

$\text{\AA}/\text{Au}(500 \text{ \AA})$ is deposited to cap the silicon dioxide holes. The UBM layer is used to prevent indium (used for chip hybridization) from diffusing into the ohmic contact metal and degrading its electromagnetic properties.

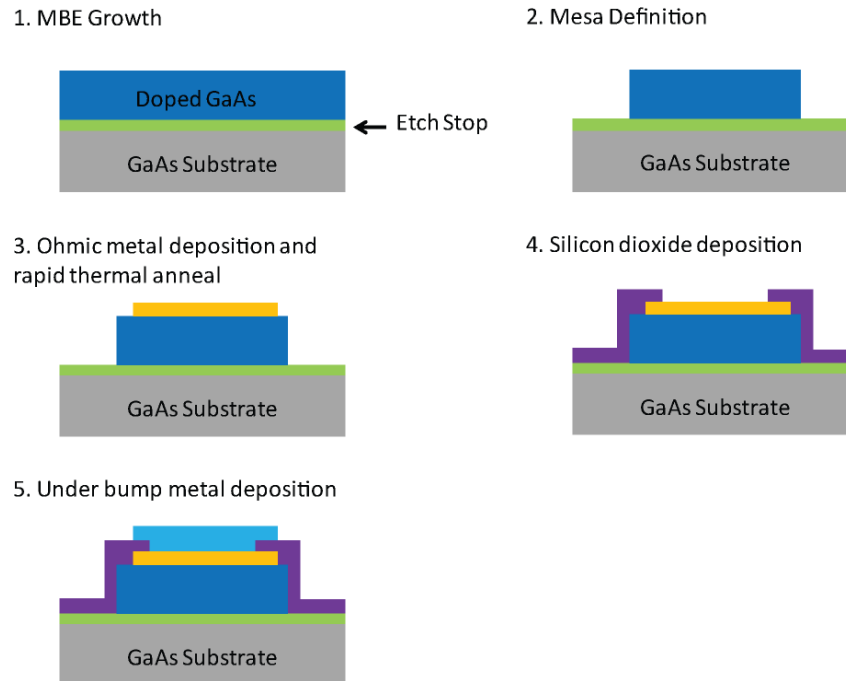


Figure 4.2 Schematic representation of the fabrication procedure of the epitaxial n-doped GaAs layer pixel definition.

A control chip was fabricated, as illustrated in Fig. 4.3, in parallel to the fabrication of the GaAs pixel array. The fabrication of the control chip started with a silicon wafer with a 1 micron thick layer of silicon dioxide. The metal control lines are defined onto the silicon wafer with $\text{Ti}(500 \text{ \AA})/\text{Au}(3000 \text{ \AA})$ metal, which will be used to make electrical contact to the metamaterial pixels and a wire bond pad on the silicon wafer. A 200nm layer of silicon dioxide is deposited with windows to the bond pads and in areas that will make contact to the metamaterial pixels. A UBM metal consisting of $\text{Ti}(300 \text{ \AA})/\text{Ni}(1,500 \text{ \AA})/\text{Au}(500 \text{ \AA})$ is deposited to cap the windows made in the silicon dioxide. The Ti layer serves as an adhesion layer, the Ni as an indium diffusion barrier,

and the Au as an indium sticking layer. A large indium pad is deposited onto the UBM metal and reflowed to form a sphere that will be used to make electrical contact to the pixel array.

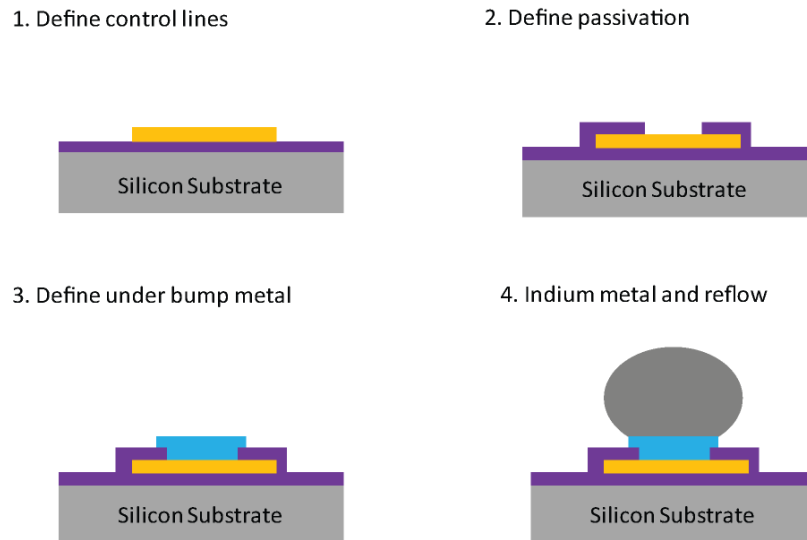


Figure 4.3 Schematic representation of the fabrication procedure of the control chip.

As depicted in Fig. 4.4, once the two chips have been fabricated, they are bonded together with a flip-chip bonder (FC150: SUSS MicroTec) at 160 °C. To provide mechanical support to the pixel array and the control chip, an underfill epoxy was injected between the two chips with the aid of the capillary force to feed the epoxy. The substrate is then selectively removed up to the etch stop layer. The etch stop layer is also selectively removed and the backside is patterned with Ti(150 Å)/Au(1350 Å) to form a Schottky metal .

1. Flip chip bond and epoxy

2. Substrate removal and Schottky metal deposition

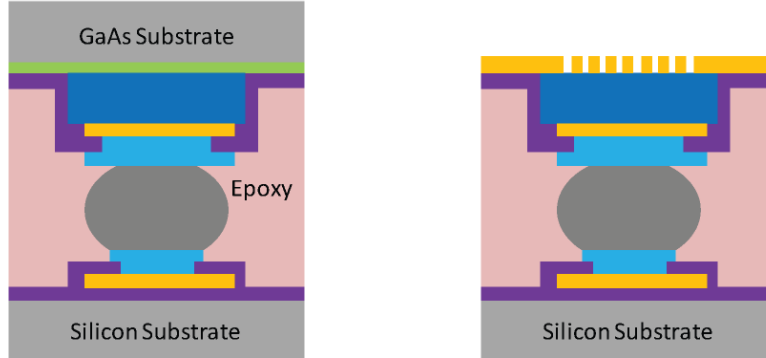


Figure 4.4 Schematic representation of the fabrication procedure for final device assembly.

We characterized the electrical performance of the MMA-SLM by running voltage dependent current (IV) profiles for all 62 functioning pixels. The resulting mean and standard deviation are shown in Fig. 4.5(a) and is comparable to previous investigations. The breakdown voltage occurs just beyond the maximum bias swept with the knee of the IV curve occurring close to $V_{\text{bias}} = -23$ V. The entire device is simultaneously biased with the resulting IV profile over the full bias range, including forward bias, as shown in Fig. 4.5(b).

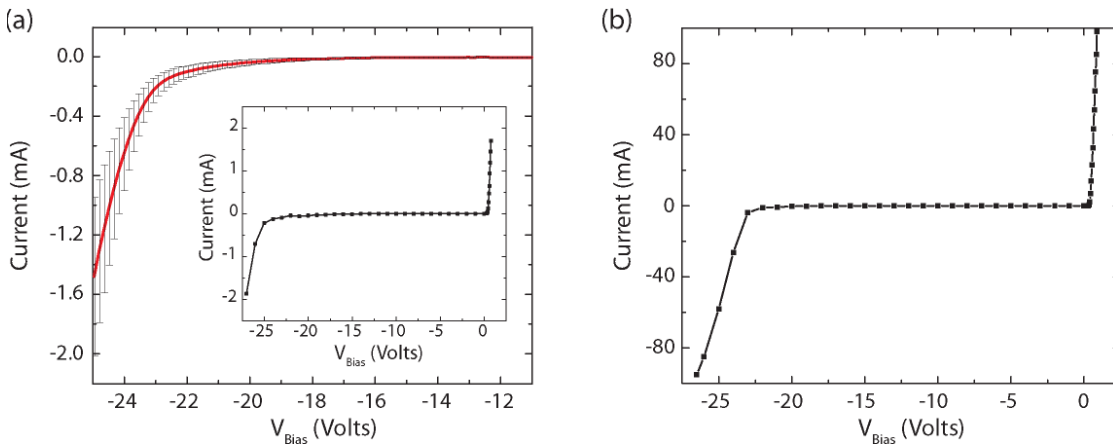


Figure 4.5 Voltage dependent current (IV) profile. (a), Average IV curve measured with the standard deviation plotted as the error bars for the 62 functioning pixels. The inset plot shows a single pixel's IV curve including forward bias. (b), The measured IV for the entire device.

4.2. Results and discussion

In Fig. 4.6(a-d) we show the measured frequency dependent reflectance $R(\omega)$ for zero applied bias and for a reverse bias of $V_{\text{bias}} = -26.5$ V. The reflectance was characterized at an incident angle of 20 degrees from 2 to 10 THz using a Hyperion-2000 infrared microscope connected to a Fourier-transform infrared spectrometer, Hg-arc lamp source, liquid helium-cooled Si bolometer detector, and a germanium coated 6 μm mylar beamsplitter. The measured reflectance spectra are normalized with respect to a gold mirror with square metal apertures set to 450 μm on each side. Measurements were performed with the THz electric field perpendicular to the metal connecting wires, as depicted in Fig. 1d. The DC potential between the Schottky metal layer and the Ohmic ground plane is a reverse bias voltage (V_{bias}) as shown in Fig. 4.1(b).

When a metamaterial pixel is unbiased, the GaAs epi-layer has a maximum carrier concentration (n_{GaAs}). As V_{bias} is increased, depletion of n_{GaAs} results in a monotonic redshift of the reflectance minimum until saturation, as shown for each color pixel in Fig. 4.6(e). A maximum $V_{\text{bias}} = -26.5$ V results in sufficient depletion of n_{GaAs} to shift the frequency of the reflectance minimum by nearly 5%; in the case of the lowest color frequency pixel. As the reflectance redshifts the minimum value decreases between the two bias conditions, with the largest decrease occurring at lower frequencies where minimum value decreases by 12%.

In many applications, amplitude modulation over a narrow band is desired. As an example we consider operating at a fixed frequency ω_0 i.e. the reflectance minimum of the unbiased case. In Fig. 4.6(f) we plot $R(\omega_0)$ as a function of V_{bias} each color pixel. We observe that the reflectance level increases as a function of increasing V_{bias} which appears

to saturate upon approaching the breakdown threshold. The doped semiconductor layer thus provides an all-electronic means of both frequency and amplitude tuning of the metamaterial reflectance and here we realize amplitude tuning of over 30% at 2.52 THz.

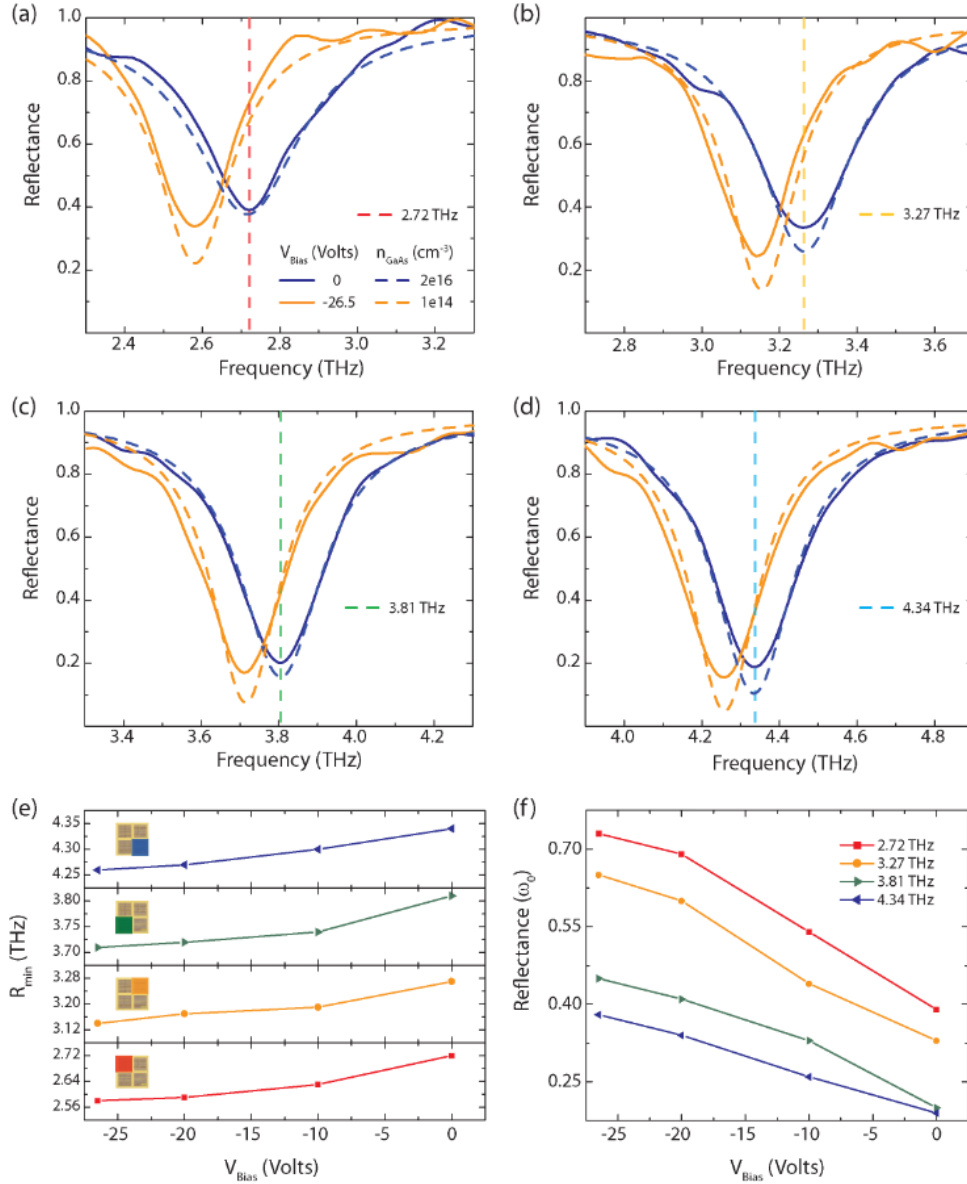


Figure 4.6 Experimentally measured and computationally simulated frequency dependent reflectance of the metamaterial absorber shown for each color sub-pixel. (a-d), The experimental curves are shown for applied bias voltage V_{bias} equal to both 0 V (blue) and -26.5 V (gold), with the simulated curves shown for carrier concentration of the n-doped GaAs epitaxial layer n_{GaAs} equal to 2.0×10^{16} cm $^{-3}$ (blue dashed) and 1.0×10^{14} cm $^{-3}$ (gold dashed). The colored vertical dashed lines indicate frequency of the unbiased reflectance minimum, $R_{\text{min}} (V_{\text{bias}} = 0) = \omega_0$, for their respective sub-pixels. (e), Frequency location of R_{min} as a function of V_{bias} for each color sub-pixel, color shading

on inset image indicates location within the super-pixel. (f), The reflectance values $R(\omega_0)$ for ω_0 as indicated by the vertically dashed color lines in Fig. 4.6 (a-d), shown as a function of V_{bias} for each color sub-pixel.

In order to clarify the mechanism underlying operation of the tunable absorber, we perform full wave 3D electromagnetic simulations. Recent computational studies have looked at the relation between the semiconductor physics and electromagnetic response of metamaterials^[105]. We model each color pixel using commercial FDTD solver, CST's Microwave Studio. We define both the ELC and ground plane metal layers as a lossy metal with DC conductivity value $\sigma_0 = 4.5 \times 10^7$ S/m. For the n-doped GaAs epi-layer, whose frequency dependent permittivity $\tilde{\epsilon}_{GaAs}(\omega)$ is modeled by Drude theory shown in Eq. 4.1^[106,107], we define three separate volume regions: the unbiased depletion, the maximum bias depletion, and the non-depleted region as depicted in Fig. 4.7(c,d).

The dielectric permittivity of GaAs has been shown to be well described within the framework of the Drude model for the conductivity at THz frequencies. The model can be written as the following:

$$\tilde{\epsilon}_{GaAs}(\omega) = \epsilon_{\infty} + \frac{\omega_p^2}{\omega(\omega - i\gamma_c)} \quad (4.1)$$

Where $\epsilon_{\infty} \approx 12.9\epsilon_0$ is the dielectric constant of undoped GaAs and $\epsilon_0 = 8.85 \times 10^{-12}$ F/m is the vacuum permittivity, ω_p is the plasma frequency, and γ_c is the collision frequency. ω_p is dependent of the free carrier concentration n_{GaAs} :

$$\omega_p^2 = \frac{n_{GaAs} q^2}{\epsilon_0 m^*} \quad (4.2)$$

Where $q = 1.6 \times 10^{-19}$ C is the elementary charge, and $m^* = 0.067m_0$ is the effective mass of n-doped GaAs and $m_0 = 9.11 \times 10^{-31}$ kg is the ordinary mass of an electron. γ_c is dependent on the carrier mobility μ :

$$\gamma_c = \frac{q}{m^* \mu} \quad (4.3)$$

Studies show that μ is strongly dependent on the doping level n_{GaAs} with μ values up to 6500 cm²/Vs reported at $n_{GaAs} = 2 \times 10^{16}$ cm⁻³^[107], though values closer to 4000 cm²/Vs have also been measured^[106], and is closer to what is commercially available. In the computational model we use μ as a fit parameter and determine a value of 3800 cm²/Vs which is fixed for the model of all four unit cell types.

The depletion width x_n in an n-GaAs based Schottky diode can be calculated from^[108,109]:

$$x_n = \sqrt{\frac{2\varepsilon_s(V_{bi} + V)}{qn_{GaAs}}} \quad (4.4)$$

Where $\varepsilon_s = \varepsilon_\infty$, the built-in voltage $V_{bi} = 0.9$ V at the Schottky junction interface between the Au (ELC) and n-GaAs, $n_{GaAs} = 2 \times 10^{16}$ cm⁻³, and V is the applied voltage (taking positive values upon reverse bias). The unbiased depletion resulting from the V_{bi} is determined to have a depletion width of 250 nm. We model the depletion layer, which we restrict to being directly underneath the metal. Breakdown and depletion width studies of n-doped GaAs have shown relatively close match to theory and have shown x_n beyond a micron can be achieved^[110,111]. In our model we represent the depletion at maximum reverse bias $V_{bias} = -26.5$ V by sweeping n_{GaAs} underneath the 250 nm unbiased depletion width and keeping $\tilde{\varepsilon}_{GaAs}(\omega)$ constant in the volume of the epi-layer beyond the ELC metal boundary.

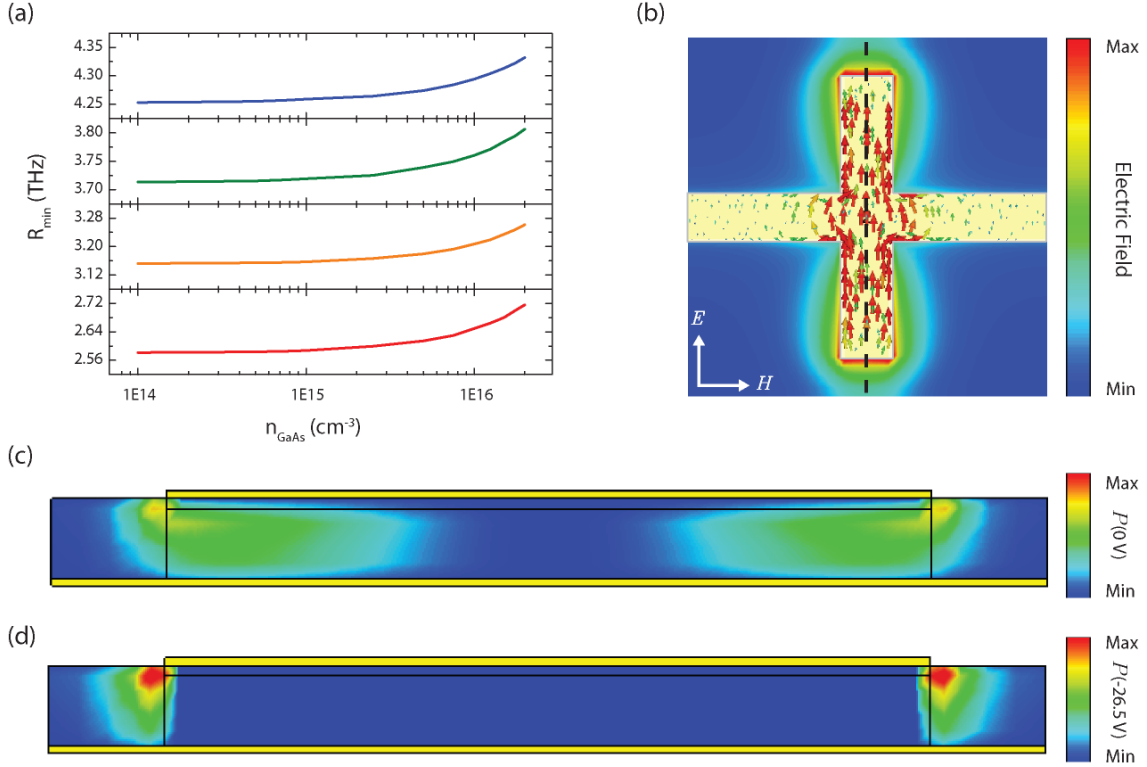


Figure 4.7 Numerical simulation results of the metamaterial absorber. (a), Frequency location of the reflectance minimum (R_{min}) as a function of carrier concentration n_{GaAs} in the n-GaAs epitaxial layer which lies underneath the ELC Au metal and 250 nm threshold depletion layer. (b), Simulated current density in the ELC and the electric field magnitude plotted in plane for the case of the unbiased reflectance minimum $R_{min}(V_{bias} = 0) = 2.72$ THz as indicated by the red dashed line in Fig. 4.6(a). (c,d), Power loss density shown for a cross sectional cut (dashed black line in b), for V_{bias} equal to 0 V (c) and -26.5 V (d).

Results from our computational model are plotted as the dashed curves in Fig. 4.6(a-d) and show excellent agreement with experiment. Notably, as n_{GaAs} is changed from $2 \times 10^{16} cm^{-3}$ to $1 \times 10^{14} cm^{-3}$ the tunability in the reflectance saturates as shown in Fig. 4.7(a), in agreement with experiment. The mechanism of tunability of the metamaterial absorber can be explored by observation of the surface current density and magnitude of the THz electric field (plotted directly underneath the ELC) as shown in Fig. 4.7(b). We find that the surface current density is similar to that found in prior investigations^[23] and, as expected, the THz electric field is primarily localized underneath

the ELC focused just beyond the gap edge. Unlike the electric field distribution which is relatively unchanged, the power loss density distribution, shown in Fig. 4.7(c,d) for both the unbiased and maximum bias cases, is strongly dependent on carrier density spatially located through the epi layer with the loss removed from the depleted volume. The form of the metamaterial absorptive feature strongly depends on the value of the complex dielectric constant that the local terahertz electric field experiences. In particular the resonant frequency is set by the real part of the dielectric function, whereas the width of the absorption is determined by dielectric loss. Thus future designs can achieve greater modulation of the absorption peak by either removing the region of the epi layer that is not depleted or operate at lower frequencies where simulations indicate modulation depth can be improved due to increased damping of the resonance.

Alternatively, tuning of the MMA resonance frequency can be further exploited to enhance the modulation of the reflected THz electromagnetic phase for potential avenues of developing phase SLMs. In Fig. 4.8 the relationship between the modulated amplitude and phase of the reflectance for each color sub-pixel is shown as determined from the model fits calculated in Figs. 4.6(a-d). Interestingly, at the intersection point of the reflectance curves (dashed lines) lies the maximum phase shift, spanning from 32° to 64° across the different color sub-pixels. These points relate to cases of constant insertion loss with a respective increase from -3.5 dB to -7.7 dB due to both a drop in the frequency redshift of the reflectance minimum as well as a decrease in the reflectance minimum value. In theory, dynamic MMAs can be exploited further due to the slope of the reflectance about the minimum, as the phase is proportional to the derivative of the

amplitude with respect to the frequency^[66], thus one can achieve minimal insertion losses with an extremely high degree of modulation in the phase.

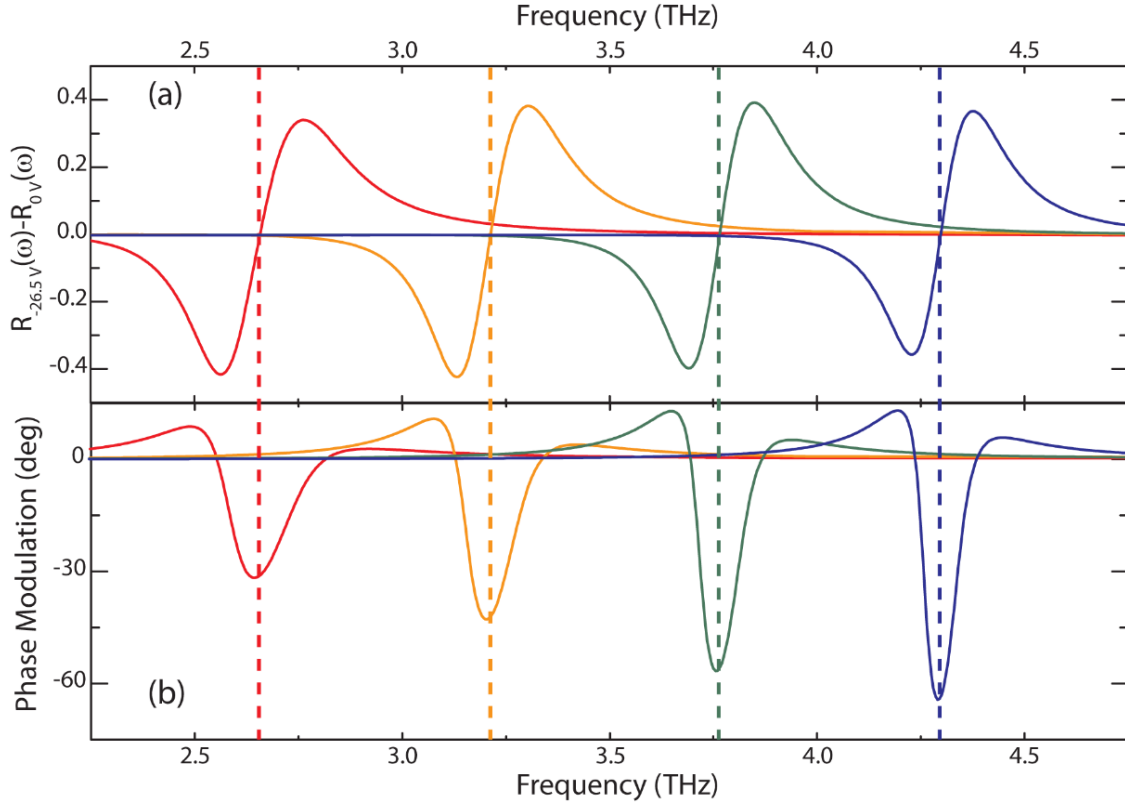


Figure 4.8 Simulation results for reflected amplitude and phase modulation shown for each color sub-pixel. (a), The amplitude modulation $R_{-26.5V}(\omega) - R_{0V}(\omega)$ calculated from the reflectance curves shown in Figs. 4.5(a-d), a dashed line at the zero crossing coincides with the maximum change in phase. (b), Corresponding phase modulation.

The pixels perform collectively as a SLM and we individually characterize the tunable reflectance for each pixel. In Fig. 4.9(a) a spatial map of the maximum absolute change in reflectance $|\Delta R(\omega)| = |R_{-26.5V}(\omega) - R_{0V}(\omega)|$ is shown. Our THz MMA-SLM demonstrates tunable reflectance that spans from 25% to over 50% change in total reflectance, corresponding to a maximum modulation depth ($\Delta R/R_{max}$) of 69%. Our fabricated device had two dead pixels, displayed as black in Fig. 4.8(a), which is therefore unmodulated.

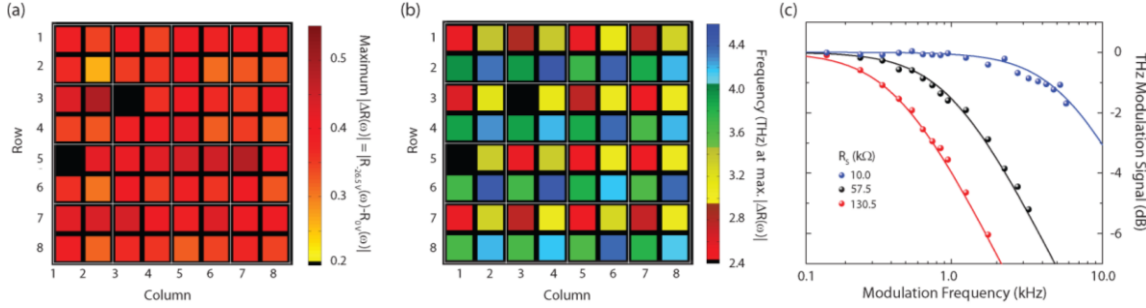


Figure 4.9 Spatial light modulator performance. (a), Magnitude of the maximum change in reflectance $|\Delta R(\omega)| = |R_{-26.5V}(\omega) - R_{0V}(\omega)|$ shown for each pixel. (b), The corresponding frequency for each pixels respective $|\Delta R_{max}(\omega)|$. (c), The measured RC time constant by loading with an external series resistor R_s , where the solid curves represent the fits used to calculate the device roll-off.

The frequency at which the minimum in reflectance occurs is displayed as a false color plot in Fig. 4.9(b). The 2 x 2 multi-color subarray, outlined in white, is replicated across the entire 8 x 8 spatial array with each color appearing distinct from one another. The operational frequency of each of the four color pixels was chosen to minimize spectral overlap, which allows for both spatial and spectral information to be gathered in parallel by creating an effective 4 x 4 spatially modulated array with four uniquely controlled frequencies.

In order to quantify advantages our semiconductor based MMA-SLM has over current state-of-the-art devices, we characterized the modulation speed and the results are shown in Fig. 4.9(c). We input a square wave voltage between 0 and -10 V, and sweep the modulation frequency allowing us to measure the device RC time constant as has been done in previous studies^[62], where by loading external series resistors R_s , the device capacitance can be extracted. The forward resistance R of the Schottky diode is measured to be 4.7 Ω . The depletion capacitance C is extracted by using three different external series resistors of 10.0, 57.5 and 130.5 k Ω , providing measured roll-off of 10.0, 1.70 and 0.78 kHz respectively. The solid curves in Fig. 4.9(c) represent the fits to the

experimental data using the RC time constants as the fitting parameter. The resulting 3 dB roll-off frequency f_c of 12 MHz was determined from these fits. The improved modulation speed, compared to previous metamaterial designs^[62], is a result of having the ohmic ground plane directly underneath the Schottky layer which minimizes the device capacitance. Another added benefit of our ohmic ground plane configuration is that THz radiation is shielded from the carrier wire routing thus allowing for higher filling factors which further accommodates larger array sizes.

In conclusion, we have demonstrated, for the first time, an all-electronic multi-color spatial light modulator with super-pixels composed of arrays of terahertz metamaterial absorbers. Our device is capable of modulation of THz radiation at frequencies up to 12 MHz and a maximum modulation depth of 69%. By utilizing a flip-chip bonded n-doped gallium arsenide epitaxial layer in the metamaterial absorber, we are able to achieve high pixel density and minimal device capacitance thus allowing for high speed modulation. Our design is scalable and may accommodate large active areas for much larger pixel count as required for high resolution applications. This work demonstrates a new path for construction of high speed terahertz electronic devices and has implications in numerous scientific and technological areas rich in applications, particularly in sensing, imaging, and dynamic scene projectors.

CHAPTER 5

5. Terahertz single pixel imaging with an optically controlled dynamic spatial light modulator

Although there exists great technical difficulty in feasibly performing THz imaging, there has been moderate progress over the past 25 years. Multi-element detector schemes, both microbolometer arrays [112,113] and electro-optic sampling with high-performance CCD cameras [114], provide accurate and real-time THz images. However, these imaging systems often require high powered sources and/or expensive complex detectors that lack the sensitivity of single element detectors. The use of a single detector has been employed to obtain THz images by mechanically raster scanning the object plane to acquire spatial information [115]. While the latter technique has the benefit of high spatial resolution and accurate imaging, major shortcomings are the long acquisition time [116] and the mechanical nature of the scanning system.

An alternative single pixel solution - relying on spatial multiplexing - could help overcome many of the disadvantages involved with more conventional imaging techniques. The imaging of complex scenes is enabled with sparse detector arrays or even single pixels using spatial light modulators (SLMs) to multiplex the image. Mechanical masks that are either manually exchanged or placed onto spinning discs have demonstrated proof of principle THz imaging using, for example, compressive sensing and adaptive coded aperture imaging [117-119]. Although SLMs, such as digital micro-mirror (DMD) [120] and liquid crystal (LC) [121] systems are commercially available, they do not operate at THz frequencies. Attempts to develop THz SLMs have thus far

been ineffective in producing efficient and high speed devices, though there are several attractive alternatives to using mechanical masks.

Semiconductor and metamaterial / semiconductor hybrid devices can be controlled by a variety of different methods to achieve THz amplitude and frequency modulation as were outlined in the introduction to dynamic metamaterials in Chapter 1. Another avenue besides metamaterials to achieve a THz SLM has been inspired by the work initially developed at millimeter wavelengths where optically excited electron plasmas in photo-active semiconductors serve as a spatial mask in creating Fresnel lenses and reflect-arrays for beam-steering and communication based applications [122,123]. Early studies indicate that THz spatial modulation is also possible with sufficient optical power [124-126]. Both electronic and optically controlled SLMs pose as a fast and efficient means to dynamically control electromagnetic radiation thus allowing for realistic methods to perform THz imaging.

In this work we demonstrate single pixel multiplex THz imaging based on an optically controlled reconfigurable THz mask in high-resistivity Silicon (ρ -Si) [45]. By utilizing a DMD to optically encode spatial patterns we are able to achieve up to 1023-pixel, high fidelity THz images with frame rates as fast as one image per two seconds - only limited by available software. The achieved signal-to-noise ratio (SNR) suggests the possibility that our technology may provide quasi real-time THz imaging with frame rates as fast as 3 frames per second (fps).

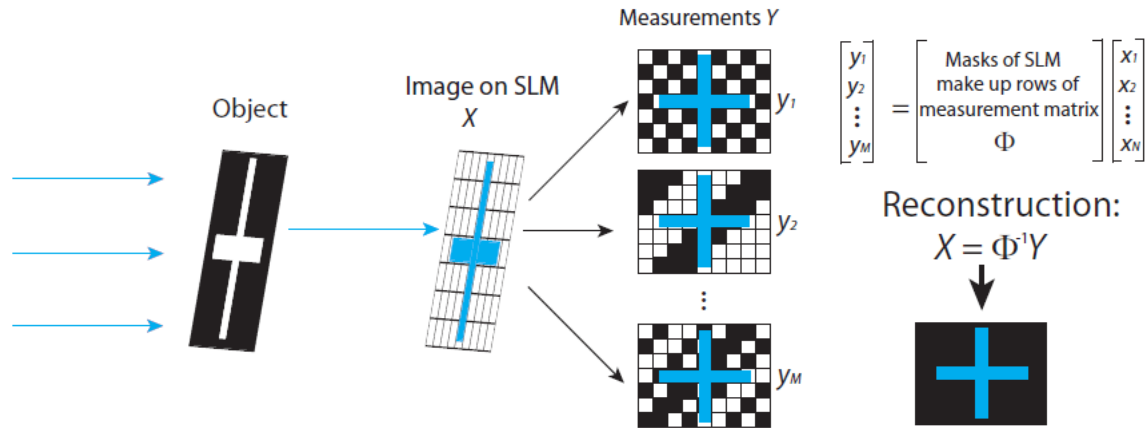


Figure 5.1 Schematic depicting multiplex imaging process where the spatial modulation of a formed image allows for the reconstruction using a single pixel detector.

5.1. Theory

5.1.1. Imaging Theory

Typical single pixel camera architectures involve four key components: a light source, imaging optics, a single element detector, and a SLM. Light from an illuminated object is focused using imaging optics onto a SLM which, for binary encoding, selectively passes portions of the image to the detector and blocks others. A sequence of known patterns is displayed on the SLM and a single value is acquired for each mask frame. Prior knowledge of these masks allows for the reconstruction of the image as schematically illustrated in Fig. 5.1. For example, mechanical raster scanning can be emulated by displaying a single pixel at a time on the SLM.

For imaging systems using intensity based detectors that are not sensitive to the phase of electromagnetic radiation, binary masks that modulate the intensity are well suited. There are several different types of binary coded apertures that can be used to multiplex an image - though the field is dominated by random and Hadamard based masks. Random binary masks are comprised of 1's and 0's determined by standard

probability distributions such as Gaussian or Bernoulli, among others. Hadamard matrices are square matrices composed of +1's and -1's in which each row is orthogonal to all other rows [127]. To create binary masks we can use an S -matrix, created by omitting the first row and column of the corresponding normalized Hadamard matrix, substituting all 1's with 0's, and all -1's with 1's. Each row of this matrix can then be used as a 1, 0 mask for successive measurements in a single pixel imaging system.

We define a one- or two- dimensional image by a vector X with N -elements (this can be done by concatenating the rows into a single column). We represent a single measurement y_j in a multiplexing scheme by the following expression:

$$y_j = \sum_{i=1}^N \phi_{ji} x_i \quad (5.1)$$

or the matrix equation $Y = \Phi \times X$. In this equation, Y is a column vector with M -elements representing the M measurements taken and Φ is the $M \times N$ measurement matrix, in which each row represents a mask displayed on the SLM. For example, Φ that corresponds to a raster scan imaging technique is the $N \times N$ identity matrix. For a well conditioned measurement matrix [128] and the fully determined case, i.e. $M = N$, the reconstruction becomes linear and can be solved by a simple matrix equation: $X = \Phi^{-1} \times Y$ [127]. One advantage of using S -matrices as the measurement matrix such that $\Phi = S_N$ is the particularly simple decoding process given by: $S_N^{-1} = \frac{2}{N+1} (2S_N^T - J_N)$ where S_N is the S -matrix of order N , S_N^T is its transpose, and J_N is an $N \times N$ matrix of all 1's [127].

5.1.2. Dynamic THz spatial light modulators

The photoexcitation of free carriers in semiconductors is a well understood process for both CW and ultrafast optical beams [129]. For ρ -Si substrates a higher carrier density can be generated by CW pump beams, compared to pulsed sources, due to the relatively long carrier lifetimes in Si [130]. The change in the complex dielectric constant can be described by the Drude model [130-133]

$$\varepsilon(\omega) = \varepsilon_{\infty} - \frac{\omega_p^2}{\omega(\omega + i\Gamma)} \quad (5.2)$$

where $\varepsilon_{\infty} = 11.7$ is the frequency independent dielectric permittivity due to the contribution of bound electrons, $\Gamma = 1/\tau_c$ is the damping rate (with $\tau_c = 160$ fs the average collision time [130,133]), ω_p is the plasma frequency defined as $\omega_p^2 = n_{Si}e^2/\varepsilon_0m^*$ with e the electron charge, ε_0 the free-space permittivity, and $m^* = 0.26m_e$ the effective mass [133]. If we neglect the carrier diffusion and consider only free carrier generation and linear recombination in the semiconductor, the carrier density n_{Si} is proportional to the optical power of the pump beam and is modulated through photodoping [132]

$$n_{Si} = \frac{I_0(1 - R)\tau}{2Ad\hbar\omega} \quad (5.3)$$

where I_0 is average power, R is the reflectance of Si at the pump wavelength, $\hbar\omega$ is the photon energy, $\tau = 25 \mu\text{s}$ is the carrier lifetime [134], A is the area of the laser excitation, and d is the penetration depth. At THz frequencies the photodoped charges correspond to a large increase in the absorption coefficient as a function of I_0 , allowing for strong attenuation of incident THz electromagnetic waves.

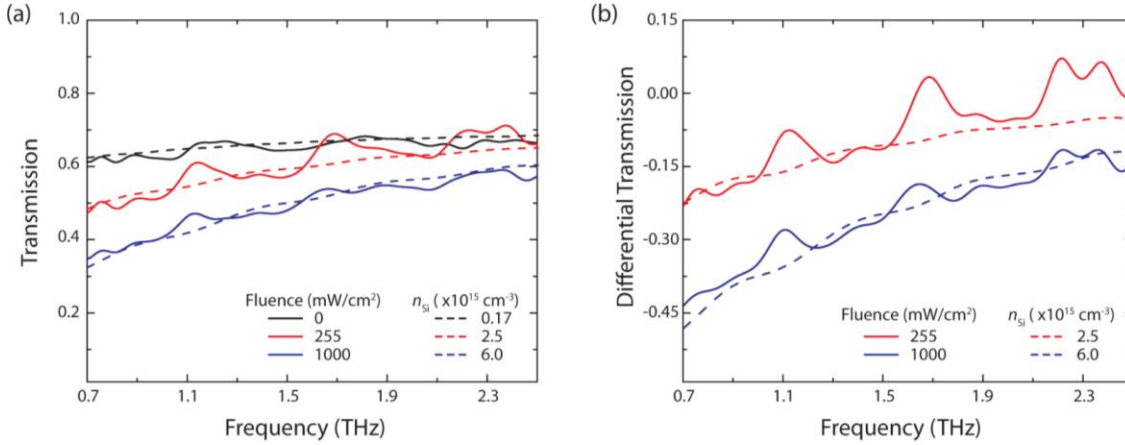


Figure 5.2 (a) Solid curves show the transmission of THz radiation through ρ -Si wafer as a function of frequency for several different optical fluence values. Measurements were done in atmosphere in FTIR system. The dashed curves show the simulated fits for increasing carrier concentration n_{Si} within the penetration depth (85 μ m) of ρ -Si. (b) Dependence of the differential transmission on the optical fluence as defined in the text.

We measured the THz transmission, shown as the solid curves in Fig. 5.2, through a 520 μ m thick ρ -Si substrate ($\rho > 10,000$ ohm-cm) for increasing optical power using a 980 nm CW laser diode. We characterize the THz transmission using a Fourier Transform Infrared (FTIR) spectrometer, a mercury (Hg) arc lamp source, multi-layer mylar beamsplitter, and liquid-helium cooled silicon bolometer. Etalons due to multiple reflections within the ρ -Si substrate were removed and the modified interferogram was Fourier transformed to obtain the sample spectrum. A similar procedure was performed for a reference with an open channel; division of the sample and reference spectra resulted in the frequency dependent absolute value transmission $T(\omega)$ and corresponding differential transmission $[T_p(\omega) - T_{p=0}(\omega)]/T_{p=0}(\omega)$ shown in Fig. 5.2. We observe broadband attenuation of the THz signal where, at our maximum fluence of $p = 1$ W/cm², we measure a modulation depth of 43% at 0.7 THz. The undoped ($T_{p=0}(\omega)$, black curve) of Fig. 5.2(a) was performed in vacuum; however, due to technical limitations,

transmission measurements for both photodoped cases were performed in air - leading to a reduced signal-to-noise which accounts for the large fluctuations in $T(\omega)$.

The dashed curves in Fig. 5.2 are the results of full wave 3D electromagnetic simulations where we model the resulting change in the transmission as a function of an increase in the ρ -Si conductivity using the commercial FDTD solver CST Microwave Studio 2012. In simulation we define the ρ -Si within the penetration depth, $d = 85 \mu\text{m}$ [130], as a Drude layer, described by Eqs. 5.2 and 5.3, with increasing n_{Si} . Below the penetration depth the ρ -Si is treated as a dielectric with a constant complex permittivity $\epsilon_{Si} = 11.7 + 0.01i$. The photogenerated carrier density approached $6 \times 10^{15} \text{cm}^{-3}$ for the maximum fluence, in agreement with previous work [130]. The strong frequency dependence of the imaginary component of the dielectric permittivity within the photoexcited region results in high absorption at lower frequencies and minor attenuation above several THz. The qualitative agreement between the model and experimental measurements demonstrate that optically controlled broadband THz modulation is possible with the carrier lifetime in ρ -Si being sufficient to allow for modulation beyond 10 kHz switching speeds.

5.2. Experimental setup

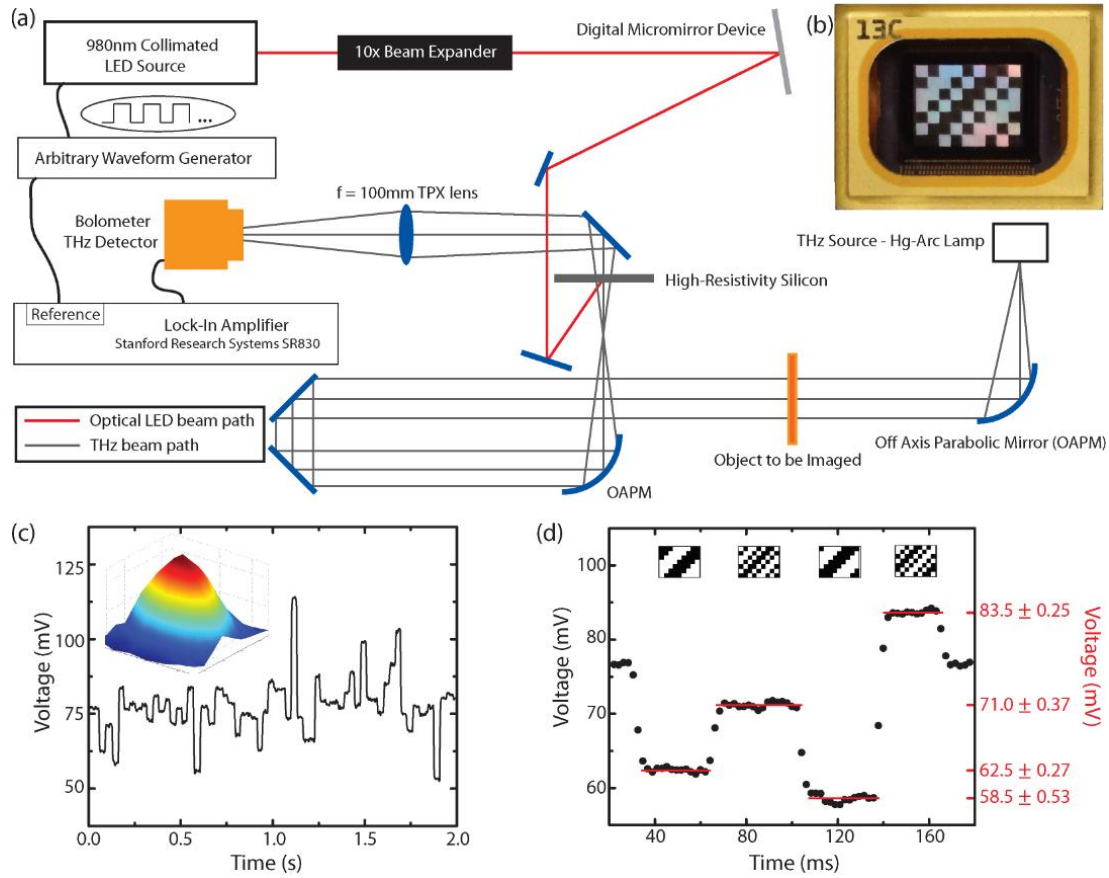


Figure 5.3 (a) Schematic of LED and THz optical layouts. The THz beam (shown in gray) passes through the object and is imaged with the OAPMs onto a ρ -Si wafer. The collimated 980 nm wavelength optical beam (shown in red) reflects off the DMD surface and creates a spatial light pattern at the THz image plane. (b) Photograph of a 7×9 S-matrix mask pattern displayed on DMD; each mask pixel is 1.5 mm being constructed from tiling 109×109 DMD pixels. (c) Lock-in amplifier voltage output is displayed as a function of time in seconds for the 63 sequential S-matrix masks; the entire measurement takes approximately 2 s. Inset: reconstructed THz beam profile at image plane. (d) Zoom-in of time data shown in (c). Raw data from four consecutive S-matrix mask measurements are shown with the corresponding binary mask shown above; the averaged values used for reconstruction along with the standard deviation are shown on the right.

A schematic of the THz imaging system is presented in Fig. 5.3(a) and consists of both an optical beam path (red lines) and a THz beam path (gray lines). As a broadband THz source we utilize a Hg-Arc lamp which emulates a 5500 K blackbody. The source is used in conjunction with a long-pass filter (LPF-065 from Lakeshore) that blocks

wavelengths shorter than $65\ \mu\text{m}$ ($> 4.6\ \text{THz}$). The THz imaging optics consist of two $50.8\ \text{mm}$ diameter 90° off-axis parabolic mirrors (OAPMs) each with an effective focal length of $f_L=190.6\ \text{mm}$. The first OAPM is f_L from the source and back-illuminates the object a distance $150\ \text{mm}$ away. The second OAPM, a distance $933\ \text{mm}$ from the object, focuses the radiation and forms a conjugate image on the SLM $215\ \text{mm}$ away. The system has an overall magnification of 0.23 , mapping the $43.5\ \text{mm}$ diameter object to approximately $10\ \text{mm}$ at the SLM. An image was formed by placing a back illuminated patterned metal aperture (examples shown in Fig. 5.5) between the OAPMs so that a THz image ($10\ \text{mm}$ in diameter) was formed at the SLM plane. The THz image is transmitted through the ρ -Si and focused using a $50.8\ \text{mm}$ diameter TPX lens with $f = 100\ \text{mm}$ to the detector - a liquid-helium cooled silicon bolometer. The entire apparatus is enclosed and is purged by dry air at room temperature to reduce the THz absorption due to water vapor.

An optical beam is used to spatially modulate the THz image and consists of a $2\ \text{W}$ multimode laser diode at a wavelength of $980\ \text{nm}$. An aspheric lens collimates the laser and a Galilean beam expander is used to produce a beam which slightly overfills the DMD. Light is reflected from the DMD in the blaze configuration (described below) and the spatially patterned optical beam is aligned to overlap with the THz image at the front surface of the ρ -Si wafer achieving a maximum optical fluence of $250\ \text{mW}/\text{cm}^2$. The DMD shown in Fig. 5.3(b) is utilized to spatially modulate the optical beam by configuring it as a blazed diffraction grating. Our DMD (DLP D4100-2XLVDS) has a window optimized for the transmission of NIR and 1024×768 micro-mirrors (total area $14.0\ \text{mm} \times 10.5\ \text{mm}$), where each mirror has a pitch $d_{DMD} = 13.68\ \mu\text{m}$ and behaves as a

binary reflector. By aligning the angle of incidence correctly, the majority of the energy can be directed into the "blazed" order [135]. The blazed condition for wavelength λ_B is related to the grating pitch $d = d_{DMD}/\sqrt{2}$, the diffraction order m , and the facet angle $\phi = 12^\circ$ as shown in Eq. 5.4. The fourth blazed angle is centered at $\lambda = 984$ nm with an efficiency of 47% [136].

$$\lambda_B = \frac{d}{m} \sin 2\phi \quad (5.4)$$

The DMD is computer controlled and able to change between frames up to a (software limited) time of 32 ms. Binary bitmap files are loaded into the software to be displayed on the DMD; examples are shown in Fig. 5.3(d). The white portions represent light that was directed toward the ρ -Si whereas black represents light that was directed away. This corresponds to white mask regions photodoping the ρ -Si, i.e. modulating the THz transmission where black represents unmodulated regions. Since the DMD is designed for much shorter optical wavelengths, we may utilize several mirror pixels to function as a single THz-sized pixel for the S -matrix mask, thus permitting flexibility for both pixel count and pitch. We use S -matrix masks of varying complexity and change the pixel size accordingly to keep the overall mask area approximately equal. The THz image resolutions we investigated are summarized in Table 5.1 and the relation between physical size and DMD pixels is detailed.

Table 5.1 Relationship between THz imaging resolution and DMD pixel sizes.

Order (N)	Resolution	THz Pixel Size	DMD Pixels / THz Pixel
63	7×9	1.5 mm \times 1.5 mm	109 \times 109
255	15×17	698 mm \times 698 mm	51 \times 51
1023	31×33	328 mm \times 328 mm	24 \times 24

Detection of the THz signal is performed with a lock-in detection technique. The laser diode power is modulated with a square wave at a frequency of 300 Hz, which in turn modulates the THz power detected. Output voltage from the Si-bolometer is input into a lock-in amplifier which provides the measured THz signal in Volts. Figs. 5.3(c,d) show the measured lock-in voltage as a function of time for several successive masks. The stabilization of the lock-in signal after switching between masks is close to 5 ms, with a SNR recorded for each measurement greater than 100; this is sufficient to allow us to acquire a THz measurement at the limits of the switching time of the DMD. We may estimate the total power of THz radiation used in our imaging apparatus since our bolometer has a calibrated responsivity of 2.64×10^5 V/W at 300 Hz. Our DMD may be configured to modulate all pixels on and off, from which we measure a lock-in signal of 130 mV. Thus our THz image consists of a maximum modulated THz power of 96 nW over an integrated bandwidth from 0.2 - 4.6 THz.

5.3. Experimental Results and Discussion

Using the experimental apparatus shown in Fig. 5.3 we performed single pixel THz imaging of various scenes. All THz images are normalized by referencing to the beam profile with no object present. The flexibility afforded by our setup enabled us to image at many different mask resolutions and sizes without physically changing the system. Fig. 5.3(c) shows the THz signal for 63 different *S*-matrix masks displayed over a period of 2 s (each mask is displayed for approximately 32 ms). Fig. 5.3(d) shows zoomed-in raw data for consecutive *S*-matrix masks, with the corresponding binary mask shown above and the average value used for reconstruction shown in red on the right axis. The inset to

Fig. 5.3(c) shows a false color image of the THz beam profile at the image plane. The reconstruction was done using 63 measurements from the 7×9 S -matrix masks (pixel size 1.5 mm) with the total measurement time of approximately 2 s. It is clear from the data shown that quality THz images can be acquired in relatively short times. As stated, the current limitation on speed is software related resulting in mask modulation speed of approximately 31 Hz. However, the response time of the system to a change in mask is approximately 5 ms, resulting in a potential frame rate of 3 fps.

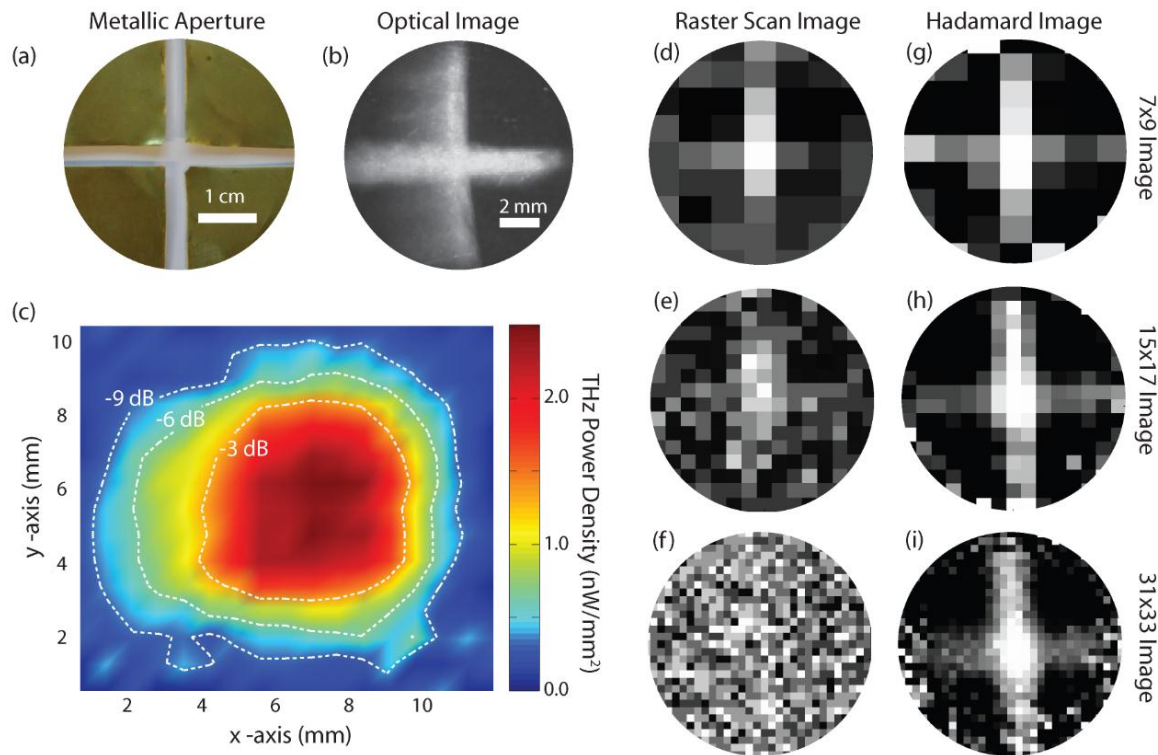


Figure 5.4 Comparison of THz imaging with raster scan masks and S -matrix masks. (a,b) Show the metallic aperture used as the object and the conjugate optical image on the ρ -Si wafer. (c) Spatial map of the THz power density shown for the reference beam profile with contour plots showing the intensity drop in dB. (d) - (f) Shows raster-scan images for increasing mask complexity. (g) - (i) Shows Hadamard reconstructed images of the same size and complexity as the raster scan measurements to the immediate left.

In order to compare our imaging system to more conventional schemes, we perform both raster scan and Hadamard imaging and highlight differences between the

two methods - see Fig. 5.4. S -matrix masks consist of roughly 50% light throughput and it has been demonstrated that using masks created from an $N \times N$ S -matrix can increase SNR by a factor of $\frac{N+1}{2\sqrt{N}} \cong \frac{\sqrt{N}}{2}$ over raster scan imaging with the same resolution and pixel size [127]. Figs. 5.4(a,b) shows both the metallic aperture used as an object and an optical photograph of the conjugate image at the front surface of the ρ -Si wafer. Figs. 5.4(d-f) shows raster-scan images acquired with increasing resolution and constructed from 63, 255, and 1023 measurements respectively. The last column in Fig. 5.4(g-i) shows Hadamard reconstructions with the same number of measurements and resolution as the raster scan images. While the image quality in the case of 7×9 pixel resolution is comparable between the two techniques, the rapid decrease in image quality for the raster scan images at higher resolutions is apparent - see Fig. 5.4(f). In contrast, the image quality is retained for increasing pixel count in the multiplexing case.

To better understand why the signal depreciated significantly for increasing pixel complexity in the case of the raster scan we investigated the measured power for each respective mask type. We calculate the spatial dependence of the power density (nW/mm^2) by taking the total measured THz power (96 nW) and extracting the THz power density per pixel p_i from the measured 15×17 beam profile intensity as defined by

$$p_i = \frac{96 \text{ nW}}{(698 \text{ } \mu\text{m})^2} \times \frac{x_i}{\sum_{i=1}^{255} x_i} \quad (5.5)$$

where x_i is the reconstructed signal from pixel i . In Fig. 5.4(c) we show a high quality image of the power density - sufficient to observe optical aberrations resulting from the use of OAPMs which result in an asymmetric distribution of THz power about the

horizontal axis. The power/pixel decreases for increasing resolution since the pixel size is reduced - in our case from 1.5 mm to 698 μm to 328 μm . The peak power density calculated in Eq. 5.5 is 2.5 nW/mm^2 near the center of the beam. This corresponds to a total of 5.6 nW of measured power for the 1.5 mm size pixel and 0.27 nW for the 328 μm pixel, a 95% reduction of measured power proportional to the decrease in pixel area. As shown in Fig. 5.4(c), the power density is -9 dB lower towards the outer diameter of the images and approaches values as low as 50 pW of THz power for 328 μm sized pixels - still well above the bolometer's specified noise-equivalent-power (NEP) of $1.57 \times 10^{-13} \text{ W}/\sqrt{\text{Hz}}$. The raster scan is unable to compensate for the loss in measured signal for each pixel due to decreasing pixel dimension. In the Hadamard case, although the signal per pixel also drops due to decreasing pixel size, the increase in sampled pixels for each data acquisition offsets the reduction in signal. Consequently, the higher resolution image offers more information without sacrificing SNR. The improvement in the image quality for increasing pixel complexity is evident and allows for the aberrations of the THz image resulting from the OAPMs to be rendered.

In order to explore our imaging technique for possible use in screening applications, in Fig. 5.5 we show various examples of high-fidelity THz images. The top row displays photographs of all the objects imaged: crosses with 8 mm and 4.5 mm wide arms at the object plane (Fig. 5.5(a,b)) and two razor blades imaged in manila envelopes (Fig. 5.5(c,d)). As stated above, we can program the S -matrix masks to allow for several different functions and mask complexities. We achieved high resolution images containing 31×33 pixels with each mask pixel measuring 328 μm across; this was acquired with 1023 sequential measurements. The reconstructed THz images are shown

in Fig. 5.5(e-h). Due to the magnification of the system, the crosses are imaged down to have 2.5 mm and 1.5 mm wide arms, respectively. The minimum feature size of the images that we can resolve for these crosses is limited according to the Rayleigh Criterion with a diffraction limited spot size of approximately 1.4 mm at 1 THz. The razor blades are placed within manila envelopes and are, obviously, not visible in the optical, however are clearly identified in the THz images, demonstrating the potential for THz imaging to be used in security applications.

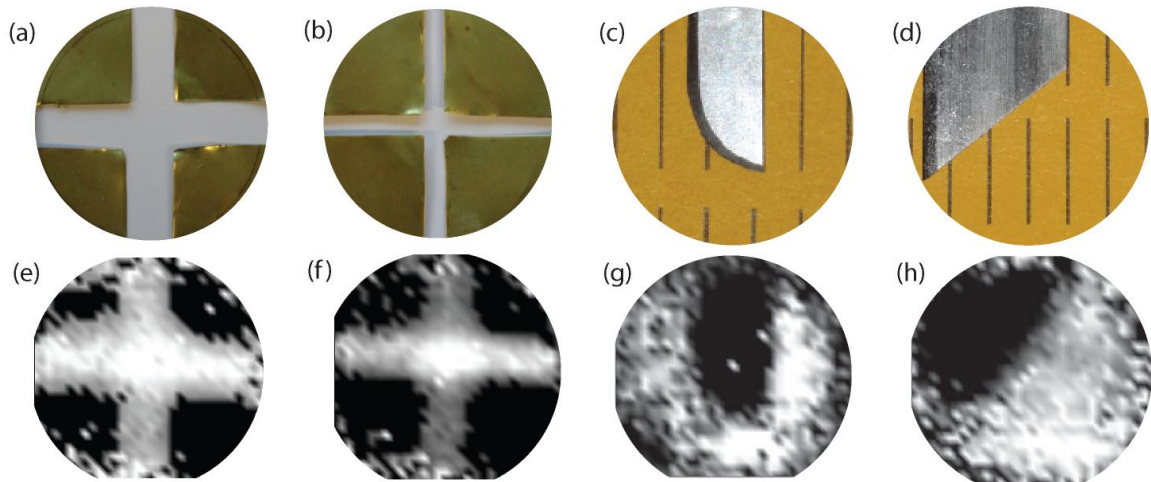


Figure 5.5 THz imaging with high-resolution S -matrix masks (31×33 pixels with each pixel measuring $328 \mu\text{m}$ on a side). (a,b) Show metallic apertures used as the object of two differently sized crosses, with arm widths of approximately 8 mm and 4.5 mm in the object plane mapping to 2.5 mm and 1.5 mm on the image plane. (c,d) Two different types of metal razor blades that were placed in manila envelopes for imaging. (e) - (h) Shows the THz images of the corresponding objects shown immediately above.

5.4. Metamaterial SLMs

Results presented in Figs. 5.4, 5.5 demonstrate the ability to perform THz imaging using a single pixel detector. For many potential applications it would be desirable to obtain spectral information, rather than integrating across a portion of the THz range. As discussed in the introduction, metamaterials have shown an ability to modulate THz electromagnetic radiation with demonstrated advantages over conventional materials,

including spectral selectivity, amplitude modulation [59], and phase modulation [66]. We computationally explore a metamaterial based SLM which is optically controlled - schematically shown Fig. 5.6(a). Our metamaterial SLM is modeled similar to that for the ρ -Si and we add a complimentary electric split ring resonator [33] to the top of the substrate. The optically excited charge carriers shunt the resonant response of the metamaterial (See Fig. 5.6(c)), effectively modulating the transmission at the operational frequency. The metamaterial has been designed to yield a band-pass response centered at 1 THz and achieves a simulated modulation depth of 67% for a maximum fluence of 1 W/cm² - see Fig. 5.6(b).

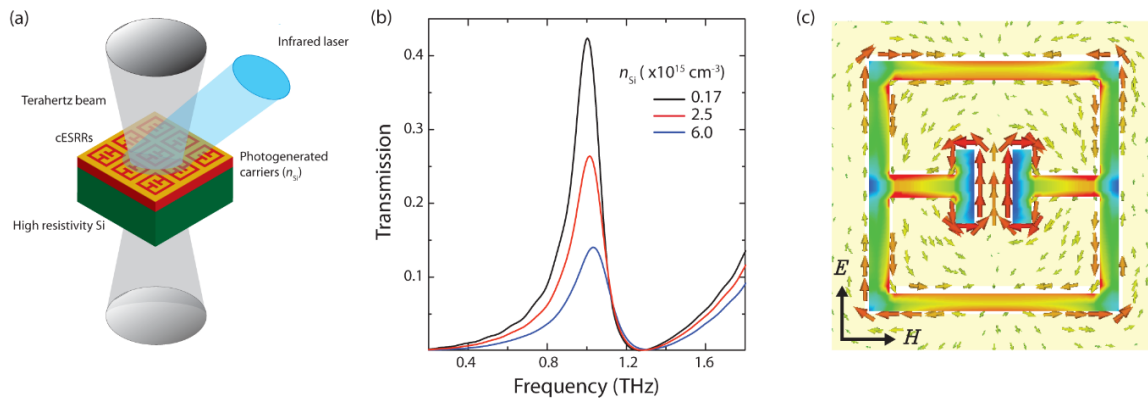


Figure 5.6 Optically reconfigurable THz masks with metamaterials. (a) Schematic showing optical pump beam overlapped with THz incident onto complimentary electric split ring resonators (cESRRs) where the photoexcited carriers in Si underneath metamaterial dynamically tune the EM response of the MM. (b) Simulation showing the modulation in THz transmission as a function of carrier excitation. (c) Simulated current density in the cESRR and the electric field magnitude plotted in plane for the case of maximum transmission at 1 THz.

The advantage in THz imaging provided by adding resonant metamaterials, as demonstrated in Fig. 5.6, is an increase in modulation depth at selected frequencies over bare silicon (67% as compared to 37% at 1 THz). The modulation depth could be further improved by optimizing the geometry of ρ -Si within the metamaterial unit cell, as well as

the photodoping wavelength - both of which could potentially maximize the carrier density closer to the surface. Obtaining spectral information with conventional instruments can be challenging, requiring complex high cost equipment and instrumentation with significantly limited acquisition speeds [137]. By arranging the pixels of metamaterial arrays to have uniquely designed operating frequencies we can create multi-color SLMs that could be used to perform high speed THz spectral imaging offering significant improvement over current systems.

In conclusion, we have performed high fidelity THz single pixel imaging and various scenes have been rendered. An optically controlled spatial light modulator was implemented through photodoping in high resistivity silicon and controlled by a DMD. We use *S*-matrix masks of varying resolution ranging from 63 to 1023 pixels and were able to obtain THz images as fast as one per two seconds. We directly compared Hadamard imaging to the raster-scan technique and highlighted the advantages of the multiplexing method. At THz frequencies dynamically reconfigurable semiconducting device technology provides significant advantages over traditional masks due to the benefit of adaptability and real-time control. This work demonstrates a new path for construction of THz imaging systems. Future work will realize real time imaging of more complex scenes as well as incorporating metamaterials to add additional functionalities applicable to sensing, imaging, and dynamic scene projectors.

CHAPTER 6

6. Microwave Metamaterial Detector Focal Plane Array

Microwave imaging systems working between 8-30 GHz have been used for decades in remote sensing and radio astronomy [138,139]. Common designs are often notably massive and bulky, employing mechanical positioning stages (to raster scan a single pixel across an image plane to build up an image), or using an array of efficient but very substantial elements, such as horn antennas [140]. Though the greatest gains in performance come from increasing the aperture, if compactness, mobility or inconspicuousness are desirable, one would like to have an imaging system that maximizes the performance and minimizes the weight and bulk at a given aperture size. With pixel spacing on the order of the diffraction limited spot size $a \sim \lambda_0/2\pi$ (where λ_0 is the wavelength of the radiation at the imaging frequency), the focal plane can be adequately sampled and all available information acquired. However, such dense spacing is at odds with pixel channel independence. Minimizing cross-talk between detector pixels can require spacings that result in poor resolution and sparse spatial sampling of the image [141-143]. Achieving a high detected-to-incident power efficiency is another key aspect to consider in order to improve the sensitivity. Ideally, one would like to transfer all power to the detector that is incident within the boundaries of a pixel. In all examples to-date there are trade-offs between power efficiency and pixel independence [144,145]. We believe that resonators developed in the metamaterial community can offer different and potentially superior options for pixel density, channel independence and power efficiency.

Here we present a metamaterial absorber (MMA) that operates as a detector of microwave radiation [146]. Each MMA unit cell functions as an individual antenna coupled detector and, collectively, as a focal plane array (FPA). The metamaterial unit cell converts the incident microwave radiation into electric currents, which are guided to a dedicated receiver chain and finally detected with a power detector to produce DC voltage linearly proportional to the signal. All metamaterial elements and receiver system components can be integrated into a single printed circuit board (PCB).

6.1. Design and fabrication

One key design feature afforded by metamaterials is the ability to engineer materials for matching the impedance of the MMA to that of free space. The resonant nature of the MMA structures generates high electric fields in the gap, completely dissipating the incident energy into a combination of dielectric and ohmic losses [38,39]. However, here we modify the MMA design in order to instead transfer the incident energy into a detector circuit. We have utilized the highly absorbing capability of the MMA to fashion a focal plane array by letting each individual unit cell serve as an array element.

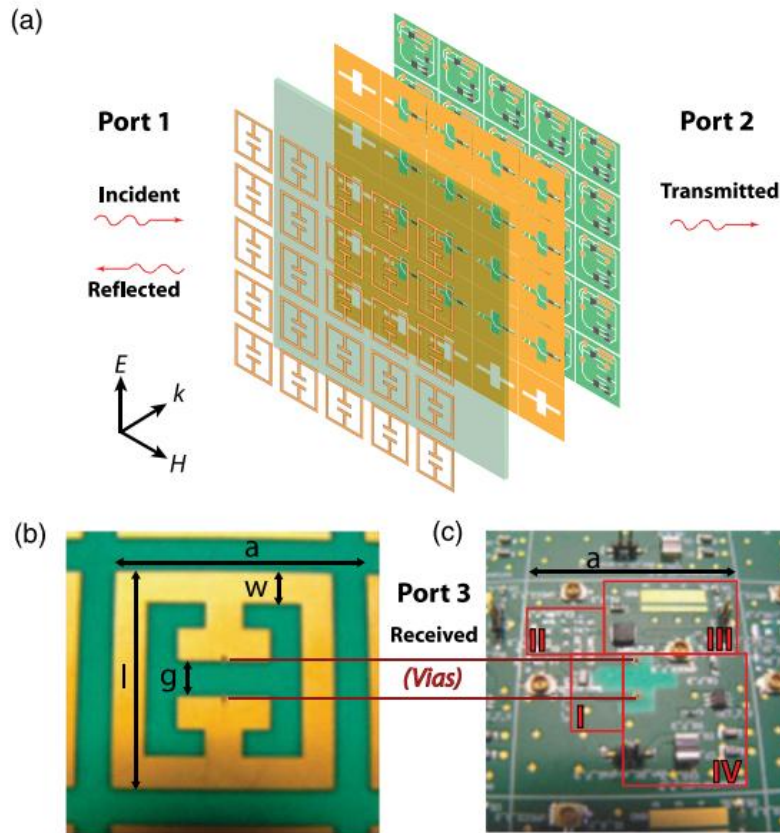


Figure 6.1 (a) System architecture of our metamaterial microwave power detector array. (a) Radiation is incident from port 1 with electric field polarization as depicted. A schematic of the full device is shown (exploded view) and the layers shown from top to bottom are: the ELC, Rogers dielectric spacer, patterned ground plane, and microwave power receiver circuit. (b) Photo of an individual pixel, i.e. an ELC unit cell with dimensions of $a = 27.3$, $l = 24$, $w = 3.5$, and $g = 4$; all in millimeters. (c) Photo of the circuit layer with *vias* indicated. The *vias* transport the received signal (port 3) to the microwave power receiver circuit underneath each unit cell where the different highlighted regions are: (I) balun, (II) impedance matching circuit, (III) low noise amplifier, and (IV) microwave power detector.

The microwave FPA presented here consists of metamaterial unit cells arranged on a square lattice of 11 by 11 elements. The entire detector system architecture -- all contained within the footprint of each unit cell -- consists of the metamaterial absorber followed by a balun, impedance matching circuit, low noise amplifier (LNA) and a microwave power detector. The FPA has been implemented in a twelve layer commercial PCB process fabricated and assembled by Hughes circuits, including four metal layers

and *vias*, see Fig. 6.1. The device is constructed from a 30.5 μm copper layer which constitutes the electrically coupled LC (ELC) resonators [23,24], followed by a patterned ground plane, power routing plane, and the circuit layer -- where the ELC and ground plane are separated by Rogers 4003 dielectric with a 4.88 mm thickness. Microwave radiation received by the metamaterial perfect absorber is transferred by the 0.5 mm diameter *vias* to the circuit layer where a balun is used to transform the balanced signal to an unbalanced signal. The signal is then fed into the impedance matching circuit which not only maximizes the signal power, but also serves to compensate for variances in the MPA resonance frequency -- due to imperfections in the fabrication process. Finally the signal is amplified by the LNA before being converted to a DC signal by the microwave power detector.

We simulate the design of the entire detector array using commercial 3D electromagnetic simulation software CST's Microwave Studio 2011. The ports, (shown schematically in Fig. 6.1), are used to investigate the transfer of electromagnetic energy in the device and consist of waveguide ports (port 1 and 2), and a discrete port (port 3). The discrete port is a lumped circuit element that connects the *vias* to one another with a defined impedance set equal to 100 Ω , which is equivalent to the input impedance of the balun. The metamaterial was configured to maximize the transfer of energy into port 3, i.e. S_{31} , while at the same time minimize both the free space reflection coefficient (S_{11}) and reflection coefficient (S_{33}) at 2.0 GHz. In order to achieve this goal we tuned the dimensions of the MMA; consisting of the ELC geometry, thickness of the Rogers 4003 ($\tilde{\epsilon} = \epsilon_1 + i\epsilon_2 = 3.38 + 0.007i$) dielectric spacer, and the opening in the ground plane. The final dimensions of the ELC resonator are shown in Fig. 6.1(b) with parameters as

labeled. The dimensions of the cross shaped opening in the ground plane, (Fig. 6.1(c)), were optimized to minimize the coupling between the *vias* and ground plane, as well as tune the MMA's effective magnetic response. The ground plane also helps to shield any undesirable coupling effects between the circuit components and the electromagnetic metamaterial performance.

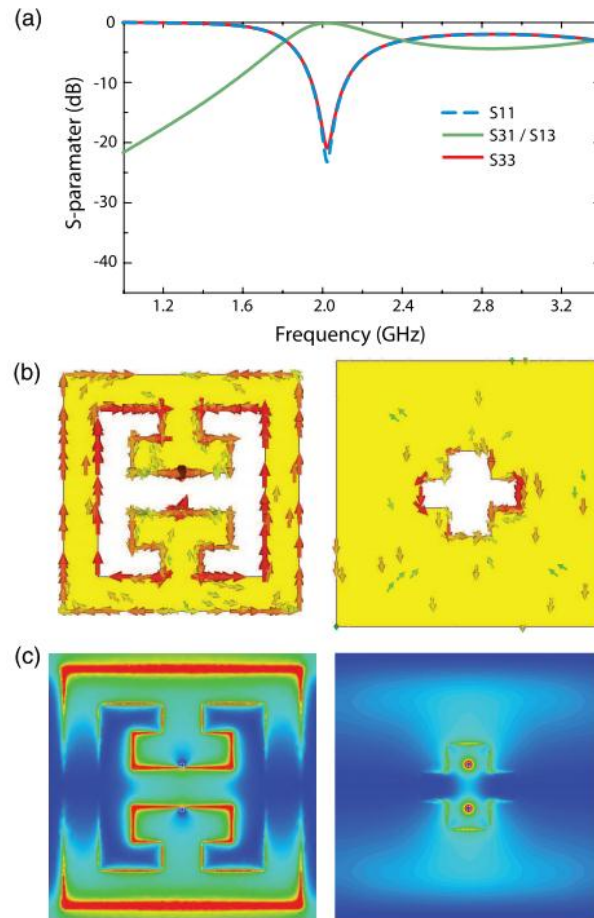


Figure 6.2 Numerical simulations of metamaterial absorber. (a) Simulated results of the free space reflection (S_{11} dashed blue curve), transmission (S_{31} green curve), and reflection coefficient (S_{33} red curve). Simulated current densities (b) and electric field magnitude (c) shown directly underneath the ELC (left) and above the ground plane (right) at the simulated design frequency of 2.0 GHz.

The simulated scattering parameters are shown in Fig. 6.2(a) and demonstrates that a maximum in transmission corresponds with the minima of both reflection

coefficients S_{11} and S_{33} at 2.0 GHz. As mentioned, the MMA design typically utilizes the dielectric and ohmic losses within the constituent components in order to achieve a minimum in S_{11} . In contrast, the design presented here achieves $S_{31} = 0.986$, indicating that over 97% of the incident intensity is transmitted into the detector circuit. In Fig. 6.2(b) we plot the surface current density at resonance and find that our MMA achieves a response similar to prior designs [23]. Fig. 6.2(c) shows the magnitude of the electric field and, as can be observed, the electric field is focused into the ELC split gap (right panel) and the *vias* are sufficiently decoupled from the ground plane.

Although simulations presented above indicate that a high performance MMA unit cell may be used as a detector of incident radiation, tolerances in both the component values and the geometry can occur in the fabrication process and may thus alter the ideal electromagnetic response. Characterization of S_{11} is not possible with our experimental setup. However, simulations presented in Fig. 6.2(a) indicate that S_{33} is a reasonable approximation of S_{11} . Thus we measure S_{33} in order to investigate the resonant properties of the fabricated MMA, shown as the red curve in Fig. 6.3(a). We observe a high reflection coefficient across the range investigated but notably minima occur at 2.5 and 3.15 GHz, with values of -33 dB and -29 dB, respectively. The simulated minimum in S_{33} occurring at 2.0 GHz has shifted to 2.5 GHz, which we attribute to the variation in the fabrication from the simulated design.

Our metamaterial focal plane array exhibited several undesirable deviations from the designed values during commercial fabrication. We characterized various parameters of our device and found errors that include: layer thickness, *via* dimensions, layer alignment (registration), balun impedance, and dielectric values. These variances result in

a reduction of ideal electromagnetic performance which leads to an impedance mismatch between the metamaterial unit cell and the $50\ \Omega$ input circuit modules. Overall, this results in diminished reception of electromagnetic energy due to increased reflection between the metamaterial and detector circuit. We anticipated various fabrication errors and therefore, in the design process, preemptively added a reconfigurable element to tune the impedance of the circuit layer after the metamaterial unit cell. Thus an impedance matching circuit directly following the balun compensates for MMA variances and tunes the strength and frequency of the resonance at the selected operating frequency. Due to the hardware and component limitations we decided to operate at 2.5 GHz, as opposed to the simulated 2.0 GHz operational frequency.

6.2. Results and discussion

Free space measurements of the center pixel were performed within an anechoic chamber. We use a HP 8510B vector network analyzer (VNA) with a double ridge guide horn antenna (700 MHz - 18 GHz range) as a transmitter. The horn was connected to a port of the VNA which provided a power level of -3 dBm. Another port of the VNA was directly connected following the unbalanced signal output of the balun on the center single pixel of the MMA / FPA. The resulting S-parameters measured were for only this center pixel with all neighboring unit cells having $50\ \Omega$ terminations following their respective balun output connections. The MMA / FPA was placed 1.75 m away from the horn antenna to be in the far field of the horn's radiating field pattern. In Fig. 6.3(a), the green S_{31} curve shows a peak about 2.5 GHz overlapping with the minimum observed in S_{33} .

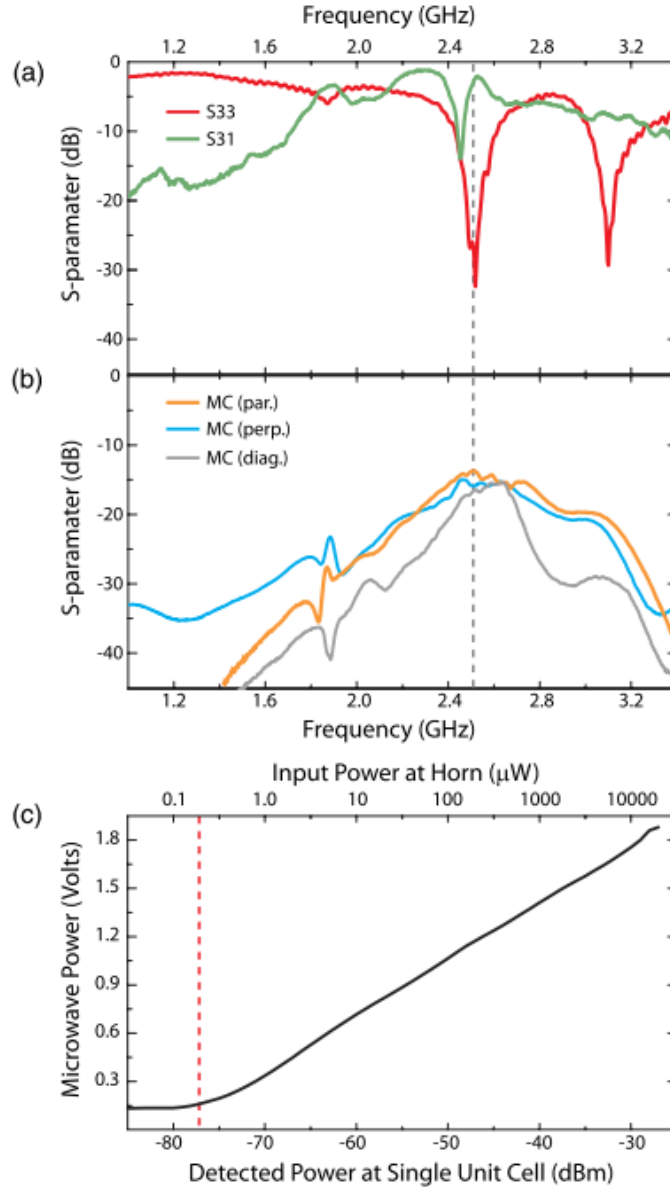


Figure 6.3 Experimental measurements in anechoic chamber for the center pixel on the MMA / FPA. (a) S- parameter data shows the reflection coefficient (S_{33} red curve) and the transmission (S_{31} green curve) with the dashed grey line at 2.5 GHz the frequency for sensitivity and off-angle measurements. (b) Mutual coupling (MC) between neighboring metamaterial pixels located parallel (gold curve), perpendicular (blue curve), and diagonal (grey curve) with respect to the electric field polarization. (c) Sensitivity characterization with the output of microwave power detector of single pixel as function of incident power, and is sensitive as indicated by dashed red line down to -77 dBm at 2.5 GHz.

The gold curve in Fig. 6.3(b) displays the measured mutual coupling (MC) between neighboring unit cells parallel to the electric field direction. At 2.5 GHz the MC

was measured to be below -14 dB. We have also measured the MC in the perpendicular and diagonal neighboring cells and values below -15 dB were found. Values of MC are significantly low, especially considering the proximity of nearest neighbors at a lattice spacing of $\lambda/4.4$ (27.3 mm) and with edge separation of $\lambda/40$ (3.0 mm). In addition to the clear benefit toward imaging [141-143], reducing MC is of particular importance for multiple input multiple output (MIMO) communication systems that suffer reduction in channel capacity due to these affects [147,148].

We used a separate board to implement the impedance matching circuit and low-noise amplifier (LNA) (Board 2) and another board (Board 3) for the microwave power detector. We connected the output of Port 3 with a UMCC connector to Board 2 as shown schematically in Fig. 6.4. After the signal propagates through the impedance matching network and LNA, it passes through a SMA connector, which we call Port 4. We use the ADL5523 LNA made by Analog Device which provides a gain of approximately 15 dB at 2.5 GHz. In Fig. 6.5, the gold S_{41} curve shows over a 15 dB improvement of S_{31} at 2.5 GHz as a result of having an impedance matching circuit followed by the LNA. The microwave power detector converts the microwave output signal from port 4 into a DC voltage and is implemented using a monolithic LT5534 made by Linear Technology. The LT5534 has a 50MHz to 3GHz detected bandwidth and is capable of measuring microwave signals with over a 60dB dynamic range with a linear DC output with respect to signal amplitude in decibel scale.

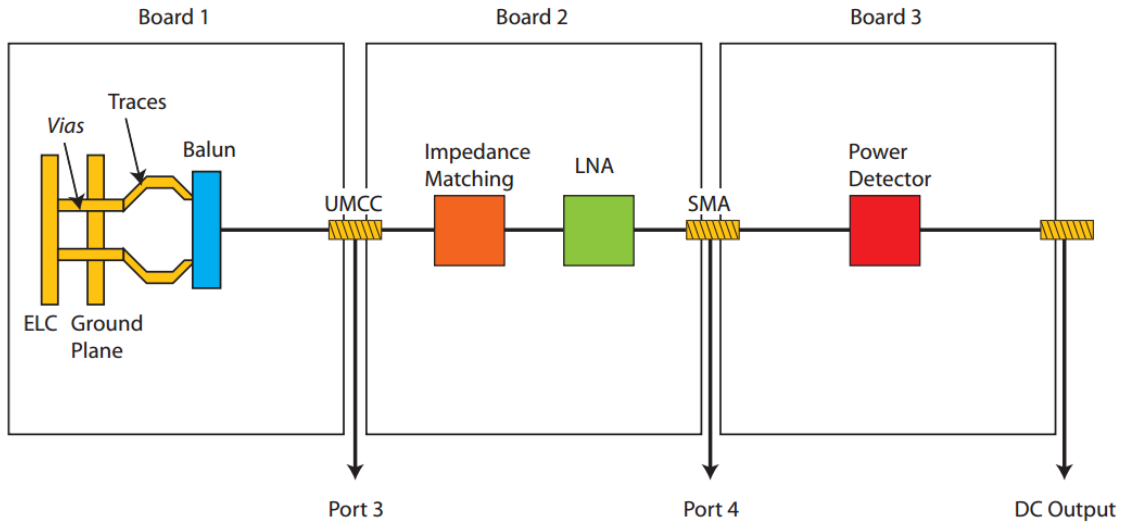


Figure 6.4 System architecture consists of three boards with board 1 which containing the metamaterial connecting through the *vias*, traces and balun out through an ultraminiature coax connector (UMCC) designated as port 3. The UMCC cable connects to board 2 containing both the impedance matching circuit and low noise amplifier (LNA) with output labeled as port 4. The third board consists of only the microwave power detector providing a DC voltage output signal.

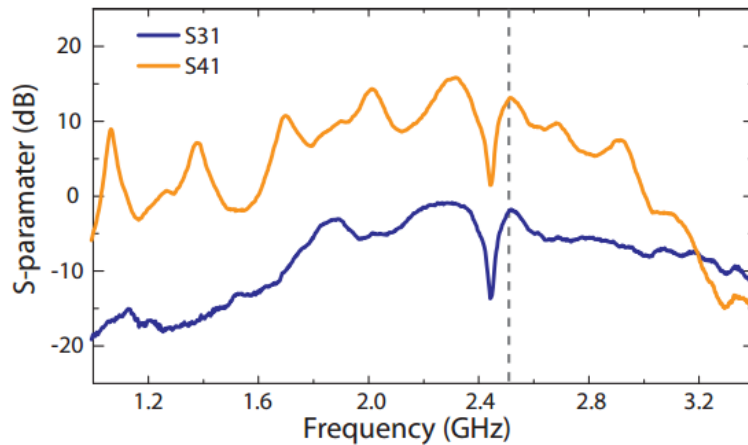


Figure 6.5 S-parameter data shows the transmission without (S₃₁ blue curve) and with (S₄₁ gold curve) the addition of the impedance matching and low noise amplifier (LNA) with the dashed grey line at 2.5 GHz the frequency for sensitivity and off-angle measurements.

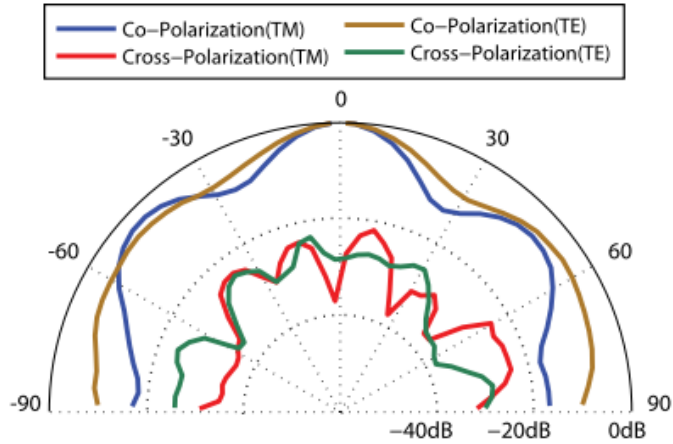


Figure 6.6 Off-angle performance characterization of the MMA / FPA at 2.5 GHz for both the electric field vector perpendicular (TE) and parallel (TM) to the floor of the chamber. The ELC resonator's are rotated between the correct polarization (E-field perpendicular the split gap) and the cross polarization (E-field parallel to the gap).

We now turn toward characterization of the sensitivity and angular dependence of the MMA / FPA. A microwave source was fixed to operate at 2.5 GHz and fed to the horn antenna. The DC voltage output from the MMA / FPA was recorded as the horn power was swept from -50 dBm to +20 dBm as shown in Fig. 6.3(c). We determine an ultimate pixel sensitivity of -77 dBm, corresponding to a radiation power density of 27 nW/m², after calibrating for cable and free space losses. Fig. 6.6 shows the resulting off-angle performance characterization of the MMA / FPA at 2.5 GHz for both transverse electric (TE) and transverse magnetic (TM) polarizations. However it should be noted that our metamaterial does not possess 90° rotational symmetry and thus we characterized TE and TM for both the “correct” polarization -- as shown in Fig. 6.1(a) -- the cross polarization to this. The measurement results demonstrate that the MMA / FPA operates as a wide angle antenna. This is consistent with the off-angle absorption performance typical to MMAs [42]. Both TE and TM cross-polarized angular dependent

measurements are at minimum of 20dB lower than the co-polarized measurements. Thus the presented MMA / FPA may be used for polarization discrimination imaging.

In conclusion, the characterization of our metamaterial absorber focal plane array was demonstrated to operate at 2.5 GHz and have high pixel sensitivity of -77 dBm, with low pixel to pixel coupling interference below -14 dB, good frequency selectivity and wide angular performance. We note that the FPA is not restricted to the frequency applied in this work but could prove useful at higher frequency operation from microwave to millimeter wave. Even more generally, the MMA due to its ability to capture nearly all of the incident electromagnetic energy at design frequencies across the entire electromagnetic spectrum could serve as an excellent candidate to act as detector pixels when implemented into bolometric or semiconducting configurations. The sub-wavelength unit cell and narrow resonant spectral bandwidth can also be expanded to enable multi-color and co- and cross-polarized pixels.

CHAPTER 7

7. Conclusions and future direction

Metamaterials are in the process of changing the landscape for discovery and innovation within a wide scope of applications across the electromagnetic spectrum. The work that is presented here hopes to illuminate several different paths in which this field can be applied and contribute to the development of terahertz (THz) technology. Creating materials and integrating them into actual devices, including spatial light modulators (SLMs) and detector arrays, are areas where an immediate impact can be felt.

We have utilized several different paths to achieve dynamic control of several types of THz metamaterials. We have experimentally demonstrated direct THz modulation at speeds up to 10 MHz using integrated high electron mobility transistors (HEMTs) within the metamaterial unit cell. We have created electronic tunable metamaterial absorbers (MMAs) with an experimental measured modulation depth of 70%. Further we have designed, both through electronic and optical, means to control a THz SLM in order to demonstrate single pixel THz imaging. In addition to the presented work, several related works that are currently being performed are briefly discussed.

7.1. THz compressive sensing

By packing the 8x8 pixel array THz MMA-SLM with a printed circuit board (PCB) which is interconnected to a field programmable gate array (FPGA) with 64 independent programmable channels, we are able to efficiently program spatial masks for multiplex imaging in a reflection based scheme as compared to the transmission scheme presented in Chapter 5, shown schematically in Fig. 7.1(a). This imaging system is capable of

displaying a variety of different masks, which allow for compressive imaging approaches to be demonstrated. Pushing the size of the SLM to higher pixel counts will be necessary to further demonstrate the advantages inherent to these multiplex techniques. In Fig. 7.1(b) a next generation design of a 128x128 pixel THz MMA-SLM is displayed where a read out integrated circuit (ROIC) provides dynamic control of the larger array size.

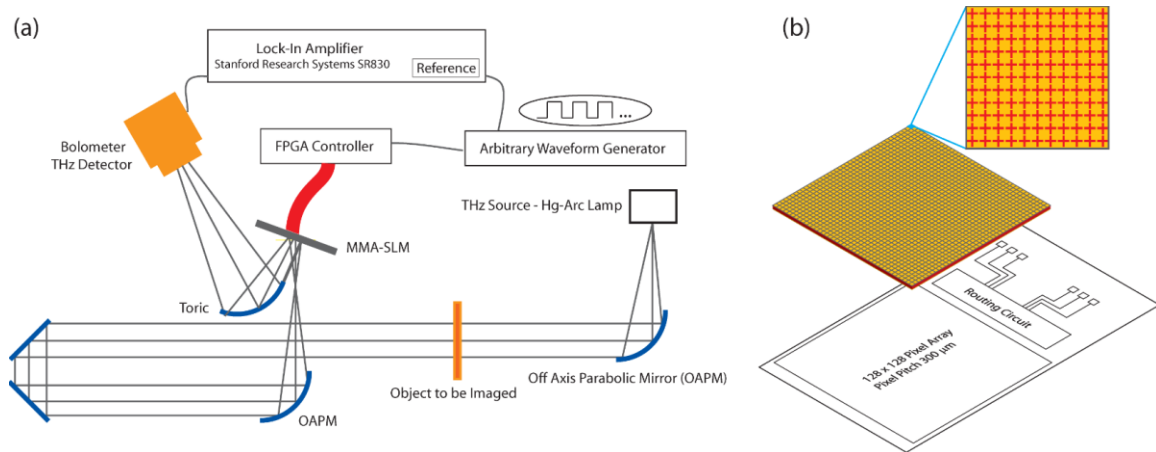


Figure 7.1 Next generation terahertz imaging system utilizing metamaterial spatial light modulator (SLM). (a) Reflection based setup where image formed on metamaterial absorber (MMA) SLM and is spatially multiplexed enabling single pixel detector to be used for THz imaging. (b) Next generation device will allow for high pixel count, with reduced pixel dimensions allowing for nearly 100% filling fraction.

Still necessary are the optimization of several key parameters, for example, moving to a complimentary resonant structure to allow for improved efficiency of the depletion of the doped epitaxial layer and increased tuning in the resonant absorption. Additionally, smaller overall pixel dimensions are possible with higher filling fractions of active metamaterial elements per pixel. Several candidate materials may offer further improvement in the performance as well the complexity and cost required to fabricate these structures. These materials include liquid crystals, ferroelectrics, graphene, HEMTs, and phase change materials such as vanadium oxide.

7.2. Bolometric imaging

Metamaterial absorbers offer several advantages over other types of absorbing media, specifically with regards to the relative thickness of the absorbing structure. Metamaterial absorbers can extinguish the incident radiation over a distance over two orders of magnitude smaller than the wavelength. This could offer potential benefits for the design of detector elements whose performance is hindered by such things as thermal capacitance in bolometric detection and carrier transit length in photodetectors. Commercially available room-temperature THz microbolometer cameras typically rely on scaled versions of their infrared counterparts, with the addition of increased costs and sensitivity thresholds which require high power illumination.

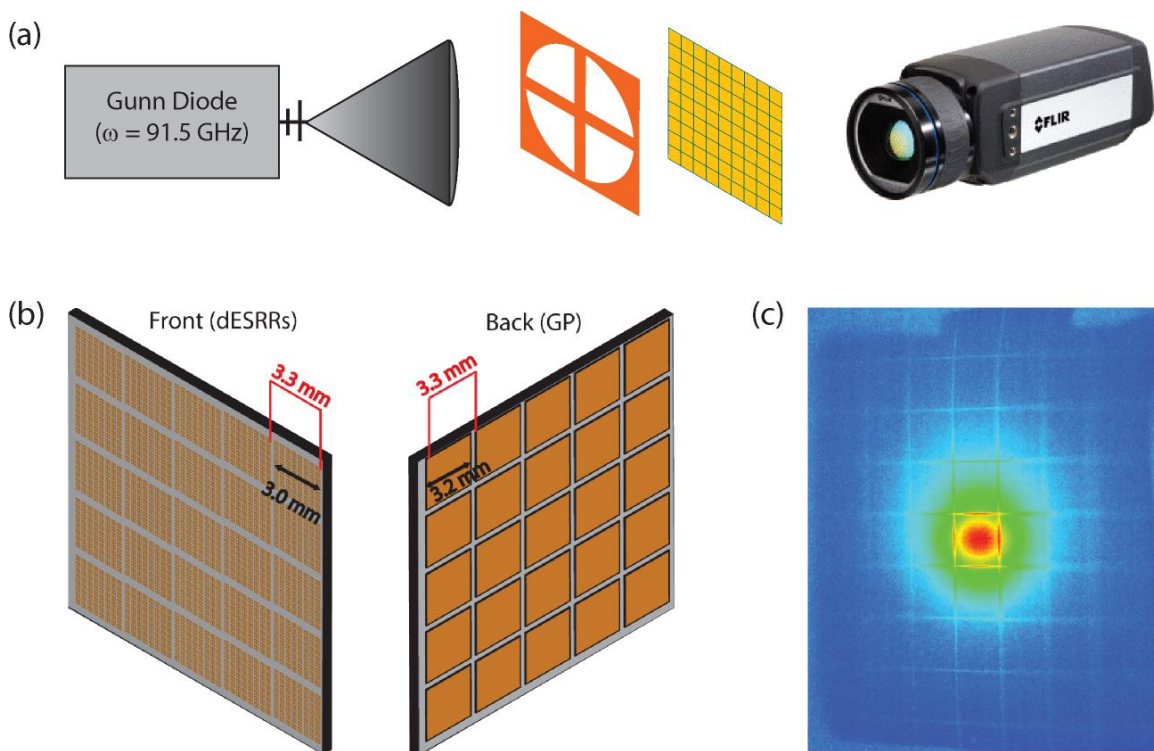


Figure 7.2 Metamaterial absorber (MMA) pixel array used for bolometric mm-wave to infrared (IR) imaging. (a) Schematic of proposed imaging system where mm-wave image is formed on MMA pixel array with a commercial IR camera detecting the thermal

temperature increase formed by the image. (b) Schematic of MMA pixel array. (c) Experimental measured IR image from an incident mm-wave beam.

We are currently studying a bolometric imager using a MMA pixel array to absorb mm-wave radiation. The geometry and material properties are sufficient to increase the effective temperature of the pixels by several degrees which are imaged by a room-temperature forward looking infrared (FLIR) microbolometer camera [See Fig. 7.2(a)]. In Fig. 7.2(b) a schematic of the MMA pixel array features absorber pixels capable of absorbing nearly all of the incident power into pixels where each pixel is on the order of the wavelength and the thickness is close to two orders of magnitude smaller than the wavelength. Preliminary experimental results shown in Fig. 7.2(c) demonstrate the capability to image the thermal signature resulting from incident mm-wave radiation which is roughly focused onto a single pixel of the MMA pixel array. Currently, we are further reducing the pixel pitch, improving thermal isolation to reduce thermal crosstalk, and reducing the total thickness to further reduce the thermal capacitance and increase the sensitivity per pixel.

BIBLIOGRAPHY

1. D. R. Smith, W. J. Padilla, D. Vier, S. C. Nemat-Nasser, and S. Schultz, "Composite medium with simultaneously negative permeability and permittivity," *Physical Review Letters* **84**, 4184-4187 (2000).
2. R. Shelby, D. Smith, and S. Schultz, "Experimental verification of a negative index of refraction," *Science* **292**, 77-79 (2001).
3. D. Schurig, J. Mock, B. Justice, S. A. Cummer, J. Pendry, A. Starr, and D. Smith, "Metamaterial electromagnetic cloak at microwave frequencies," *Science* **314**, 977-980 (2006).
4. J. B. Pendry, "Negative refraction makes a perfect lens," *Physical Review Letters* **85**, 3966-3969 (2000).
5. N. Fang, H. Lee, C. Sun, and X. Zhang, "Sub-diffraction-limited optical imaging with a silver superlens," *Science* **308**, 534-537 (2005).
6. M. Tonouchi, "Cutting-edge terahertz technology," *Nature photonics* **1**, 97-105 (2007).
7. D. Mittleman, M. Gupta, R. Neelamani, R. Baraniuk, J. Rudd, and M. Koch, "Recent advances in terahertz imaging," *Applied Physics B* **68**, 1085-1094 (1999).
8. W. L. Chan, J. Deibel, and D. M. Mittleman, "Imaging with terahertz radiation," *Reports on Progress in Physics* **70**, 1325 (2007).
9. T. Korter and D. Plusquellic, "Continuous-wave terahertz spectroscopy of biotin: vibrational anharmonicity in the far-infrared," *Chemical Physics Letters* **385**, 45-51 (2004).
10. N. Karpowicz, H. Zhong, C. Zhang, K. I. Lin, J. S. Hwang, J. Xu, and X. C. Zhang, "Compact continuous-wave subterahertz system for inspection applications," *Applied Physics Letters* **86**, 054105-054105-3 (2005).
11. K. Kawase, Y. Ogawa, Y. Watanabe, and H. Inoue, "Non-destructive terahertz imaging of illicit drugs using spectral fingerprints," *Optics Express* **11**, 2549-2554 (2003).
12. G. P. Williams, "Filling the THz gap—high power sources and applications," *Reports on Progress in Physics* **69**, 301 (2006).
13. S. A. Cummer and D. Schurig, "One path to acoustic cloaking," *New Journal of Physics* **9**, 45 (2007).

14. S. Narayana and Y. Sato, "Heat flux manipulation with engineered thermal materials," *Physical Review Letters* **108**, 214303 (2012).
15. J. B. Pendry, A. Holden, D. Robbins, and W. Stewart, "Magnetism from conductors and enhanced nonlinear phenomena," *IEEE Transactions on Microwave Theory and Techniques* **47**, 2075-2084 (1999).
16. D. Smith, S. Schultz, P. Markoš, and C. Soukoulis, "Determination of effective permittivity and permeability of metamaterials from reflection and transmission coefficients," *Physical Review B* **65**, 195104 (2002).
17. D. R. Smith and J. B. Pendry, "Homogenization of metamaterials by field averaging," *JOSA B* **23**, 391-403 (2006).
18. D. Smith, "Analytic expressions for the constitutive parameters of magnetoelectric metamaterials," *Physical Review E* **81**, 036605 (2010).
19. F. Capolino, *Theory and phenomena of metamaterials* (CRC Press LLC Boca Raton, FL, 2009).
20. J. Pendry, A. Holden, W. Stewart, and I. Youngs, "Extremely low frequency plasmons in metallic mesostructures," *Physical Review Letters* **76**, 4773-4776 (1996).
21. S. O'Brien and J. Pendry, "Magnetic activity at infrared frequencies in structured metallic photonic crystals," *Journal of Physics: Condensed Matter* **14**, 6383 (2002).
22. C. Caloz and T. Itoh, *Electromagnetic metamaterials: transmission line theory and microwave applications* (Wiley-IEEE Press New York, 2005).
23. D. Schurig, J. Mock, and D. Smith, "Electric-field-coupled resonators for negative permittivity metamaterials," *Applied Physics Letters* **88**, 041109-041109-3 (2006).
24. W. Padilla, M. Aronsson, C. Highstrete, M. Lee, A. Taylor, and R. Averitt, "Electrically resonant terahertz metamaterials: Theoretical and experimental investigations," *Physical Review B* **75**, 041102 (2007).
25. R. Liu, T. J. Cui, D. Huang, B. Zhao, and D. R. Smith, "Description and explanation of electromagnetic behaviors in artificial metamaterials based on effective medium theory," *Physical Review E* **76**, 026606 (2007).
26. N. Landy, C. Bingham, T. Tyler, N. Jokerst, D. Smith, and W. Padilla, "Design, theory, and measurement of a polarization-insensitive absorber for terahertz imaging," *Physical Review B* **79**, 125104 (2009).

27. A. Schwanecke, A. Krasavin, D. Bagnall, A. Potts, A. Zayats, and N. Zheludev, "Broken time reversal of light interaction with planar chiral nanostructures," *Physical Review Letters* **91**, 247404 (2003).
28. J. Pendry, "A chiral route to negative refraction," *Science* **306**, 1353-1355 (2004).
29. W. Chen, C. M. Bingham, K. M. Mak, N. W. Caira, and W. J. Padilla, "Extremely subwavelength planar magnetic metamaterials," *Physical Review B* **85**, 201104 (2012).
30. C. M. Bingham, H. Tao, X. Liu, R. D. Averitt, X. Zhang, and W. J. Padilla, "Planar wallpaper group metamaterials for novel terahertz applications," *Optics Express* **16**, 18565-18575 (2008).
31. N. Han, Z. Chen, C. Lim, B. Ng, and M. Hong, "Broadband multi-layer terahertz metamaterials fabrication and characterization on flexible substrates," *Optics Express* **19**, 6990-6998 (2011).
32. F. Falcone, T. Lopetegi, M. Laso, J. Baena, J. Bonache, M. Beruete, R. Marqués, F. Martin, and M. Sorolla, "Babinet principle applied to the design of metasurfaces and metamaterials," *Physical Review Letters* **93**, 197401 (2004).
33. H. Chen, J. F. O'Hara, A. J. Taylor, R. D. Averitt, C. Highstrete, M. Lee, and W. J. Padilla, "Complementary planar terahertz metamaterials," *Optics Express* **15**, 1084-1095 (2007).
34. N. Landy, S. Sajuyigbe, J. Mock, D. Smith, and W. Padilla, "Perfect metamaterial absorber," *Physical Review Letters* **100**, 207402 (2008).
35. C. M. Watts, X. Liu, and W. J. Padilla, "Metamaterial Electromagnetic Wave Absorbers," *Advanced Materials* **24**, 98-120 (2012).
36. X. Liu, T. Tyler, T. Starr, A. F. Starr, N. M. Jokerst, and W. J. Padilla, "Taming the blackbody with infrared metamaterials as selective thermal emitters," *Physical Review Letters* **107**, 45901 (2011).
37. K. Aydin, V. E. Ferry, R. M. Briggs, and H. A. Atwater, "Broadband polarization-independent resonant light absorption using ultrathin plasmonic super absorbers," *Nature Communications* **2**, 517 (2011).
38. X. Liu, T. Starr, A. F. Starr, and W. J. Padilla, "Infrared spatial and frequency selective metamaterial with near-unity absorbance," *Physical Review Letters* **104**, 207403 (2010).
39. H. Tao, N. I. Landy, C. M. Bingham, X. Zhang, R. D. Averitt, and W. J. Padilla, "A metamaterial absorber for the terahertz regime: Design, fabrication and characterization," *Optics express* **16**, 7181-7188 (2008).

40. J. Hao, J. Wang, X. Liu, W. J. Padilla, L. Zhou, and M. Qiu, "High performance optical absorber based on a plasmonic metamaterial," *Applied Physics Letters* **96**, 251104-251104-3 (2010).
41. W. Padilla and X. Liu, "Perfect electromagnetic absorbers from microwave to optical," *SPIE Newsroom Optical Design & Engineering* **10**, 003137 (2010).
42. H. Tao, C. Bingham, A. Strikwerda, D. Pilon, D. Shrekenhamer, N. Landy, K. Fan, X. Zhang, W. Padilla, and R. Averitt, "Highly flexible wide angle of incidence terahertz metamaterial absorber: Design, fabrication, and characterization," *Physical Review B* **78**, 241103 (2008).
43. H. Tao, C. Bingham, D. Pilon, K. Fan, A. Strikwerda, D. Shrekenhamer, W. Padilla, X. Zhang, and R. Averitt, "A dual band terahertz metamaterial absorber," *Journal of Physics D: Applied Physics* **43**, 225102 (2010).
44. D. Shrekenhamer, W. Chen, and W. J. Padilla, "Liquid Crystal Tunable Metamaterial Perfect Absorber," arXiv preprint arXiv:1206.4214 (2012).
45. D. Shrekenhamer, C. M. Watts, J. Montoya, S. Krishna, and W. J. Padilla, "Metamaterial-based imaging for potential security applications" in *SPIE OPTO*(International Society for Optics and Photonics, 2013).
46. T. Yen, W. Padilla, N. Fang, D. Vier, D. Smith, J. Pendry, D. Basov, and X. Zhang, "Terahertz magnetic response from artificial materials," *Science* **303**, 1494-1496 (2004).
47. J. F. Federici, B. Schulkin, F. Huang, D. Gary, R. Barat, F. Oliveira, and D. Zimdars, "THz imaging and sensing for security applications—explosives, weapons and drugs," *Semiconductor Science and Technology* **20**, S266 (2005).
48. G. J. Simonis, "Index to the literature dealing with the near-millimeter wave properties of materials," *International Journal of Infrared and Millimeter Waves* **3**, 439-469 (1982).
49. J. W. Lamb, "Miscellaneous data on materials for millimetre and submillimetre optics," *International Journal of Infrared and Millimeter Waves* **17**, 1997-2034 (1996).
50. R. Piesiewicz, C. Jansen, S. Wietzke, D. Mittleman, M. Koch, and T. Kürner, "Properties of building and plastic materials in the THz range," *International Journal of Infrared and Millimeter Waves* **28**, 363-371 (2007).
51. X. Peralta, M. Wanke, C. Arrington, J. Williams, I. Brener, A. Strikwerda, R. Averitt, W. Padilla, E. Smirnova, and A. Taylor, "Large-area metamaterials on thin membranes for multilayer and curved applications at terahertz and higher frequencies," *Applied Physics Letters* **94**, 161113 (2009).

52. H. Tao, A. Strikwerda, K. Fan, C. Bingham, W. Padilla, X. Zhang, and R. Averitt, "Terahertz metamaterials on free-standing highly-flexible polyimide substrates," *J.Phys.D: Appl.Phys* **41**, 232004 (2008).
53. X. Liu, S. MacNaughton, D. B. Shrekenhamer, H. Tao, S. Selvarasah, A. Totachawattana, R. D. Averitt, M. R. Dokmeci, S. Sonkusale, and W. J. Padilla, "Metamaterials on parylene thin film substrates: Design, fabrication, and characterization at terahertz frequency," *Applied Physics Letters* **96**, 011906-011906-3 (2010).
54. H. Tao, J. J. Amsden, A. C. Strikwerda, K. Fan, D. L. Kaplan, X. Zhang, R. D. Averitt, and F. G. Omenetto, "Metamaterial silk composites at terahertz frequencies," *Advanced Materials* **22**, 3527-3531 (2010).
55. V. Yannopapas and A. Moroz, "Negative refractive index metamaterials from inherently non-magnetic materials for deep infrared to terahertz frequency ranges," *Journal of physics: Condensed matter* **17**, 3717 (2005).
56. O. Paul, C. Imhof, B. Reinhard, R. Zengerle, and R. Beigang, "Negative index bulk metamaterial at terahertz frequencies," *Opt.Express* **16**, 6736-6744 (2008).
57. S. Zhang, Y. Park, J. Li, X. Lu, W. Zhang, and X. Zhang, "Negative refractive index in chiral metamaterials," *Physical Review Letters* **102**, 023901 (2009).
58. W. Chen, N. Landy, K. Kempa, and W. Padilla, "A Subwavelength Extraordinary-Optical-Transmission Channel in Babinet Metamaterials," *Advanced Optical Materials* (2013).
59. W. J. Padilla, A. J. Taylor, C. Highstrete, M. Lee, and R. D. Averitt, "Dynamical electric and magnetic metamaterial response at terahertz frequencies," *Physical Review Letters* **96**, 107401 (2006).
60. H. T. Chen, J. F. O'Hara, A. K. Azad, A. J. Taylor, R. D. Averitt, D. B. Shrekenhamer, and W. J. Padilla, "Experimental demonstration of frequency-agile terahertz metamaterials," *Nature Photonics* **2**, 295-298 (2008).
61. H. T. Chen, W. J. Padilla, J. M. O. Zide, A. C. Gossard, A. J. Taylor, and R. D. Averitt, "Active terahertz metamaterial devices," *Nature* **444**, 597-600 (2006).
62. H. T. Chen, S. Palit, T. Tyler, C. M. Bingham, J. M. O. Zide, J. F. OHara, D. R. Smith, A. C. Gossard, R. D. Averitt, and W. J. Padilla, "Hybrid metamaterials enable fast electrical modulation of freely propagating terahertz waves," *Applied Physics Letters* **93**, 091117-091117-3 (2008).
63. D. Shrekenhamer, S. Rout, A. C. Strikwerda, C. Bingham, R. D. Averitt, S. Sonkusale, and W. J. Padilla, "High speed terahertz modulation from metamaterials with embedded high electron mobility transistors," *Optics Express* **19**, 9968-9975 (2011).

64. T. Driscoll, S. Palit, M. M. Qazilbash, M. Brehm, F. Keilmann, B. G. Chae, S. J. Yun, H. T. Kim, S. Cho, and N. M. Jokerst, "Dynamic tuning of an infrared hybrid-metamaterial resonance using vanadium dioxide," *Applied Physics Letters* **93**, 024101-024101-3 (2008).
65. H. Tao, A. Strikwerda, K. Fan, W. Padilla, X. Zhang, and R. Averitt, "Reconfigurable terahertz metamaterials," *Physical Review Letters* **103**, 147401 (2009).
66. H. Chen, W. J. Padilla, M. J. Cich, A. K. Azad, R. D. Averitt, and A. J. Taylor, "A metamaterial solid-state terahertz phase modulator," *Nature Photonics* **3**, 148-151 (2009).
67. W. M. Zhu, A. Q. Liu, X. M. Zhang, D. P. Tsai, T. Bourouina, J. H. Teng, X. H. Zhang, H. C. Guo, H. Tanoto, and T. Mei, "Switchable magnetic metamaterials using micromachining processes," *Advanced Materials* **23**, 1792-1796 (2011).
68. A. Taflove and S. C. Hagness, *Computational Electrodynamics: The Finite Difference Time Domain Method* (Artech House Boston, MA, 2000).
69. J. Jin, *The finite element method in electromagnetics* (Wiley New York, 2002).
70. D. Smith, D. Vier, T. Koschny, and C. Soukoulis, "Electromagnetic parameter retrieval from inhomogeneous metamaterials," *Physical Review E* **71**, 036617 (2005).
71. R. Singh, E. Smirnova, A. J. Taylor, J. F. O'Hara, and W. Zhang, "Optically thin terahertz metamaterials," *Opt. Express* **16**, 6537-6543 (2008).
72. M. Van Exter and D. R. Grischkowsky, "Characterization of an optoelectronic terahertz beam system," *Microwave Theory and Techniques, IEEE Transactions on* **38**, 1684-1691 (1990).
73. S. L. Dexheimer, *Terahertz spectroscopy: principles and applications* (CRC press London, 2007).
74. P. U. Jepsen, R. Jacobsen, and S. Keiding, "Generation and detection of terahertz pulses from biased semiconductor antennas," *JOSA B* **13**, 2424-2436 (1996).
75. J. F. O'Hara, J. Zide, A. Gossard, A. Taylor, and R. Averitt, "Enhanced terahertz detection via ErAs: GaAs nanoisland superlattices," *Applied Physics Letters* **88**, 251119-251119-3 (2006).
76. A. A. Michelson, "XXXVIII. On the application of interference-methods to spectroscopic measurements.—I," *The London, Edinburgh, and Dublin Philosophical Magazine and Journal of Science* **31**, 338-346 (1891).
77. P. Griffiths and J. A. De Haseth, *Fourier transform infrared spectrometry* (Wiley-Interscience New York, 2007).

78. W. Knap, J. Lusakowski, T. Parenty, S. Bollaert, A. Cappy, V. Popov, and M. Shur, "Terahertz emission by plasma waves in 60 nm gate high electron mobility transistors," *Applied Physics Letters* **84**, 2331-2333 (2004).
79. W. Knap, Y. Deng, S. Rumyantsev, and M. Shur, "Resonant detection of subterahertz and terahertz radiation by plasma waves in submicron field-effect transistors," *Applied Physics Letters* **81**, 4637-4639 (2002).
80. T. Kleine-Ostmann, P. Dawson, K. Pierz, G. Hein, and M. Koch, "Room-temperature operation of an electrically driven terahertz modulator," *Applied Physics Letters* **84**, 3555-3557 (2004).
81. M. Dyakonov and M. Shur, "Shallow water analogy for a ballistic field effect transistor: New mechanism of plasma wave generation by dc current," *Physical Review Letters* **71**, 2465-2468 (1993).
82. M. Dyakonov and M. Shur, "Detection, mixing, and frequency multiplication of terahertz radiation by two-dimensional electronic fluid," *IEEE Transactions on Electron Devices* **43**, 380-387 (1996).
83. C. Y. Chen, T. R. Tsai, C. L. Pan, and R. P. Pan, "Room temperature terahertz phase shifter based on magnetically controlled birefringence in liquid crystals," *Applied Physics Letters* **83**, 4497-4499 (2003).
84. T. R. Tsai, C. Y. Chen, R. P. Pan, C. L. Pan, and X. C. Zhang, "Electrically controlled room temperature terahertz phase shifter with liquid crystal," *IEEE Microwave and Wireless Components Letters* **14**, 77-79 (2004).
85. T. Kleine-Ostmann, K. Pierz, G. Hein, P. Dawson, M. Marso, and M. Koch, "Spatially resolved measurements of depletion properties of large gate two-dimensional electron gas semiconductor terahertz modulators," *Journal of Applied Physics* **105**, 093707-093707-6 (2009).
86. P. Chao, M. Shur, R. Tiberio, K. G. Duh, P. Smith, J. Ballingall, P. Ho, and A. Jabra, "DC and microwave characteristics of sub-0.1- μm gate-length planar-doped pseudomorphic HEMTs," *IEEE Transactions on Electron Devices* **36**, 461-473 (1989).
87. Y. Cai, I. Brener, J. Lopata, J. Wynn, L. Pfeiffer, J. Stark, Q. Wu, X. Zhang, and J. Federici, "Coherent terahertz radiation detection: Direct comparison between free-space electro-optic sampling and antenna detection," *Applied Physics Letters* **73**, 444-446 (1998).
88. S. Allen Jr, D. Tsui, and F. DeRosa, "Frequency dependence of the electron conductivity in the silicon inversion layer in the metallic and localized regimes," *Physical Review Letters* **35**, 1359-1362 (1975).

89. E. Batke and D. Heitmann, "Rapid-Scan fourier transform spectroscopy of 2-D space charge layers in semiconductors," *Infrared Physics* **24**, 189-197 (1984).
90. R. Plana, L. Escotte, O. Llopi, H. Amine, T. Parra, M. Gayral, and J. Graffeuil, "Noise in AlGaAs/InGaAs/GaAs pseudomorphic HEMTs from 10 Hz to 18 GHz," *IEEE Transactions on Electron Devices* **40**, 852-858 (1993).
91. R. Wilk, N. Vieweg, O. Kopschinski, and M. Koch, "Liquid crystal based electrically switchable Bragg structure for THz waves," *Optics Express* **17**, 7377-7382 (2009).
92. I. Khoo, D. Werner, X. Liang, A. Diaz, and B. Weiner, "Nanosphere dispersed liquid crystals for tunable negative-zero-positive index of refraction in the optical and terahertz regimes," *Optics Letters* **31**, 2592-2594 (2006).
93. W. Hu, R. Dickie, R. Cahill, H. Gamble, Y. Ismail, V. Fusco, D. Linton, N. Grant, and S. Rea, "Liquid crystal tunable mm wave frequency selective surface," *Microwave and Wireless Components Letters, IEEE* **17**, 667-669 (2007).
94. M. Gorkunov and M. Osipov, "Tunability of wire-grid metamaterial immersed into nematic liquid crystal," *Journal of Applied Physics* **103**, 036101-036101-3 (2008).
95. A. Minovich, J. Farnell, D. N. Neshev, I. McKerracher, F. Karouta, J. Tian, D. A. Powell, I. V. Shadrivov, H. Hoe Tan, and C. Jagadish, "Liquid crystal based nonlinear fishnet metamaterials," *Applied Physics Letters* **100**, 121113-121113-4 (2012).
96. T. Tsai, C. Chen, C. Pan, R. Pan, and X. Zhang, "Terahertz time-domain spectroscopy studies of the optical constants of the nematic liquid crystal 5CB," *Applied Optics* **42**, 2372-2376 (2003).
97. R. Wilk, N. Vieweg, O. Kopschinski, T. Hasek, and M. Koch, "THz Spectroscopy of Liquid Crystals from the CB Family," *Journal of Infrared, Millimeter and Terahertz Waves* **30**, 1139-1147 (2009).
98. N. Vieweg, C. Jansen, M. K. Shakfa, M. Scheller, N. Krumbholz, R. Wilk, M. Mikulics, and M. Koch, "Molecular properties of liquid crystals in the terahertz frequency range," *Optics express* **18**, 6097-6107 (2010).
99. P. J. Collings and M. Hird, *Introduction to liquid crystals: chemistry and physics* (Taylor & Francis London, 2004).
100. G. Meier and A. Saupe, "Dielectric relaxation in nematic liquid crystals," *Molecular Crystals and Liquid Crystals* **1**, 515-525 (1966).
101. W. H. Dejeu, *Liquid Crystals* (Academic Press New York, 1978).

102. F. Rutz, T. Hasek, M. Koch, H. Richter, and U. Ewert, "Terahertz birefringence of liquid crystal polymers," *Applied Physics Letters* **89**, 221911-221911-3 (2006).
103. H. Mosallaei and K. Sarabandi, "Design and modeling of patch antenna printed on magneto-dielectric embedded-circuit metasubstrate," *Antennas and Propagation, IEEE Transactions on* **55**, 45-52 (2007).
104. S. J. Lee, Z. Ku, A. Barve, J. Montoya, W. Y. Jang, S. Brueck, M. Sundaram, A. Reisinger, S. Krishna, and S. K. Noh, "A monolithically integrated plasmonic infrared quantum dot camera," *Nature Communications* **2**, 286 (2011).
105. Y. Urzhumov, J. S. Lee, T. Tyler, S. Dhar, V. Nguyen, N. M. Jokerst, P. Schmalenberg, and D. R. Smith, "Electronically reconfigurable metal-on-silicon metamaterial," *Physical Review B* **86**, 075112 (2012).
106. T. I. Jeon and D. Grischkowsky, "Characterization of optically dense, doped semiconductors by reflection THz time domain spectroscopy," *Applied Physics Letters* **72**, 3032-3034 (1998).
107. P. Huggard, J. Cluff, G. Moore, C. Shaw, S. Andrews, S. Keiding, E. Linfield, and D. Ritchie, "Drude conductivity of highly doped GaAs at terahertz frequencies," *Journal of Applied Physics* **87**, 2382-2385 (2000).
108. S. M. Sze and K. K. Ng, *Physics of semiconductor devices* (WileyNew York, 1981).
109. M. Shur, *Introduction to electronic devices* (WileyNew York, 1996).
110. B. Baliga, R. Ehle, J. Shealy, and W. Garwacki, "Breakdown characteristics of gallium arsenide," *IEEE Electron Device Letters* **2**, 302-304 (1981).
111. M. Hudait and S. Krupanidhi, "Breakdown characteristics of MOVPE grown Si-doped GaAs Schottky diodes," *Solid-State Electronics* **43**, 2135-2139 (1999).
112. A. W. Lee and Q. Hu, "Real-time, continuous-wave terahertz imaging by use of a microbolometer focal-plane array," *Optics Letters* **30**, 2563-2565 (2005).
113. N. R. Butler, R. J. Blackwell, R. Murphy, R. J. Silva, and C. A. Marshall, "Low-cost uncooled microbolometer imaging system for dual use" in *SPIE's 1995 International Symposium on Optical Science, Engineering, and Instrumentation* (International Society for Optics and Photonics, 1995).
114. Q. Wu, T. Hewitt, and X. Zhang, "Two-dimensional electro-optic imaging of THz beams," *Applied Physics Letters* **69**, 1026-1028 (1996).
115. B. Hu and M. Nuss, "Imaging with terahertz waves," *Optics Letters* **20**, 1716-1718 (1995).

116. M. C. Nuss, "Chemistry is right for T-ray imaging," *IEEE Circuits and Devices Magazine* **12**, 25-30 (1996).
117. W. L. Chan, K. Charan, D. Takhar, K. F. Kelly, R. G. Baraniuk, and D. M. Mittleman, "A single-pixel terahertz imaging system based on compressed sensing," *Applied Physics Letters* **93**, 121105-121105-3 (2008).
118. O. Furxhi, E. L. Jacobs, and C. Preza, "Image plane coded aperture for terahertz imaging," *Optical Engineering* **51**, 091612-1-091612-8 (2012).
119. H. Shen, L. Gan, N. Newman, Y. Dong, C. Li, Y. Huang, and Y. Shen, "Spinning disk for compressive imaging," *Optics Letters* **37**, 46-48 (2012).
120. D. Dudley, W. Duncan, and J. Slaughter, "Emerging digital micromirror device (DMD) applications" in *Proc. SPIE*, 2003).
121. K. M. Johnson, D. J. McKnight, and I. Underwood, "Smart spatial light modulators using liquid crystals on silicon," *IEEE Journal of Quantum Electronics* **29**, 699-714 (1993).
122. G. W. Webb, W. Vernon, M. Sanchez, S. Rose, and S. Angello, "Optically controlled millimeter wave antenna" in *Microwave Photonics, 1999. MWP'99. International Topical Meeting on*(IEEE, 1999).
123. M. R. Chaharmir, J. Shaker, M. Cuhaci, and A. Sebak, "Novel photonicly-controlled reflectarray antenna," *IEEE Transactions on Antennas and Propagation* **54**, 1134-1141 (2006).
124. X. C. Zhang and D. Auston, "Generation of steerable submillimeter waves from semiconductor surfaces by spatial light modulators," *Applied Physics Letters* **59**, 768-770 (1991).
125. T. Okada and K. Tanaka, "Photo-designed terahertz devices," *Scientific reports* **1**, (2011).
126. S. Busch, B. Scherger, M. Scheller, and M. Koch, "Optically controlled terahertz beam steering and imaging," *Optics Letters* **37**, 1391-1393 (2012).
127. M. Harwit and N. J. A. Sloane, *Hadamard transform optics* (Academic Press New York, 1979).
128. E. W. Cheney and D. R. Kincaid, *Numerical mathematics and computing* (Thompson Brooks/Cole Belmont, 2008).
129. R. H. Bube, *Photoelectronic properties of semiconductors* (Cambridge University Press Cambridge, 1992).

130. D. Cooke and P. U. Jepsen, "Optical modulation of terahertz pulses in a parallel plate waveguide," *Optics express* **16**, 15123-15129 (2008).
131. M. Van Exter and D. Grischkowsky, "Optical and electronic properties of doped silicon from 0.1 to 2 THz," *Applied Physics Letters* **56**, 1694-1696 (1990).
132. H. Alius and G. Dodel, "Amplitude-, phase-, and frequency modulation of far-infrared radiation by optical excitation of silicon," *Infrared physics* **32**, 1-11 (1991).
133. T. Jeon and D. Grischkowsky, "Nature of conduction in doped silicon," *Physical Review Letters* **78**, 1106-1109 (1997).
134. H. Schulenburg and H. Tributsch, "Electropassivation of silicon and bulk lifetime determination with dry polymer contact," *Journal of Physics D: Applied Physics* **33**, 851 (2000).
135. C. Hutley, *Diffraction gratings* (Academic Press, 1982).
136. J. P. Rice, J. E. Neira, M. Kehoe, and R. Swanson, "DMD diffraction measurements to support design of projectors for test and evaluation of multispectral and hyperspectral imaging sensors" in *SPIE MOEMS-MEMS: Micro-and Nanofabrication* (International Society for Optics and Photonics, 2009).
137. R. A. DeVerse, R. R. Coifman, A. C. Coppi, W. G. Fateley, F. Geshwind, R. M. Hammaker, S. Valenti, F. J. Warner, and G. L. Davis, "Application of spatial light modulators for new modalities in spectrometry and imaging" in *Biomedical Optics 2003* (International Society for Optics and Photonics, 2003).
138. <http://www.skatelescope.org>.
139. C. Carilli and S. Rawlings, "Science with the square kilometre array," *New astronomy reviews* **48**, (2004).
140. R. Appleby and R. N. Anderton, "Millimeter-wave and submillimeter-wave imaging for security and surveillance," *Proceedings of the IEEE* **95**, 1683-1690 (2007).
141. J. P. Weem and Z. Popovic, "A method for determining noise coupling in a phased array antenna" in *2001 IEEE MTT-S International Microwave Symposium Digest* (IEEE, 2001).
142. C. Craeye, B. Parvais, and X. Dardenne, "MoM simulation of signal-to-noise patterns in infinite and finite receiving antenna arrays," *IEEE Transactions on Antennas and Propagation* **52**, 3245-3256 (2004).

143. K. F. Warnick and M. A. Jensen, "Effects of mutual coupling on interference mitigation with a focal plane array," *IEEE Transactions on Antennas and Propagation* **53**, 2490-2498 (2005).
144. M. V. Ivashina, M. Kehn, P. Kildal, and R. Maaskant, "Control of reflection and mutual coupling losses in maximizing efficiency of dense focal plane arrays" in *First European Conference on Antennas and Propagation (EuCAP)*(IEEE, 2006).
145. M. Ng Mou Kehn, M. V. Ivashina, P. Kildal, and R. Maaskant, "Definition of unifying decoupling efficiency of different array antennas—Case study of dense focal plane array feed for parabolic reflector," *AEU-International Journal of Electronics and Communications* **64**, 403-412 (2010).
146. D. Shrekenhamer, W. Xu, S. Venkatesh, D. Schurig, S. Sonkusale, and W. J. Padilla, "Experimental Realization of a Metamaterial Detector Focal Plane Array," *Physical Review Letters* **109**, 177401 (2012).
147. M. A. Jensen and J. W. Wallace, "A review of antennas and propagation for MIMO wireless communications," *IEEE Transactions on Antennas and Propagation* **52**, 2810-2824 (2004).
148. C. Chiu, C. Cheng, R. D. Murch, and C. R. Rowell, "Reduction of mutual coupling between closely-packed antenna elements," *IEEE Transactions on Antennas and Propagation* **55**, 1732-1738 (2007).

CURRICULUM VITAE

David B. Shrekenhamer

shrekenh@bc.edu

Education

- Boston College, Chestnut Hill, MA
PhD in Physics Expected June 2013
Thesis Title: Dynamic Control of Metamaterials at Terahertz Frequencies
Advisor: Willie J. Padilla
- University of California, San Diego, La Jolla, CA
BS in Physics, 2006

Relevant Experience

Doctoral Research Fellow 2007 to Present

Department of Physics, Boston College

- Designed, fabricated, and characterized THz metamaterial devices (ferroelectric, HEMT, n-doped, photoexcitation, phase-change).
- Designed, integrated, and demonstrated imaging sensor concepts utilizing metamaterials as key elements (Microwave FPA, THz compressive sensing, IR coded apertures, THz rectification, and MMW to IR bolometric conversion).
- Developed a wide variety of optical spectroscopy techniques and instrument modifications for advanced experiments (Fourier-transform infrared spectrometer (FTIR), ultrafast lasers (THz-TDS), hyper-spectral microscopy, low-temperature vacuum optical designs).

Undergraduate Research Fellow 2004 to 2006

Department of Physics, University of California, San Diego

- Low temperature optical spectroscopy studies of dilute magnetic semiconductors (GaMnAs), and phase change materials (GeSbTe and VO).

Undergraduate Research Fellow 2004 to 2005

Department of Mathematics and Computer Science, University of California, San Diego

- Random Graph Theory, Poisson and Fourier analysis to characterize the network of communication network existing through wireless PDA software.

Engineering Internship 2003

Northrop Grumman Electronic Systems, Azusa, CA

- Supported the preliminary system architecture definition for Space Based Infrared System (SBIRS).

Scientific Journal Publications:

1. **D. Shrekenhamer**, S. Rout, A. C. Strikwerda, C. M. Bingham, R. D. Averitt, S. Sonkusale, and W. J. Padilla, "High speed terahertz modulation from metamaterials with embedded high electron mobility transistors," *Opt. Express* **19**, 9968-9975 (2011).
2. **D. Shrekenhamer**, W. Xu, S. Venkatesh, D. Schurig, S. Sonkusale, and W.J. Padilla, "Experimental realization of a metamaterial detector focal plane array," *Phys. Rev. Lett.* **109**, 177401 (2012).
3. **D. Shrekenhamer**, W. –C. Chen, W. J. Padilla, "Liquid crystal tunable metamaterial absorber," *Phys. Rev. Lett.* **110**, 177403 (2013).
4. **D. Shrekenhamer**, C. M. Watts, and W. J. Padilla, "Terahertz single pixel imaging with an optically controlled dynamic spatial light modulator," *Opt. Express* **21**, 12507-12518 (2013).
5. **D. Shrekenhamer**, J. Montoya, S. Krishna and W. J. Padilla, "Four-color Metamaterial THz Spatial Light Modulator," In review at *Nat. Mater.*
6. **D. Shrekenhamer**, C. M. Watts, J. Montoya, S. Krishna and W. J. Padilla, "Metamaterial-based Imaging for Potential Security Applications," *Proc. SPIE* **8632**, 863221 (2013).
7. **D. Shrekenhamer**, C. M. Watts and W. J. Padilla, "Terahertz Multiplex Imaging with Reconfigurable Metamaterial Masks," *SPIE Newsroom* (2013).
8. H. T. Chen, J. F. O'Hara, A. K. Azad, A. J. Taylor, R. D. Averitt, **D. B. Shrekenhamer**, and W. J. Padilla, "Experimental demonstration of frequency-agile terahertz metamaterials," *Nat. Photon.* **2**, 295-298 (2008).
9. K. S. Burch, **D. B. Shrekenhamer**, E. J. Singley, J. Stephens, B. L. Sheu, R. K. Kawakami, P. Schiffer, N. Samarth, D. D. Awschalom, and D. N. Basov, "Impurity band conduction in a high temperature ferromagnetic semiconductor," *Phys. Rev. Lett.* **97**, 087208 (2006).
10. X. Liu, S. MacNaughton, **D. B. Shrekenhamer**, H. Tao, R. D. Averitt, M. R. Dokmeci, S. Sonkusale, and W. J. Padilla, "Metamaterials on parylene thin film substrates: Design, fabrication and characterization at THz frequencies ", *Appl. Phys. Lett.* **96**, 011906 (2010).
11. H. Tao, C. M. Bingham, A. C. Strikwerda, D. Pilon, **D. Shrekenhamer**, N. I. Landy, K. Fan, X. Zhang, W. J. Padilla, and R. D. Averitt, "Highly-flexible wide angle of incidence terahertz metamaterial absorber," *Phys. Rev. B (Rapid Communications)* **78**, 241103R (2008).
12. H. Tao, C. M. Bingham, D. Pilon, K. Fan, A. C. Strikwerda, **D. Shrekenhamer**, W. J. Padilla, X. Zhang, and R. D. Averitt, "A dual band terahertz metamaterial absorber," *J. Phys. D Appl. Phys.* **43**, 225102 (2010).
13. D. Shakhvorostov, R. A. Nistor, L. Krusin-Elbaum, G. J. Martyna, D. M. News, B. G. Elmegreen, X. Liu, Z. E. Hughes, S. Paul, C. Cabral, S. Raoux, **D. B. Shrekenhamer**, D. N. Basov, Y. Song, and M. H. Muser, "Evidence for electronic gap-driven metal-semiconductor transition in phase-change materials" *Proc. Natl Acad. Sci.* **106**, 10907 (2009).

14. M. M. Qazilbash, K. S. Burch, D. Whisler, **D. Shrekenhamer**, B. G. Chae, H. T. Kim, and D. N. Basov, "Correlated metallic state of vanadium dioxide," *Phys. Rev. B* **74**, 205118 (2006).

Conference Presentations:

1. *Metamaterial-based imaging for potential security applications*, Invited Talk, Photonics West 2013, San Francisco, CA. February 3-7, 2013
2. *Metamaterial inspired microwave focal plane array*, Metamaterials 2011: The First International Congress on Advanced Electromagnetic Materials for Microwaves and Optics, Barcelona, Spain, 9-13 October, 2011.
3. *High speed terahertz modulation from metamaterials with embedded high electron mobility transistors*, Metamaterials 2011: The First International Congress on Advanced Electromagnetic Materials for Microwaves and Optics, Barcelona, Spain, 9-13 October, 2011.
4. *High speed terahertz modulation from metamaterials with embedded high electron mobility transistors*, ICAM: New frontiers in the physics of two dimensional electron systems, Buenos Aires, Argentina, November 23-25, 2011.
5. *High speed terahertz modulation from metamaterials with embedded high electron mobility transistors*, LEES 2012: Low Energy Electrodynamics in Solids, Napa, CA, July 22-27, 2012.